SPIN INTERACTIONS IN ORGANIC MOLECULAR ARCHITECTURES

A DOCTORAL THESIS
by
ALESSIO VEGLIANTE

Supervised by
José Ignacio Pascual Chico

December 2024

This thesis was carried out at CIC nanoGUNE BRTA

Abstract

The study of magnetism in carbon-based nanostructures is a rapidly advancing field, driven by both fundamental scientific interest and the potential for applications in emerging technologies like molecular spintronics and quantum information.

Although magnetism is commonly associated with transition metals possessing unpaired d- or f-shell electrons, it can also emerge in light elements like carbon. The so-called π magnetism, which arises from unpaired p-shell electrons, is associated to several unique properties, such as enhanced spin delocalization and longer coherence times, which make magnetic carbon-based systems highly attractive for a variety of technological applications. The investigation of intrinsic magnetic states in purely organic nanostructures, long confined to theoretical speculation, is now experimentally accessible thanks to the advancements in on-surface synthesis techniques. These methods enable the fabrication of nanostructures that are difficult to achieve using conventional solution-based chemistry, including highly reactive carbon-based magnetic systems.

In this thesis, we investigate spin interactions in atomically precise organic nanostructures synthesized on metal substrates. Using scanning probe microscopy techniques-primarily scanning tunneling microscopy (STM) and spectroscopy (STS)-combined with theoretical simulations, we characterize the spin states of these systems and explore how they are affected by variations in the structural conformation or local chemical modifications.

We study several organic systems featuring a varying number of unpaired π electrons. First, we investigate the magnetic state exhibited by a non-planar organic diradical (2-OS) on a gold substrate. We demonstrate that the exchange interaction between its two radical units is highly dependent on the precise molecular conformation. Thus, we show that the intramolecular spin coupling can be modified by inducing controlled structural changes with the STM tip, either by applying local attractive forces or by directly contacting the molecule and lifting it from the substrate. Additionally, we study how the

spin state of the diradical can be altered by modifying its chemical structure, specifically by reducing the distance between the radical units, which results in a transition to a closed-shell state.

Next, we investigate more complex nanoarchitectures formed by coupling triangulene building blocks via a combination of in-solution and on-surface reactions. First, we characterize a polyradical nanographene (TTAT), generated by joining three pristine [3]triangulenes through a nitrogen-doped triangulene core. The observation of typical magnetic fingerprints in STS, such as Kondo resonances and inelastic spin excitations, demonstrates the open-shell character of the final structure. With the support of advanced multiconfigurational calculations, we show that this system accommodates three unpaired π electrons which couple ferromagnetically, resulting in a high-spin ground state. Similarly, we synthesize and characterize a [3]triangulene-based macrocycle (TNS), which accumulates twelve unpaired π electrons. We reveal that this nanostructure exhibits a many-body singlet ground state, with collective spin excitations accessible via inelastic electron tunneling spectroscopy. Furthermore, we demonstrate that the magnetic behaviour of this system is consistent with the predictions of the Heisenberg model for an antiferromagnetic $S = 1$ spin ring.

Finally, we explore strategies for fabricating two-dimensional covalent networks based on open-shell triangulene units, with the aim of investigating collective spin states in extended organic architectures. While significant challenges remain in achieving fully ordered two-dimensional structures incorporating π-radical units, we identify here some promising approaches to overcome these obstacles in future research.

Contents

Introduction

Magnetic materials play an essential role in modern science and technology. The investigation of magnetism, from bulk materials down to low-dimensional systems and single molecules, has led to tremendous progress in our understanding of matter and has given rise to crucial technological advancements.

In the last decades, several scientific breakthroughs, starting with the discovery of giant magnetoresistance[1,2], have resulted in the emergence of spintronics, a new research field that aims at using the spin of the electron for storing, processing and transmitting information[3–5]. Compared to conventional electronics, based on the electron charge, this new technology holds promise for devices with higher efficiency, increased processing speed and lower power consumption. Furthermore, electron spins have been proposed as elementary bits for quantum information technology, thus stimulating the fabrication and investigation of nanomaterials and molecules with robust and addressable spin states[6].

Research on magnetism, including studies on single-molecule magnets, has been mostly restricted to the elements belonging to the *d*- and *f*-block of the periodic table[7]. More recently, however, carbon-based nanomaterials have emerged as a new platform for the exploration of quantum magnetism and as potential building blocks for spintronic devices[8].

A fundamental incentive to the investigation of carbon-based nanostructures has surely come from the the widespread interest generated by graphene, a truly two-dimensional all-carbon material, first isolated and characterized in 2004[9,10]. Although graphene itself does not exhibit intrinsic magnetism, some graphene nanostructures with well-defined geometries (also called *nanographenes*) can show spin polarization due to the presence of unpaired π electrons[11,12].

The magnetism arising from *p*-shell electrons presents several features that make it particularly appealing for fundamental studies and potentially advantageous for technological applications. In contrast to transition metals, light elements like carbon exhibit weak spin-orbit and hyperfine coupling, which

result in longer spin coherence times, more delocalized magnetic moments and long-range spin interactions[13,14]. Thanks to these properties, magnetic carbon nanostructures are considered excellent candidates for the realization of stable bits for quantum computing[15], and have been proposed as elementary components for different spintronic devices, such as spin filters, molecular switches and spin valves[11,16–18]. Furthermore, the chemical versatility of carbon, its ability to form a wide variety of compounds, makes these systems highly tunable, and therefore an ideal platform for the fabrication of molecular architectures with tailored magnetic properties.

The presence of unpaired π electrons, however, is associated with high chemical reactivity, which strongly hinders the synthesis and characterization of carbon-based nanomaterials by means of conventional in-solution techniques. Furthermore, their magnetic properties heavily depend on their atomic-scale structure and can be significantly altered by local defects, heteroatoms or changes in the bonding configuration. Thus, atomic precision is an essential requirement for fabricating nanographenes with well-defined and reproducible spin states.

In this respect, a decisive impulse to the experimental exploration of π-magnetism has come from the recent development of *on-surface synthesis* under ultra-high vacuum conditions. By activating controlled reactions of specific precursors on suitable metal surfaces, it is now possible to fabricate carbon nanoarchitectures with full control over their atomic structure and geometry[19,20]. Additionally, an important advantage offered by on-surface synthesis is that the reaction products can be characterized by means of spatially resolved surface-sensitive techniques, such as scanning tunneling microscopy (STM) and spectroscopy (STS). These methods allow direct visualization of the chemical structure of the synthesized molecules, as well as detection of their electronic and magnetic properties with atomic resolution[21].

Thanks to these tools, several magnetic organic systems, that remained elusive to traditional solution chemistry, have been recently generated and characterized on metal substrates, including long sought-after molecules, like the triangulene and the Clar's goblet[22,23].

In addition, by exploiting the manipulation capabilities of the scanning tunneling microscope at low temperature, it is possible to induce chemical reactions in specific molecular sites, to selectively quench or activate radical units, and even to modify the structural conformation of individual molecules or to decouple them from their metal supports. This offers unprecedented control over the magnetic properties of matter at the single-molecule level, which is highly appealing for applications in molecular spintronics. From a

more fundamental point of view, these tools allow to explore and manipulate magnetism at the atomic scale and thus to directly test theoretical spin models.

In this thesis we investigate spin interactions in carbon-based nanostructures fabricated on metal substrates through chemical reactions of specific molecular precursors. We study different all-organic systems featuring an increasing number of unpaired π electrons. Using scanning probe techniques, we unravel the magnetic states that emerge from the interactions among these spin units and rationalize them with the support of theoretical calculations, within the framework of the main models currently used to describe quantum magnetism. The main objectives of this work are: i) to design and synthesize carbon-based nanoarchitectures with well-defined atomic structures and reproducible magnetic states; ii) to detect and characterize the spin interactions emerging in these nanostructures using STM and STS and examine their dependence on the molecular conformation and atomic-scale chemical structure; and iii) to explore methods for manipulating the spin states of these systems, by taking advantage of their chemical or mechanical tunability, to achieve controlled changes in their magnetic properties.

The thesis is organized as follows:

Chapter 1 introduces the main theoretical concepts and the experimental techniques used in the thesis. It starts with a general overview of the topic of π-magnetism in carbon-based nanostructures, with a special focus on the electronic and spin properties of the [3]triangulene, a paradigmatic example of nanographene, which represents the basic building block of some of the structures investigated in the thesis. Additionally, the impact of heteroatom substitution on the spin state of graphene flakes are briefly discussed.

Then we present the principles of scanning tunneling microscopy and spectroscopy, with a focus on bond-resolved imaging and on the detection of magnetism in single molecules through its characteristic fingerprints in STS (Kondo resonances and inelastic spin excitation features). This is followed by a description of the on-surface synthesis strategies commonly used to fabricate graphene nanostructures. The chapter is completed with a brief description of the experimental setup.

Chapter 2 reports the on-surface generation and investigation of the non-planar organic diradical **2-OS**, a derivative of the Chichibabin's hydrocarbon, with a focus on the dependence of the intra-molecular spin coupling on the structural conformation of the molecule. We show that the exchange interaction between its two spin units can be tuned by means of mechanical manipulation using the STM tip. Furthermore, we explore the possibility of modifying the molecule's spin state through changes in its chemical structure.

Chapter 3 focuses on an open-shell nanographene obtained through a strategic coupling of three [3]triangulenes to the edges of a nitrogen-substituted [3]triangulene core. We show that such combination of triangulene building blocks results in a structure with three unpaired π electrons. We thus reveal the interaction among these three spins, and demonstrate that the system behaves as a ferromagnetic spin trimer.

Chapter 4 reports the on-surface synthesis and characterization of a molecular macrocycle obtained by coupling six [3]triangulenes through their vertices. The resulting nanostructure accumulates a large number of unpaired π electrons (twelve) which give rise to a many-body singlet ground state. We probe the spin states of this triangulene-based ring through the fingerprints of the collective spin excitations revealed by inelastic electron tunneling spectroscopy. Also, we investigate how the passivation of a radical unit or the opening of the cyclic structure modify the spin properties of the system.

Chapter 5 focuses on our on-going exploration of on-surface synthesis strategies for building extended two dimensional structures based on open-shell triangulene units. We report a few attempts using distinct molecular precursors, highlighting the challenges associated with the generation of covalent triangulene networks, and outline the most promising directions for future experiments.

Chapter 6 summarizes the main conclusions of the thesis.

Contributions from collaborating groups

The work presented in this thesis is the result of a collaboration between several research groups. The experimental work involving on-surface synthesis and characterization through scanning probe microscopy was carried out by me, with contributions from other members of my group (Scanning Probe Microscopy at NanoGUNE). The synthesis of all the molecular precursors was performed by the group of Diego Peña (CiQUS and Universidade de Santiago de Compostela, Santiago de Compostela, Spain), while the theoretical calculations were carried out by the groups of Thomas Frederiksen (Donostia International Physics Center, San Sebastián, Spain), Emilio Artacho (CIC NanoGUNE, San Sebastián, Spain), and Pavel Jelínek (Institute of Physics, Czech Academy of Sciences, Prague, Czech Republic), with specific contributions as indicated in the different chapters. Additionally, in Section 2.5, I also report complementary data from MCBJ experiments conducted by the group of Herre van der Zant (Delft University of Technology, Delft, The Netherlands), as part of our collaboration. The specific contributions from the members of these groups are indicated in the footnotes of the corresponding chapters.

1 Theory and experimental methods

1.1 Electronic structure of sp^2 carbon systems

Carbon is one of the most versatile chemical elements, as reflected in the great variety of existing carbon-based compounds, both organic and inorganic. Carbon atoms can bond together in different ways, giving rise to several allotropes with very diverse properties, from diamond, an insulator, to graphite, which is instead a good electrical conductor. This variety stems from different bonding geometries, which depend on the hybridized orbitals involved in the carbon-carbon covalent bonds.

The carbon atom exhibits four valence electrons, and is therefore able to form up to four covalent bonds, as a result of its ground state electronic configuration $1s^2 2s^2 2p^2$. In a covalent structure, a carbon atom is bonded to neighbouring atoms (carbon or different ones) through $n+1$ hybrid orbitals, indicated as sp^n orbitals, which arise from the combination of the $2s$ orbital with n $2p$ orbitals, as illustrated in Figure 1.1a.

In this thesis we study magnetism in polycyclic aromatic hydrocarbons (PAHs) composed of sp^2-hybridized carbon atoms. In such structures, each carbon atom forms three sp^2 orbitals, resulting from the hybridization of the $2s$ orbital with two of the $2p$ orbitals. This leads to the formation of three σ bonds with the neighbouring atoms in a planar trigonal geometry. The remaining p_z orbitals, which lie perpendicular to the plane of the molecule and are not affected by the hybridization, overlap laterally forming the conjugated π-electron system (Figure 1.1b).

Most of these molecules can be described as finite fragments of graphene, a single layer of sp^2-hybridized carbon atoms arranged in a honeycomb lattice. As shown in Figure 1.1c, graphene is a *bipartite* system, made up of two interconnected hexagonal sublattices. Each carbon atom shares three valence

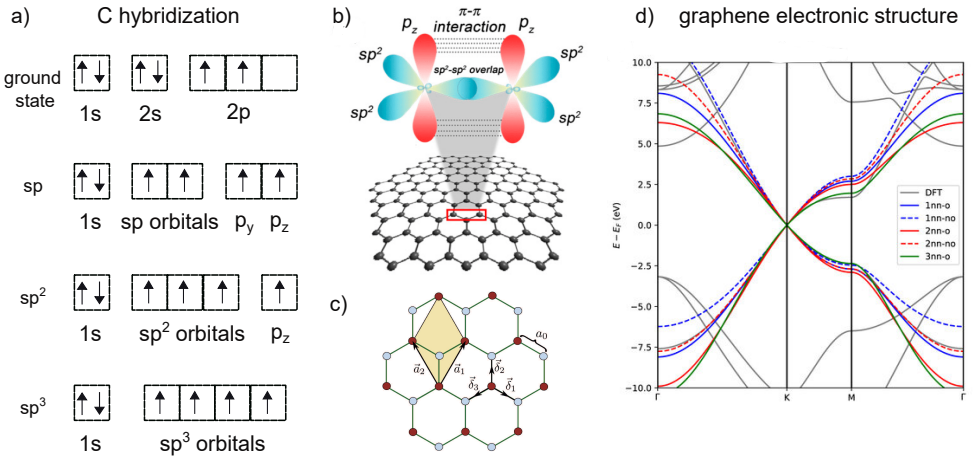

Figure 1.1: (a) Schematic depicting orbital hybridization in carbon. (b) Representation of carbon orbitals and their bonds in sp^2-hybridized carbon systems. Adapted from [24]. (c) Honeycomb lattice of graphene composed of two interpenetrating sublattices (red and blue atoms). Adapted from [25]. (d) Band structure of graphene calculated with DFT (in grey) and different tight-binding models. The graph includes the nearest-neighbour model (blue), next-nearest neighbour model (red) and third-nearest neighbour model (green), with both orthogonal (-o) and non-orthogonal (-no) basis variants. Adapted from [12].

electrons with three atoms belonging to the opposite sublattice through the in-plane sp^2 hybrid orbitals. The bonds formed between the p_z atomic orbitals give rise to the π band, exhibiting a characteristic linear dispersion at the Fermi level, which is responsible for the peculiar electronic properties of the system[26]. Each carbon atom contributes with a single electron to the π band, which is therefore called *half-filled*.

Taking advantage of the orthogonality between the σ- and the π-symmetry electronic states, the properties of graphene and, more broadly, of planar sp^2 carbon structures can be understood by considering only the p_z electrons forming the π-conjugated system, which play the dominant role in their low-energy electronic features.

The usual starting point for describing the electronic properties of graphene-like structures is the *tight-binding* (TB) model, which, although relatively simple, already captures the most relevant features of many of such systems. In this model, the electronic structure of a solid is determined considering atomic orbitals localized at the lattice sites and the possibility of electron *hopping* between neighbouring sites. Importantly, this approximation ignores electron-electron interactions.

The nearest-neighbour TB Hamiltonian can be written as

$$\hat{H}_0 = -t \sum_{\langle i,j \rangle, \sigma} [c^{\dagger}_{i\sigma} c_{j\sigma} + h.c.], \tag{1.1}$$

where $c^{\dagger}_{i\sigma}$ and $c_{i\sigma}$ are the creation and annihilation operators of an electron with spin σ at site i, respectively, and t is the hopping integral between nearest-neighbour orbital sites. The notation $\langle i, j \rangle$ indicates the pairs of nearest-neighbour atoms, while *h.c.* stands for the Hermitian conjugate terms. In the case of neutral graphene systems, we consider one $2p_z$ orbital for each sp^2 carbon atom.

It is found that this simple approach reproduces well the electronic properties of graphene. In fact, considering a nearest-neighbour hopping integral $t \approx 2.7$ eV, the TB model correctly yields the linear dispersion of the π-symmetry conduction and valence bands, as shown in Figure 1.1d. These bands touch at the Fermi level, making graphene a zero-gap semiconductor, or *semimetal*. It is important to point out that the absence of a band gap in pristine graphene is a consequence of the equivalence of its two sublattices.

The TB model can also be used to get a first insight into the electronic properties of finite graphene flakes. An example is reported in Figure 1.2c, which illustrates the solution of the Hamiltonian 1.1 for the [3]triangulene, a paradigmatic example of nanographene. This molecule is a planar benzenoid PAH exhibiting a characteristic triangular shape with three carbon hexagons along each side (Figure 1.2a). All the carbon atoms constituting the system are sp^2-hybridized, including those at the edges, which are passivated by hydrogen atoms.

The low-energy spectrum calculated with the TB model reveals an occupied and an unoccupied molecular orbital at symmetric energies with respect to zero and, interestingly, two electronic states exactly at zero energy[27]. Zero-energy states are relevant in the context of magnetism since, in presence of repulsive electron-electron interactions, they tend to undergo spin polarization, in agreement with the Stoner criterion[11]. This mechanism essentially represents a possible way to overcome the instability induced by the presence of low-energy electrons. However, the TB model fails to capture this effect, and therefore the onset of magnetism, since it treats the electrons as non-interacting particles.

The Hamiltonian 1.1 can be complemented with a term accounting for short-range electrostatic Coulomb interactions. This leads to the *Hubbard* model, which is described by the Hamiltonian

$$\hat{H} = \hat{H}_0 + U \sum_i n_{i\uparrow} n_{i\downarrow}, \tag{1.2}$$

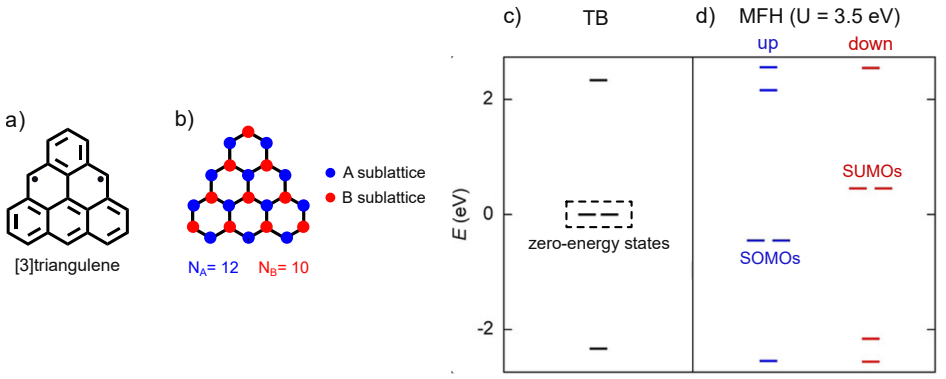

Figure 1.2: (a) Chemical structure of the [3]triangulene. (b) Representation of the molecule highlighting the atoms belonging to the two sublattices, A (blue) and B (red). (c) Nearest-neighbour tight-binding energy spectrum, obtained using $t = 2.7$ eV. The two states appearing at zero energy are highlighted in the dashed box. (d) Mean-field Hubbard energy spectrum, obtained for $U = 3.5$ eV. The introduction of electron-electron interaction results in a spin polarization. Figures (c) and (d) adapted from [27].

where $n_{i\sigma} = c^{\dagger}_{i\sigma} c_{i\sigma}$ is the number operator at the site i, and $U > 0$ represents the repulsive on-site Coulomb interaction energy. It is noteworthy that this Hamiltonian does not include long-range interactions; rather, it considers a repulsive interaction between two electrons only when they occupy the same orbital.

Due to the difficulty of obtaining an exact numerical solution even for small systems, this additional term is usually treated introducing a mean-field approximation, which leads to the Hamiltonian

$$\hat{H}_{\mathrm{MFH}} = \hat{H}_0 + U \sum_i \left(n_{i\uparrow} \langle n_{i\downarrow} \rangle + \langle n_{i\uparrow} \rangle n_{i\downarrow} - \langle n_{i\uparrow} \rangle \langle n_{i\downarrow} \rangle \right), \tag{1.3}$$

where $\langle n_{i\sigma} \rangle$ indicates the average population of spin σ electrons at site i.

As shown in Figure 1.2d, application of this model to the [3]triangulene leads to the emergence of a spin polarization and consequently to the opening of an energy gap (Coulomb gap). This results in the appearance of two singly occupied molecular orbitals (SOMOs) with the same spin polarization[27]. According to this picture, the [3]triangulene can be described as an open-shell molecule hosting two unpaired π electrons (also referred to as *diradical* molecule). Additionally, following Hund's rule, the spins of the two electrons occupying the SOMOs are aligned parallel to each other, therefore we can expect a ground state with total spin $S = 1$ (triplet state).

A closer look at the structure of the [3]triangulene (Figure 1.2b) reveals a difference in the number of atoms belonging to each of the two sublattices.

This asymmetry lies at the origin of its magnetic state, as we will discuss in the next section.

1.2 Emergence of magnetism in graphene nanostructures

1.2.1 Lieb's theorem

The equivalence between the two sublattices is responsible for the lack of intrinsic magnetism in pristine graphene. Therefore an immediate way to induce a net spin state in graphene (or in a graphene-based nanostructure) is by creating a sublattice imbalance. This can be intuitively understood considering that, since each carbon can form π bonds only with atoms of the opposite sublattice, a difference in the number of sites in the sublattices results in one or more π electrons that cannot be paired.

A more rigorous explanation is based on Lieb's theorem, which allows determining the total spin of bipartite systems described by the Hubbard model in case of repulsive electron interactions ($U > 0$)[28]. According to this theorem, which represents a generalization of the Ovchinnikov's rule[29], the ground state of such systems exhibits a total spin

$$S = \frac{1}{2}|N_A - N_B|, \tag{1.4}$$

where N_A and N_B indicate the number of atoms belonging to sublattices A and B, respectively. It immediately follows that in a graphene system a sublattice imbalance leads to a net spin polarization.

One way to induce an asymmetry between the graphene sublattices is by removal of a p_z electron from the π-conjugation network. This was achieved experimentally by creating atomic vacancies in a graphene layer through ion bombardment, which indeed resulted in a local spin polarization, as revealed by scanning tunneling spectroscopy[30]. In another experiment, the same effect was obtained through passivation with atomic hydrogen, which locally changed the carbon hybridization from a sp^2 to a sp^3 configuration[31].

Although these works demonstrated for the first time the possibility of inducing magnetism in graphene, they were based on the generation of defects or on the addition of heteroatoms. However, an *intrinsic* magnetism can develop in pristine graphene nanostructures when they are shaped in such a way as to create a sublattice imbalance.

An example is the [3]triangulene, introduced in the previous section. This molecule, in fact, exhibits a different number of atoms in the two A and B

sublattices ($N_A = 12$ and $N_B = 10$), from which Lieb's theorem predicts a $S = 1$ ground state, in agreement with the electronic occupation of the energy states obtained by solving the mean-field Hubbard Hamiltonian (Figure 1.2d). This theorem therefore provides a powerful counting rule, which can be easily applied to graphene nanostructures with well-defined geometries to predict their spin state.

1.2.2 Unpaired π electrons and Clar sextets

In many cases, the emergence of magnetism can be directly inferred from the Lewis structure of the nanographene. Considering again the [3]triangulene as an example (Figura 1.2a), one can see that it is not possible to draw any resonance structure without leaving unpaired π electrons, specifically two electrons in the majority sublattice.

A conjugated hydrocarbon like the [3]triangulene, which cannot be associated with a classical Kekulé structure, in which all the carbon atoms are π-bonded, is known as a non-Kekulé molecule. It is important to note, however, that the presence of unpaired electrons is not necessarily the result of a sublattice imbalance, as we will discuss in the next section.

Drawing chemical structures, therefore, provides a first insight into the potential emergence of spin states in a graphene nanostructure. However, a PAH typically exhibits more than one possible resonance structure, and in some cases a molecule can be represented by both open-shell and closed-shell resonance structures[12].

A useful tool for determining the most likely resonance structure of a nanographene is the Clar's rule, which relates the chemical stability of a molecule with the number of *Clar sextets*, i.e., six-membered carbon rings featuring three conjugated π bonds[32,33]. According to this empirical rule, for a benzenoid PAH the most important resonance structure is the one displaying the highest number of non-adjacent Clar sextets. This follows from the observation that a larger number of Clar sextets is associated to a higher aromaticity, which results in an increase of the chemical stability of the molecule.

1.2.3 Nullity

Another important counting rule that is usually used in the determination of the magnetic properties of sp^2-hybridized carbon systems is derived from benzenoid graph theory and is based on the concept of *nullity*[34]. This quantity refers to the number of zero-energy states of a molecule as obtained by solving

the nearest-neighbour tight-binding Hamiltonian 1.1. According to this rule, the nullity η of a honeycomb system is given by

$$\eta = 2\alpha - N, \tag{1.5}$$

where N is the total number of sites and α is the maximum possible number of sites that are not nearest neighbours to each other.

Determining the nullity of a certain nanostructure allows us to get a first insight into its magnetism, since zero-energy states are expected to undergo spin polarization for $U > 0$, as we saw before. Therefore the nullity of a graphene fragment can be directly linked to the number of π radical units, i.e., of unpaired π electrons.

Application of this rule to the [3]triangulene correctly yields $\eta = 2$. In fact, as it is common in bipartite structures, the maximum number of non-adjacent sites is equal to the number of atoms of its majority sublattice $N_A = 12$, hence $\eta = 24 - 22$.

Further examples are shown in Figure 1.3, where we report the structures of other graphene fragments, along with the intrinsic spin state predicted by Lieb's theorem and their nullity. Importantly, such nanographenes have been actually synthesized and characterized on metal surfaces, confirming their open-shell character and the spin states determined with these simple counting rules[23,35,36].

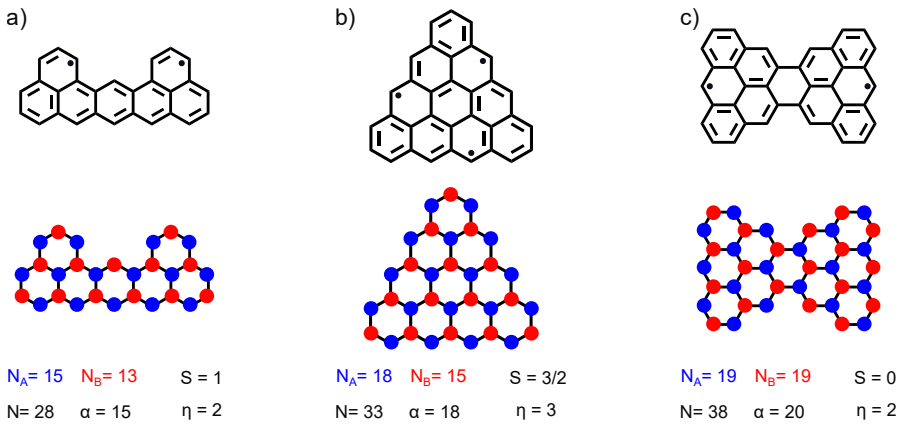

Figure 1.3: Application of the counting rules (Lieb's theorem and nullity) for the prediction of the magnetic properties of graphene nanostructures. (a) and (b) are examples of structures with sublattice imbalance (heptauthrene and [4]triangulene, respectively[27,37]). The nanostructure represented in (c), called Clar's goblet, is an example of a non-Kekulé molecule without sublattice imbalance[23].

A significant case is represented by the bowtie-shaped molecule in Figure 1.3c, the so-called Clar's goblet. Differently from the other systems reported in Figure 1.3, this nanographene does not exhibit a sublattice imbalance. It follows that Lieb's theorem predicts a total spin $S = 0$ for its ground state, which apparently suggests a closed-shell structure. However, by applying equation 1.5, it is found that the system's nullity is $\eta = 2$. This is in agreement with the TB calculations, revealing two zero-energy states, which are expected to undergo spin polarization when including the Hubbard interaction term[11,23]. Indeed, it can be verified that, despite the absence of sublattice imbalance, no Kekulé structure can be drawn for this molecule.

To account for the $S = 0$ (singlet) ground state predicted by Lieb's theorem the electrons occupying the two SOMOs need to be antiferromagnetically coupled, which is in apparent contrast with Hund's rule. However, as seen in the resonance structure in Figure 1.3c, here the two unpaired π electrons belong to opposite sublattices, unlike the case of the [3]triangulene. The two sublattices can be considered as two independent systems, to which Hund's rule applies separately[23].

These observations, based on the counting rules, allow us to get a first insight into the mechanisms of spin coupling in graphene magnetic nanostructures. In particular, they indicate that radical states belonging to opposite sublattices tend to couple antiferromagnetically, while for unpaired electrons located on the same sublattice the ferromagnetic alignment is favoured. However, it is important to consider that these simple conclusions can be applied only to bipartite structures, as they are derived from Lieb's theorem, and therefore are not valid for doped systems or in the presence of non-benzenoid rings.

1.2.4 Effects of nitrogen substitution

Incorporating a foreign atom into the lattice of a nanographene can drastically alter its electronic and magnetic properties. We focus here on the effects of nitrogen substitution in triangulenes, which will be employed in some of the nanostructures investigated in this thesis (Chapters 3 and 5).

The electronic configuration of nitrogen in its ground state is $1s^2 2s^2 2p^3$, which includes an additional valence electron with respect to carbon. Therefore, incorporating a substitutional nitrogen atom in the graphene honeycomb can be can be viewed as introducing an additional electron into the p_z orbital of the corresponding lattice site.

As an example, we consider here the case of the N-doped [3]triangulene, also referred to as aza[3]triangulene, which was recently synthesized and char-

acterized on metal surfaces[38]. As shown in Figure 1.4a, the central atom of the triangulene belongs to the minority sublattice. A first way to understand the effect of substituting C with N in this site is to interpret the addition of the extra p_z electron as the removal of the corresponding atom from the π-conjugation network. Applying Lieb's theorem to the [3]triangulene, but taking now into account one atom less in the minority sublattice, results in a $S = 3/2$ ground state. This would correspond to the chemical structure represented in Figure 1.4b, exhibiting three unpaired electrons in the same sublattice.

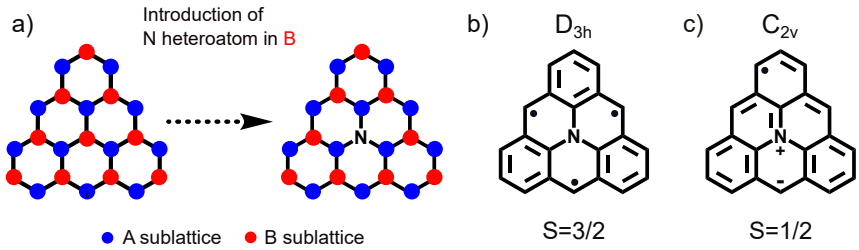

Figure 1.4: (a) Substitution of the central C atom with a N atom in the [3]triangulene, leading to the aza[3]triangulene. The atoms belonging to the majority and minority sublattices are marked in blue and red, respectively. (b) Chemical structure of the possible $S = 1/2$ ground state configuration, exhibiting a D_{3h} symmetry. (c) Molecular structure with C_{2v} symmetry and spin $S = 1/2$: this structure, driven by Jahn-Teller distortion, represents the most energetically favourable configuration according to theoretical calculations[38].

It is important to consider, however, that using Lieb's theorem in this context is not strictly correct since it should be applied only to bipartite systems. Indeed, density functional theory (DFT) calculations show that the ground state of the aza[3]triangulene is a doublet ($S = 1/2$)[38]. As illustrated in Figure 4c, the structure with a single radical unit exhibits a lower molecular symmetry (C_{2v}) with respect to the triradical one (which has a D_{3h} structure). The $S = 1/2$ ground state is, in fact, a more energetically stable configuration driven by a Jahn-Teller distortion. It is characterized by an internal charge redistribution, resulting in a zwitterionic structure, and the formation of a C-N π bond, which reduces the number of radical units from three to one.

It was shown that this is actually a common mechanism in N-doped triangulenes hosting the N atom in the minority sublattice. On the other hand, application of Lieb's theorem yields a correct prediction of the spin state of aza-triangulenes when N occupies a site of the majority sublattice, since in this case the Jahn-Teller distortion and consequent charge redistribution would not lead to a reduction in the number of unpaired electrons[39].

As an alternative to using Lieb's theorem to predict the spin state of an aza-triangulene, a more rigorous approach is to first determine the zero-energy states of the correspondent pristine molecule (e.g., by calculating its nullity) and afterwards consider the effect of adding an extra electron, coming from the N atom. We will present an example of application of this approach in the prediction of the spin state of the N-doped nanostructure investigated in Chapter 3.

1.3 Magnetic interactions in carbon-based nanostructures

As previously noted, the presence of more than one radical unit in a graphene nanostructure can lead to the development of different intra-molecular magnetic interactions. In the case of diradical nanographenes, for example, both ferromagnetic couplings, as in the [3]triangulene[22,40], or antiferromagnetic interactions, as in the Clar's goblet[23], have been reported.

Considering a system with two radical units, the magnetic interaction can be described in terms of an effective spin model:

$$H = J\vec{S}_1 \cdot \vec{S}_2, \tag{1.6}$$

where J is the exchange coupling, and $\vec{S}_i$ (i =1,2) is the spin operator of the electron at site i.

There are essentially three exchange mechanisms which determine the strength and sign of J in carbon-based nanostructures[41]: i) Hund exchange, ii) kinetic superexchange and iii) Coulomb-driven superexchange.

The *Hund exchange* is observed in the case of spatial overlap of the electronic wavefunctions. It is always ferromagnetic, since it stems from the reduction of the Coulomb repulsion between the electrons, and scales linearly with the Coulomb interaction. This mechanism is responsible for the triplet ground state of the [3]triangulene: in this molecule the large spatial overlap between the two zero-energy states results in a strong ferromagnetic coupling, with an exchange J in the order of hundreds of meV ($J \approx 500$ meV).

The second mechanism, the *kinetic superexchange*, is always antiferromagnetic, and stems from the hybridization between the zero-energy states of the nanographene. It can be directly related to the hopping mechanism between different lattice sites, included in the tight-binding Hubbard Hamiltonian 1.2, and therefore accounts for the antiparallel alignment of the spins of unpaired electrons belonging to opposite sublattices (as in the case of the Clar's goblet).

The strength of the coupling depends on the interplay between the hybridization t and the Coulomb interaction U. In particular, in the limit $t \gg U$, the exchange coupling is given by

$$J = \frac{4t^2}{U} \tag{1.7}$$

which corresponds to the expression of the Heisenberg model for antiferromagnetic interactions.

The third mechanism, the *Coulomb-driven superxchange*, can lead to both ferromagnetic and antiferromagnetic coupling. It is a more complex mechanism, involving also orbitals different from the zero-energy states, as recently described in [41]. The name stems from the fact that in this case the coupling scales quadratically with the Coulomb interaction.

As we will discuss in the next section, scanning tunneling spectroscopy allows us to reveal spin interactions in individual molecules, to map their spatial distribution and to directly quantify the exchange couplings. Indeed, robust magnetic interactions, with values of the exchange coupling ranging from a few meV up to $J \approx 200$ meV, have been measured on nanographenes synthesized on metal substrates[12,42,43]. Certainly, the study of magnetic interactions in carbon nanostructures is not limited to diradicals. Scanning tunneling spectroscopy is also a powerful tool to investigate the more complex spin states emerging from the interactions of multi-radical units, as we will show in Chapters 3 and 4.

1.4 Scanning tunneling microscopy

Scanning tunneling microscopy (STM) and spectroscopy (STS) represent the main experimental techniques used for investigating the structural, electronic and magnetic properties of carbon-based nanostructures. Since its development in 1981[44,45], the scanning tunneling microscope has emerged as one the most powerful tools in surface science, enabling the study and manipulation of matter down to the single-molecule and single-atom level.

The working principle of STM is based on the quantum tunneling effect. As shown in the scheme in Figure 1.5a, an atomically sharp metallic tip, moved by a piezoelectric actuator, is brought very close to a conducting sample's surface, at a distance on the order of a few Å. The application of a voltage bias between the tip and sample results in a current of electrons (generally in the sub-nanoampere range) tunneling through the vacuum which separates the two electrodes[46]. This potential barrier, in fact, can be overcome by

the electrons with a finite probability, that depends exponentially on the tip-sample distance.

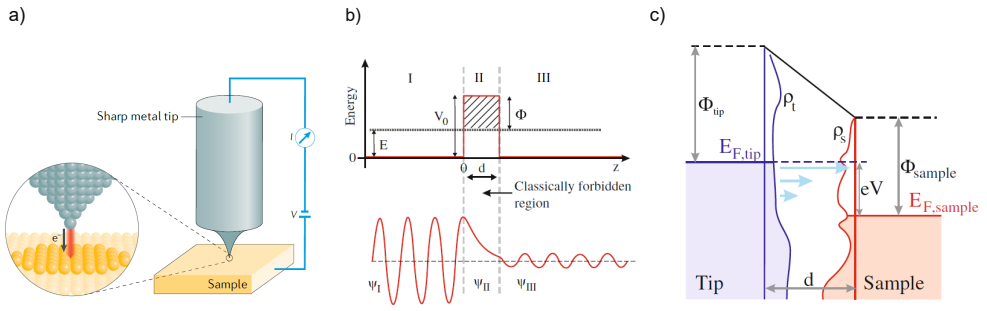

Figure 1.5: (a) Simplified representation of the set up for scanning tunneling microscopy (STM) and spectroscopy (STS). Adapted from [47]. (b) Quantum tunneling in the approximation of a one-dimensional square potential barrier. (c) Energy level diagram of the vacuum junction with an applied bias voltage V between tip and sample. The horizontal arrows with different lengths indicate the exponential decrease of the transmission factor for lower electron energies. Adapted from [46].

A first approximation to describe the quantum tunneling effect is to consider a plane wave $\psi(z)$ of energy E travelling through a one-dimensional square potential barrier (with height $V_0 > E$), as represented in Figure 1.5b. For this system the solution of the time-independent Schrödinger equation is given by

$$\psi(z) = \psi(0)e^{-kz}, \qquad k = \sqrt{\frac{2m}{\hbar^2}(V_0 - E)}, \tag{1.8}$$

where $\psi(0)$ represents the electron wavefunction at the tip position (z=0), m is the mass of the electron and $\hbar$ is the reduced Planck constant.

This exponential dependence forms the basis for the high spatial sensitivity of STM. A change of 1 Å in the tip-sample distance, for example, typically results in one order of magnitude change in the tunneling current: this allows us to detect variations on the metal surface at the atomic scale.

However, the information provided by the tunneling current is not only related to the "topography" of the surface but also to its local electronic density of states. This can be rationalized considering the model developed by Bardeen for describing tunneling in metal-insulator-metal junctions[48].

In this approach, the tip-barrier and the sample-barrier are treated as two separate systems. Their electronic states, ψ_{tip} and ψ_{sample}, are obtained by solving the time-independent Schrödinger equation for the two subsystems. Then, using time-dependent perturbation theory for weak coupling between

the electrodes, the transition rates between the initial i and the final f state of the tunneling process are computed, resulting in the matrix elements

$$M_{fi} = \frac{\hbar^2}{2m} \int_{\mathrm{S}} \left[\psi_{\mathrm{tip},i}(\mathbf{r}) \nabla \psi^*_{\mathrm{sample},f}(\mathbf{r}) - \psi^*_{\mathrm{sample},f}(\mathbf{r}) \nabla \psi_{\mathrm{tip},i}(\mathbf{r}) \right] \cdot d\mathbf{S}, \tag{1.9}$$

where $\mathbf{S}$ indicates an arbitrary surface separating tip and sample.

The tunneling current can be expressed in terms of these transition matrix elements, as follows:

$$I = \frac{2e}{\hbar} \sum_{i,f} |M_{fi}|^2 \delta(E_f - E_i), \tag{1.10}$$

where e is the electron charge, and E_i and E_f represent the energies of the initial and final state, respectively. Importantly, the delta function appearing in the expression guarantees that the tunneling process is elastic, i.e., that no energy is lost during the process.

It is then possible to express the tunneling current in terms of the electronic density of states of tip and sample. In the limit of $T = 0$, the resulting expression is

$$I = \frac{4\pi e}{\hbar} \int_0^{eV} \rho_{\mathrm{tip}}(\epsilon - eV) \rho_{\mathrm{sample}}(\epsilon) |M(\epsilon)|^2 \, d\epsilon, \tag{1.11}$$

where $\rho(\epsilon)$ is the energy-dependent density of states of tip/sample, V is the applied bias voltage and $M(\epsilon)$ represents the transition matrix element as a function of the energy. In the case of a one-dimensional rectangular energy barrier, $M(\epsilon)$ is commonly approximated by the transmission factor

$$T(\epsilon, V, d) \propto \exp\left[-2d \sqrt{\frac{2m}{\hbar^2} \left(\frac{\Phi_{\mathrm{tip}} + \Phi_{\mathrm{sample}}}{2} + \frac{eV}{2} - \epsilon \right)} \right], \tag{1.12}$$

where d is the tip-sample distance and Φ indicates the work function of the tip or the sample.

Consequently, the tunneling current from Equation 1.11 can be expressed as

$$I = \frac{4\pi e}{\hbar} \int_0^{eV} \rho_{\mathrm{tip}}(\epsilon - eV) \rho_{\mathrm{sample}}(\epsilon) T(e, V, d) \, d\epsilon. \tag{1.13}$$

According to this expression, the transmission factor depends on the energy of the tunneling electrons. As shown in the scheme in Figure 1.5c, the effective barrier for an electron with energy ϵ is given by $\bar{\Phi} + \frac{eV}{2} - \epsilon$, where $\bar{\Phi}$ is the average work function between tip and sample. An important consequence

is that the transmission reduces exponentially for electrons with lower energy (as indicated by the arrows in the figure), and therefore the main contribution to the tunneling comes from the electrons located at the Fermi level.

In the case of a small bias ($eV \ll \Phi$), the transmission factor can be considered independent from ϵ and V and only dependent (exponentially) on the tip-sample distance, as discussed before. In this approximation, I is given by

$$I = \frac{4\pi e}{\hbar} T(d) \int_0^{eV} \rho_{\text{tip}}(\epsilon - eV)\rho_{\text{sample}}(\epsilon)\, d\epsilon, \tag{1.14}$$

which clearly accounts for the tunneling current's dependence on the combined density of states of tip and sample in the energy window determined by the applied bias voltage.

In the case of a finite temperature, the Fermi-Dirac distributions $f(\epsilon)$ can be included in 1.13, leading to the expression

$$I = \frac{4\pi e}{\hbar} \int_{-\infty}^{\infty} [f(\epsilon - eV) - f(\epsilon)]\, \rho_{\text{tip}}(\epsilon - eV)\rho_{\text{sample}}(\epsilon) T(\epsilon, V, d)\, d\epsilon. \tag{1.15}$$

The results obtained from this model, however, do not consider realistic wavefunctions for the sample and the tip and therefore do not account for the spatial resolution provided by STM.

The Bardeen model was adapted to the specific tip-sample geometry by Tersoff and Hamann[49]. They calculated the matrix element M in Equation 1.10 considering the tip as a point source at position $\mathbf{r}_t$ described by a spherical s-like orbital. In this configuration, and in the limit of small bias voltage V, the tunneling current can be expressed as

$$I \propto \sum_n |\psi_n(\mathbf{r}_t)|^2 \delta(E_F - E_n) \equiv \rho_{\text{sample}}(E_F, \mathbf{r}_t). \tag{1.16}$$

Within this approximation the current results proportional to the local density of state (LDOS) of the sample evaluated at the Fermi level E_F in the tip position $\mathbf{r}_t$. It follows that an STM measurement enables the probing of the local electronic properties of a surface with atomic resolution.

1.4.1 STM imaging

The exponential dependence of the tunneling current on the tip-sample distance can be directly exploited to gain information on the atomic-scale topography of a metal surface. For this end, the STM tip is scanned across the sample with picometer precision by using piezoelectric crystals.

The most common method of operation is the so-called *constant-current* mode, in which the tunneling current is maintained at a set value (typically

in the order of picoamperes) using a feedback loop mechanism. The corresponding variation in the tip-sample distance can then be processed into a topographic image of the sample surface and its adsorbed molecules. It is important to consider, however, that STM images do not provide the actual atomic height of molecules or other adsorbates. As seen in Equation 1.14, in fact, the tunneling current is actually a result of the convolution between the topography and the electronic density of states.

An alternative method is the *constant-height* mode. In this case, the feedback mechanism is disabled and the tip is scanned over the surface at a fixed height. The consequent variation in the current provides the information about the sample topography. This method is generally used for scanning small and flat areas, typically for probing individual molecules. In particular, it is the preferred mode for performing *bond-resolved* STM (BR-STM) imaging, i.e., to resolve the atomic structure of planar organic molecules.

BR-STM represents one of the most powerful tools to investigate individual molecules on surfaces. It is typically performed using a carbon monoxide (CO)-functionalized tip, i.e., a tip having a single CO molecule attached at its apex, and scanning at small tip-sample separation and at low bias (typically $V \leq 10\,\mathrm{mV}$)[50].

The enhanced contrast obtained when CO is attached to the STM tip can be explained considering the lateral deflection of CO, which occurs due to Pauli repulsion between the CO and the chemical bonds of the surface-adsorbed molecule when scanning at close distances[51]. The lateral relaxation then leads to a variation in the conductance of the junction, which allows for the spatial localization of the individual chemical bonds though the contrast in the tunneling current. An example is reported in Figure 1.6a, which demonstrates the possibility of characterizing the atomic-scale structure of a nanographene using BR-STM. It is noteworthy that, since STM probes a convolution of topography and electronic density of state, a BR-STM image may also reveal low-bias electronic features (like the Kondo resonance, described in the next section), as shown in Figure 1.6b. From one side this effect can hinder a proper visualization of the chemical structure of the molecule; on the other hand, it provides a useful tool to spatially localize such low-energy features (e.g., to identify the presence of radical units).

1.4.2 Complementary bond-resolved imaging with nc-AFM

An alternative technique for the determination of the atomic-scale structure of organic molecules is non-contact atomic force microscopy (nc-AFM), which is also performed using a CO-functionalized tip, as first demonstrated by Gross

et al. in 2009[52]. Differently from STM, which relies on measuring the tunneling current, nc-AFM detects atomic forces by scanning a cantilever close to the surface in non-contact mode[53]. This allows the direct measurement of the topography of the system, providing a true visualization of the molecular structure without interference from the electronic states. As an example, nc-AFM imaging of the [3]triangulene is shown in Figure 1.6c[22]. This technique is particularly useful in systems with low-energy electronic features that can alter the visualization of the submolecular structure in STM[54,55].

Although STM is the primary tool used in this thesis, an example of constant-height bond-resolved nc-AFM imaging will be provided in Chapter 3. In this experiment, we use a q-plus sensor, which allows for simultaneous detection of STM and AFM images[56]. This is illustrated in Figures 3.1f-g, which demonstrate the higher capability of AFM to visualize the precise chemical structure of the molecule, without the distortions caused by electronic contributions in STM imaging.

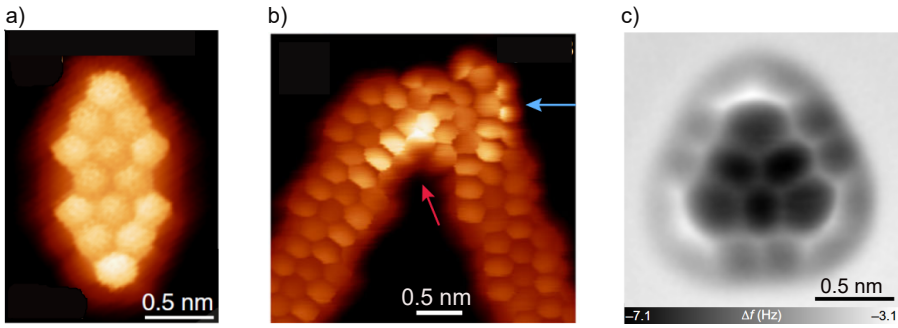

Figure 1.6: (a) Constant-height STM current image of a nanographene recorded with a CO-functionalized tip at $V = 5$ mV. This imaging mode, known as BR-STM, allows direct visualization of the bond-resolved structure of the molecule. Adapted from [57]. (b) Example of a BR-STM image (recorded at $V = 8$ mV) in the presence of low-bias spectral features, which appear as bright regions (indicated by the arrows). Adapted from [58]. (c) Bond-resolved constant-height nc-AFM image of [3]triangulene on a Cu surface. The AFM image was obtained using a q-plus sensor with a CO-functionalized tip, operated in frequency-modulation mode (oscillation amplitude $A = 50$ pm). Adapted from [22].

1.5 Scanning tunneling spectroscopy

As discussed in the previous section, the tunneling current measured in STM depends on the local density of states of tip and sample. This principle is

exploited in scanning tunneling spectroscopy (STS) to probe the electronic properties of a system with atomic resolution.

In STS the tip is kept at a constant height and the tip-sample bias is swept in a certain range, while measuring the differential conductance (dI/dV). This quantity can be directly related to the LDOS of the sample, as seen by differentiating Equation 1.13 with respect to V. Under the approximation of constant ρ_{tip},

$$\frac{dI}{dV}(V)\frac{\hbar}{4\pi e} = e\rho_{\text{tip}}\rho_{\text{sample}}(eV)T(eV,V) + \int_0^{eV} \rho_{\text{tip}}\rho_{\text{sample}}(\epsilon)\frac{\partial T(\epsilon,V)}{\partial V}\,d\epsilon. \tag{1.17}$$

According to the first term of this expression, the dI/dV signal measured at a certain position in a given bias range provides a direct measurement of the LDOS of the sample. The second term, containing the transmission factor, constitutes a monotonic background to the signal. In practice the dI/dV signal can be directly measured using a lock-in amplifier by adding a high-frequency sinusoidal modulation (with a certain amplitude V_{mod}) to the DC bias V[46].

Low-temperature STS is routinely performed on individual molecules on surfaces to probe their electronic structure and also to map the spatial distribution of their orbitals, by recording dI/dV scans at well-defined energies (dI/dV maps). As we will discuss next, STS can also be employed to detect and quantify magnetic states and spin interactions at the single-molecule level.

1.5.1 Fingerprints of magnetism: Kondo effect and inelastic spin excitations

In differential conductance measurements, a typical signature of a localized spin state in a molecular system is the zero-bias resonance associated with the *Kondo effect*. This feature arises from the screening of a magnetic impurity by the conduction electrons of the metal substrate, which leads to a collective $S = 0$ ground state[59,60].

The Kondo effect, which is related to the increase in resistance observed at low temperatures in metals containing magnetic impurities, was first explained by J. Kondo[61], and later described by P.W. Anderson in the single impurity model[62]. This model represents the magnetic impurity as an unpaired electron with spin $S = 1/2$ occupying a certain energy state. The exchange processes with the electrons of the metal substrate lead to constant fluctuations of the impurity's spin, resulting in a many-body $S = 0$ ground state. This is manifested in the dI/dV as a resonance at the Fermi energy, since the electrons close to E_F are those involved in these scattering processes.

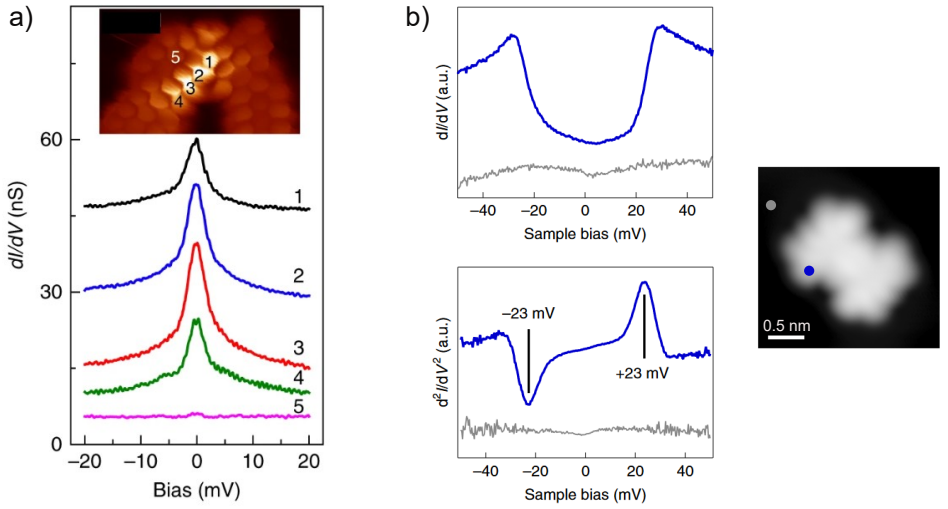

Figure 1.7: (a) Kondo resonances revealed by STS in correspondence of the bright regions appearing in the low-bias BR-STM image of a graphene nanoribbon junction. These spectral features indicate the presence of a localized magnetic moment. Adapted from [58]. (b) dI/dV (top) and d^2I/dV^2 (bottom) spectra measured on the Clar's goblet (constant-current STM image on the right), revealing inelastic spin excitation features at ± 23 mV. Such features can be ascribed to a singlet-triplet transition. Furthermore, being the molecule a diradical, the energy onset of the excitation corresponds to the effective exchange coupling between the two spins $J = 23$ meV. Adapted from [23].

It has been shown that a good description of the lineshape of the Kondo resonance is provided by the *Frota* function[63]

$$F(V) \propto \mathrm{Im}\left[ie^{i\varphi}\sqrt{\frac{i\Gamma_{\mathrm{Frota}}}{(eV - E_K) + i\Gamma_{\mathrm{Frota}}}}\right], \tag{1.18}$$

where φ is a phase factor, associated to the asymmetry of the lineshape, and E_K denotes the center of the resonance. Γ_{Frota} is related to the half width at half maximum (HWHM) of the resonance by the relation $\mathrm{HWHM} = 2.542\Gamma_{\mathrm{Frota}}$.

An example of Kondo resonance revealed in STS on a graphene nanostructure, due to the presence of a $S = 1/2$ spin state, is reported in Figure 1.7a. It is important to note, however, that Kondo resonances can be also detected in the presence of higher spin state ($S > 1/2$), as a manifestation of the so-called *underscreened* Kondo effect[57,64], as will be shown in Chapter 3.

Another spectral signature of the emergence of magnetism in a nanostructure is the presence of bias-symmetric steps associated with inelastic spin excitations. So far, we have described STS only in terms of elastic processes;

however, the tunneling electrons can also lose part of their energy, inducing inelastic excitations in the system. This case refers to inelastic electron tunneling spectroscopy (IETS)[46,65–67].

The inelastic transitions are manifested in dI/dV spectra as step-like increases in conductance (and, therefore, peaks in the d^2I/dV^2 spectra) above the threshold corresponding to the energy of the excitation. In the context of magnetism in graphene nanostructures, the appearance of these features is generally attributed to the interaction between spins, since the excitations can be related to spin-flip processes or, more broadly, to transitions between different spin states of the system. An example of inelastic features attributed to a singlet-triplet transition is reported in Figure 1.7b.

The characteristics of IETS spectra provide useful information on the spin configuration of the molecule. In particular, the energy onset of the excitation generally allows us to quantify the coupling between the electrons, as we will see in some examples in the next chapters. It is important to note also that not all spin transitions are allowed in IETS. The conservation of angular momentum requires that spin excitations induced by single-electron inelastic processes follow the selection rules $\Delta S = 0, \pm 1$ and $\Delta S_z = 0, \pm 1$[27].

1.6 On-surface synthesis

The development of on-surface synthesis (OSS) represents one of the key factors contributing to the recent progress in the experimental investigation of magnetic carbon nanostructures. As depicted schematically in Figure 1.8a, this method consists in the activation of chemical reactions on atomically clean metal surfaces in ultra-high vacuum conditions[12,21,68]. OSS enables the synthesis of molecules which are difficult to obtain using traditional in-solution chemistry, including the highly reactive open-shell nanographenes hosting one or more π radical units.

The advantages offered by OSS stem from the inert environment in which the reactions are performed, but also from the spatial confinement in two dimensions and the catalytic activity of the metal substrate, which allows for the exploration of reaction pathways that could not be easily accessible in solution. Importantly, the products of OSS can be characterized by means of scanning probe microscopy and spectroscopy, thus enabling the investigation of their properties with atomic resolution.

OSS starts with the deposition of molecular precursors onto the atomically flat surface of a suitable metal substrate. Subsequently the desired reactions, which could be either intramolecular or intermolecular, are activated, generally by thermal annealing. An example is illustrated in the scheme in Figure 1.8b,

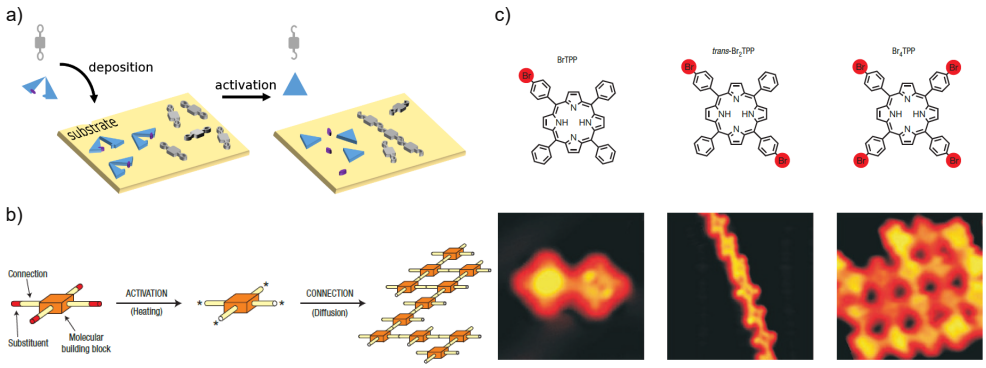

Figure 1.8: (a) Schematic representation of the typical on-surface synthesis procedure followed for growing atomically precise nanostructures. First, molecular precursors are deposited on a metal surface in ultra-high vacuum conditions; subsequently, intramolecular or intermolecular coupling reactions are activated. Adapted from [12]. (b) Scheme of the formation of covalent structures through Ullmann-like coupling on Au(111). (c) Example of the generation of dimers, one-dimensional chains and two-dimensional networks starting from mono-, di- and tetra-brominated molecular precursors. Adapted from [68].

showing the mechanism of surface-assisted Ullmann-like coupling, that represents the main reaction pathway employed in OSS to connect molecular building blocks into covalent structures. This was demonstrated for the first time in the seminal work by Grill et al. (Figure 1.8c) which showed the possibility of covalently coupling brominated molecular precursors on a Au(111) surface via annealing[68]. The reaction occurs via the dissociation of bromine atoms at elevated temperatures, leaving radicals that diffuse on the surface and create covalent bonds. As shown in Figure 1.8c, the position of the bromine atoms in the molecular precursor is crucial, since it orients the reactions and also determines the dimensionality of the final product. Indeed, in this work it was demonstrated that depending on the number and the position of these atoms, it was possible to build different types of structures, from dimers to chains to two-dimensional patches.

Another fundamental reaction in OSS, known as cyclodehydrogenation, involves intramolecular C-C coupling through dissociation of hydrogen atoms. This process closes the carbon rings of the molecular precursors, forming the zigzag edges of triangulenes or other graphene nanostructures[69–71]. We will explore this reaction in various examples of triangulene-based nanostructures investigated in this thesis.

Importantly, it is also possible to locally induce chemical reactions by stabilizing the STM tip on a well-defined position on the molecule and ramping the bias up to a certain energy threshold. This procedure is commonly used

to dissociate atoms or functional groups passivating radical units in specific molecular sites, as we will show in Chapter 2.

1.7 Experimental setup

The measurements reported in this thesis were performed with a low-temperature STM inside an ultra-high vacuum (UHV) chamber, with base pressure in the order of 10^{-10} mbar. A photograph of the system is shown in Figure 1.9.

The STM is held at $T \approx 5$ K by a thermal shield connected to a liquid helium cryostat. The entire system is surrounded by an additional liquid nitrogen bath cryostat to minimize thermal fluctuations. The STM head is suspended through three springs for isolation from mechanical vibrations. The whole UHV system is then lifted by pneumatic feet to dump low-frequency vibrations.

A sample preparation chamber is used for the *in-situ* cleaning of the metal surfaces, for molecular deposition, and thermal activation of on-surface synthesis reactions. The main substrate used in the experiments of this thesis is an Au(111) single crystal. The surface is prepared by cycles of sputtering with Ne^+ ions followed by thermal annealing at $T = 600$°C through resistive or electron beam heating. In the experiments presented here molecular deposition on the metal substrate is generally achieved through *flash evaporation* from a silicon wafer loaded with grains of the molecular compound. In this process, the silicon is heated to a high temperature for a few seconds, causing rapid evaporation of the material. This technique is particularly well-suited for large molecular structures, since the short exposition to high temperatures reduces molecular fragmentation. The more standard procedure of evaporation from a Knudsen cell evaporator was used for two triangulene precursors in Chapter 5 when performing hot sample deposition, i.e., evaporating the molecules on a substrate kept at high temperature.

The STM measurements were performed with a gold-coated tungsten tip or, when indicated in the text, with a CO-terminated tip. The STM head (from CreaTec Fischer & Co. GmbH) was controlled using Nanonis software (SPECS Surface Nano Analysis GmbH). The figures representing the experimental data were prepared using WSxM and SpectraFox softwares[72,73].

The AFM bond-resolved image and the Kelvin probe force microscopy measurements reported in Chapter 3 were performed using a qPlus-type sensor with eigenfrequency $f_0 = 30.72$ kHz and Q-factor of the order of 10^4[56]. The AFM was operated in the frequency modulation mode[74], with an oscillation amplitude of 60 pm.

The measurements under an external magnetic field (reported in Figure 3.5 in Chapter 3) as well as the STS spectrum at $T = 1.3$ K (reported in Figure 2.2 in chapter 2) were performed in a different system compared to the other experiments of this thesis, specifically in a commercial Joule-Thomson (JT) STM with a base temperature of 1.2 K.

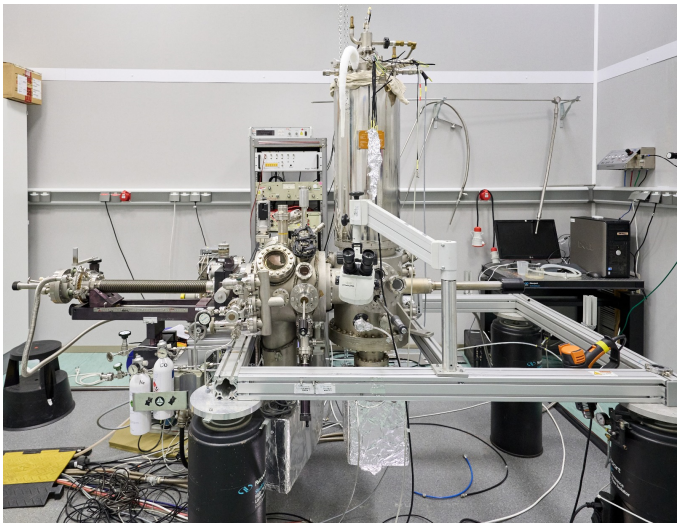

Figure 1.9: Photograph of the experimental setup, featuring the UHV system equipped with the low-temperature STM.

2 Manipulating spin interactions in the 2-OS diradical

Open-shell polycyclic aromatic hydrocarbons represent promising building blocks for carbon-based functional magnetic materials, but are also highly reactive systems, requiring structural strategies to protect their radical states from interacting with the environment. In this study, we demonstrate that the open-shell ground state of an all-organic diradical (**2-OS**) survives on a Au(111) substrate as a singlet formed by two unpaired electrons with anti-parallel spins coupled through a conformational dependent interaction. The **2-OS** molecule is a derivative of the Chichibabin's diradical, featuring a non-planar geometry that destabilizes the closed-shell quinoidal structure. Theoretical calculations reveal that the exchange coupling between the two spins strongly depends on the torsional angles between the molecular moieties, suggesting the possibility of influencing the molecule's magnetic state through structural changes. This is demonstrated here using the STM tip to manipulate the internal structural arrangement of a **2-OS** analogue, while simultaneously detecting changes in spin-spin coupling.

Part of the results reported in this Chapter are published as an article in *ACS Nano*.

- Tuning the Spin Interaction in Nonplanar Organic Diradicals through Mechanical Manipulation

  Alessio Vegliante, Saleta Fernández, Ricardo Ortiz, Manuel Vilas-Varela, Thomas Y. Baum, Niklas Friedrich, Francisco Romero-Lara, Andrea Aguirre, Katerina Vaxevani, Dongfei Wang, Carlos Garcia Fernandez, Herre S. J. van der Zant, Thomas Frederiksen, Diego Peña and Jose Ignacio Pascual.

  ACS Nano **2024** 18 (39), 26514-26521.

  https://doi.org/10.1021/acsnano.4c01963

2.1 Introduction

Carbon-based molecular nanostructures can exhibit magnetic states associated with the stabilization of unpaired electrons in radical sites[12]. Intrinsic π-magnetism has been widely observed in polycyclic aromatic hydrocarbons (PAHs) with an open-shell ground state, i.e., possessing one or more unpaired π electrons[23,27,58,75]. In this context, organic diradicals are of fundamental interest for understanding magnetic interactions at the molecular scale and developing control strategies[76].

A classical example of open-shell PAH is the Chichibabin's hydrocarbon, a molecule that has been extensively investigated for its large diradical character in the ground state[77,78]. To circumvent its high reactivity, several derivatives have been prepared, one of the latest examples being a stable compound reported by Zeng et al. (**2-OS**, Figure 2.1a)[79]. The **2-OS** molecule consists of a central bisanthracene unit linked to two fluorenyl termini that accumulate the radical character of the system. The steric hindrance between fluorenyl and anthracene moieites determines a highly non-planar structure that is responsible for the protection of the radical centers, which remain localized over the fluorenyl sub-units. Owing to high stability of its diradical ground state and its tuneable non-planar structure, **2-OS** is a suitable system to explore the relationship between magnetism and geometry at the single molecule scale.

A triplet ground state has been reported for **2-OS** in solution, in agreement with DFT calculations of the magnetic state of the molecule in the gas phase[79]. Recently, **2-OS** has also been studied in mechanically controlled break-junction devices[80], where spectroscopic features of either the singlet or triplet ground state have been detected. These variations in the sign of the magnetic exchange have been attributed to different torsional angles between the different conjugated moieties[80], enhanced by the contacts to metallic terminals[81], but a clear demonstration of the correlation between magnetic exchange and structure is lacking.

In this chapter, we demonstrate that the spin-spin coupling in the **2-OS** diradical can be manipulated by modifying its conformational structure. Low-temperature scanning tunneling microscopy measurements show that the open-shell character of **2-OS** persists on a Au(111) substrate with a singlet ground state very close in energy to a triplet excited state. Mean-Field Hubbard simulations reveal the influence of molecular geometry on the exchange coupling between the radical centers. Following these findings, we demonstrate the possibility of tuning the spin state of the molecule by modifying the arrangement of its constituent units through mechanical manipulation with the STM tip. For this purpose, we introduce a **2-OS** analogue functionalized with suitable

anchoring end groups and manipulate its structure by partially lifting it from the substrate, either by exerting attractive forces or by forming a bond with the tip. Finally, we explore the possibility of manipulating the spin interaction in the diradical by modifying its chemical structures, specifically reducing the distance between the radical units.

2.2 On-surface synthesis and characterization of 2-OS

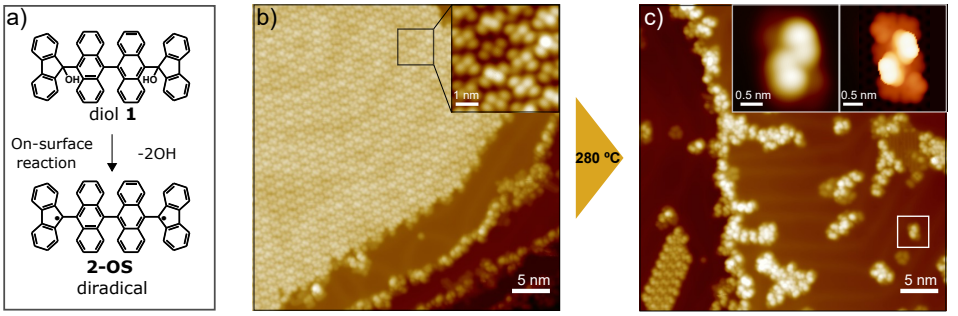

Figure 2.1: (a) Schematic representation of the generation of the **2-OS** diradical through dissociation of the OH groups from the diol **1** deposited on the Au(111) substrate. (b) Overview STM constant-current image displaying the typical close-packed domain formed by the molecular precursors when deposited on the Au(111) surface ($V = -1.25$ V; $I = 46$ pA). In the inset, close-packed structure showing the arrangement and the shape of the individual molecules ($V = -1.25$ V; $I = 30$ pA). (c) STM constant-current image recorded after annealing the sample at 280°C ($V = -1.25$ V; $I = 30$ pA). In the inset: left, STM image of a single isolated molecule as found after the annealing ($V = -1.25$ V; $I = 30$ pA); right, DFT charge density calculation of **2-OS** on Au(111).

Evaporating di- and poly-radicals onto a substrate is known to be particularly challenging, as it easily results in fragmentation due to thermal instability[82,83]. In order to get intact **2-OS** molecules on a Au(111) surface, we sublimated diol **1**, a stable molecular precursor containing a hydroxyl group (OH) capping each of the two radical centers at the fluorenyl termini, and subsequently induced an on-surface reaction to dissociate the OH groups and generate **2-OS**, as shown schematically in Figure 2.1a. [1]

The diol **1** was evaporated onto a clean Au(111) surface under ultra-high vacuum (UHV) conditions. Extended close-packed molecular domains were found on the Au surface after the sublimation, as revealed by constant-current

[1] In-solution synthesis of the **2-OS** molecular precursor performed by Saleta Fernández and Diego Peña (CiQUS and Universidade de Santiago de Compostela, Santiago de Compostela, Spain).

STM images (Figure 2.1b). A closer look into these structures shows that the constituent molecules appear partially planarized, and display four lobes: the two internal ones can be attributed to the anthracene units and the ones at the ends to the fluorenyl termini. The sample was thus annealed with the aim of inducing the C-OH cleavage, in a similar manner to the deoxygenation reaction previously described for epoxyacene derivatives[84]. Figure 2.1c shows an overview after annealing at 280°C: some close-packed domains of reduced dimensions can still be seen, alongside single isolated molecules, chains and small molecular clusters of several shapes. Individual molecules appear in constant-current STM images as shown in the inset in Figure 2.1c: they feature two internal brighter lobes, that can be attributed to the anthracene moieties, and darker external features, corresponding to the fluorenyl termini. A more detailed elucidation of the molecular structure with bond resolution is hindered by the non-planarity of the system. However, our DFT simulations of the charge density of **2-OS** on the Au(111) surface (also reported in Figure 2.1c) is in good agreement with the main features found in the STM topography, confirming our identification of the individual molecules.

Two distinct molecular structures are generally found after the annealing step, corresponding to one or both OH groups detached following the on-surface reaction (Figure 2.2a,d). The STM constant-current images appear roughly the same in the two cases; nevertheless, scanning tunneling spectroscopy allows the identification of two distinct spin states, that can be related to the two configurations with different numbers of OH groups left.

In a fraction of molecules (around 25% of the single molecules that have been investigated, Figure 2.2a), the dI/dV spectra display a pronounced zero-bias peak, as depicted in Figure 2.2b. This feature is well reproduced by a Frota function with $HWHM = 6.1$ meV, and can be attributed to a Kondo resonance, arising from the screening of a localized spin $S = 1/2$ by the conduction electrons of the metal substrate[57,58,60,61,63]. The dI/dV stacked plot taken along an axis of the molecule (Figure 2.2c) shows that the Kondo resonance is not spatially homogeneous but significantly more intense in one half of the molecule. We relate this spin state to a monoradical structure in which one OH group persists after the annealing and therefore conclude that the Kondo resonance is associated to the single unpaired electron recovered from the partial OH dissociation.

However, most of the individual molecules found after annealing (Figure 2.2d) display a distinct low-energy feature consisting of a narrow gap centered at zero-bias, followed by two sharp dI/dV peaks at ± 11 meV, as depicted in Figure 2.2e. The dI/dV stacked plot in Figure 2.2f reveals that these features appear distributed all over the molecule, weaker over the center

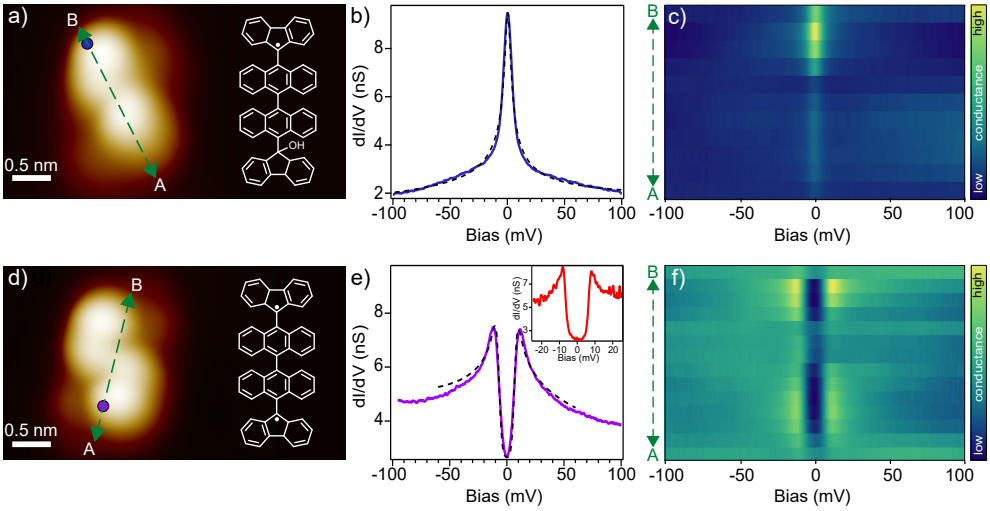

Figure 2.2: (a,d) STM constant-current images ($V = -1.25$ V; $I = 30$ pA) of single molecules as found after the on-surface reaction and the corresponding molecular structures, in the two configurations: (a) with a residual OH group, corresponding to a monoradical, and (d) with no OH groups, corresponding to the **2-OS** diradical. (b) dI/dV spectrum taken on the molecule in (a) at the position indicated by the blue circle, displaying a zero-bias resonance, that can be fitted with a Frota function (black dashed line)[63]. (c) dI/dV linescan measured across the molecule in (a) in the direction indicated by the arrow ($V = -200$ mV, $I_{set} = 500$ pA, $V_{mod} = 2$ mV). (e) dI/dV spectrum measured on the molecule in (d) at the position indicated by the purple circle, showing spin excitation steps. The black dashed line represents fits to the data using the perturbative model by Ternes[85], from which an antiferromagnetic exchange $J = 7.3$ meV is obtained. The inset shows a spectrum measured at $T = 1.3$ K, emphasizing the IET gap (V=30 mV, $I_{set} = 200$ pA, $V_{mod} = 0.8$ mV). (f) dI/dV line spectra measured across the molecule in (d) in the direction indicated by the arrow ($V = -100$ mV, $I_{set} = 500$ pA, $V_{mod} = 2$ mV).

of the molecule but with higher amplitude towards the fluorenyl end-groups. Based on the symmetric position of the dI/dV peaks, we attribute these features to an inelastic excitation of the two exchange-coupled spins at the radical sites[27,58,67,86–88], confirming that in this case both OH groups have been detached, activating the **2-OS** diradical.

We note that dI/dV spectra exhibit a higher-bias characteristic fall-off, resembling a Kondo resonance superimposed on the gapped spectrum[58,87]. Furthermore, such Kondo-like feature is absent at zero bias (see STS spectrum recorded at 1.3 K in inset in Figure 2.2e). This indicates that the Kondo-like fluctuations are enabled by inelastic electrons tunneling through the excited state[60,81,89] but are absent in the ground state. The spectral shape can be interpreted as caused by the inelastic excitation of a singlet (total spin $S = 0$)

ground state into a triplet ($S = 1$) excited state. A model of two antiferromagnetically coupled 1/2 spins[85] (dashed line in Figure 2.2e) reproduces well the spectral features, revealing an exchange interaction between the flourenyl moieties of $J \sim$ 7.3 meV. Therefore, we conclude that **2-OS** on a Au(111) surface exhibits a singlet ground state, excluding the previously observed triplet ground state[79], since this would result in a very different spectral lineshape.

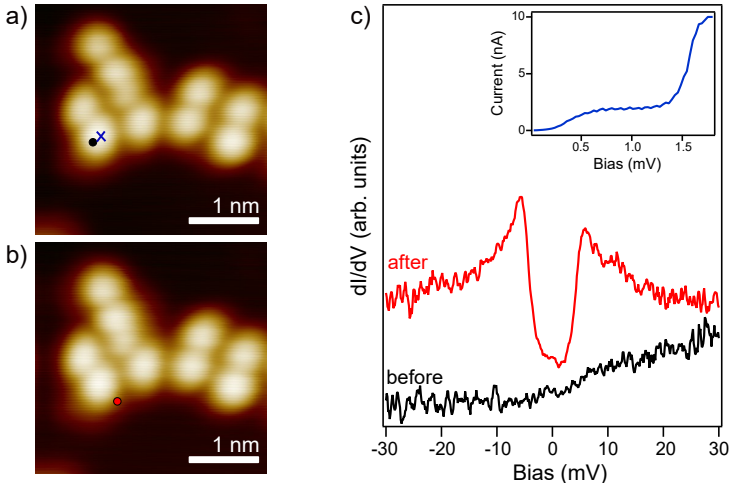

Figure 2.3: On-surface generation of **2-OS** by electron-induced C-OH cleavage. (a) Constant-current STM image of a small island of precursor molecules. The blue cross indicates the position where the tip is stabilized (setpoint: $V = 30$ mV, $I = 10$ pA) before sweeping the bias. (b) Constant-current STM image of the same area after the bias sweep. (c) dI/dV spectra measured before (black) and after (red) the bias sweep from 30 mV to 2 V at the positions indicated in (a,b) by the corresponding circles. The inset shows the variation of the tunneling current during the process. After the bias sweep, the diradical is generated, as clearly demonstrated by the appearance of the IET steps attributed to the two exchange-coupled spins. This experiment was performed at $T = 1.3$ K. Topography parameters: $V = 2$ V; $I = 10$ pA. Spectroscopy parameters: $V_{mod} = 0.8$ mV, $I_{set} = 200$ pA.

Finally, we explored an alternative approach for the on-surface generation of **2-OS**, consisting in inducing the C-OH cleavage by means of spatially controlled voltage pulses, as illustrated in Figure 2.3. We identify a small domain of precursors, then place the tip on top of a molecule and slowly raise the sample positive bias above 1.5 V, until we detect a steep increase in the tunneling current. The dI/dV spectrum recorded after the bias sweep displays the IET features attributed to the singlet-triplet excitation (Figure 2.3)c, thus indicating the formation of the diradical. We found out that this procedure allows us to remove one or more OH groups in the same molecule or in neighboring molecules within the assembled domains and clusters, but does not provide

isolated molecules over the Au surface. Therefore, our analysis here is based on single **2-OS** molecules generated by annealing the substrate.

2.3 Geometry-dependent spin coupling

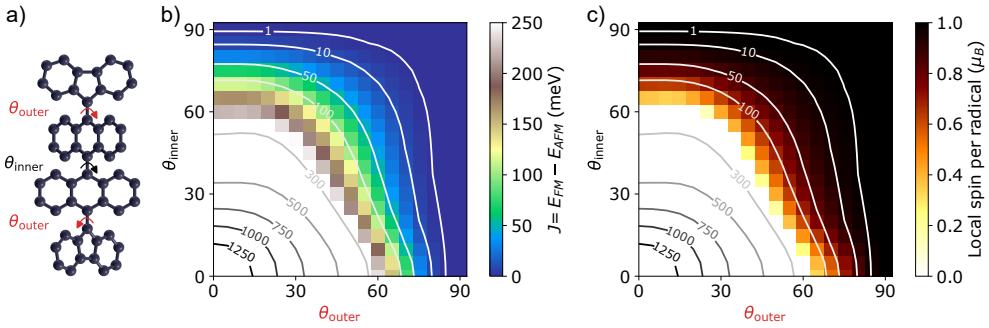

Figure 2.4: TB-MFH calculations for the exchange coupling as a function of torsional angles in **2-OS**. (a) Structural model for the **2-OS** carbon backbone with three torsional angles. For simplicity, we fix the two outer angles θ_{outer} to be identical. (b) MFH results for the intramolecular exchange coupling $J = E_{\text{FM}} - E_{\text{AFM}}$ between the two radicals, obtained using a value of $U = 3$ eV[90], as a function of the two torsional angles θ_{outer} and θ_{inner}. The value of J is obtained as the energy difference between ferromagnetic (FM) (solution constrained to $S_z = 1$) and antiferromagnetic (AFM) order (solution constrained to $S_z = 0$). The contours represent constant-J in meV: the AFM solution is always the ground state, but J approaches zero whenever one of the two angles reaches $90°$. (c) Local spin polarization per radical (defined as the sum of the spin density over sites on one half of the molecule) in the AFM state, as a function of the two torsional angles θ_{outer} and θ_{inner}. The constant-J contours from (b) are also included here as a guide. For $J \gtrsim 200$ meV the ground state becomes a closed-shell singlet (no local polarization).

To explain the origin of the antiferromagnetic coupling found on the Au substrate, we performed tight-binding mean-field Hubbard (TB-MFH) simulations of the magnetic ground state of **2-OS** in different geometries.[2] Specifically, we calculated the energy of the antiferromagnetic (AFM, the singlet case) spin arrangement with respect to the ferromagnetic (FM, the triplet solution) case, i.e., $J = E_{\text{FM}} - E_{\text{AFM}}$, as a function of the dihedral angles θ_{inner} (between the central anthracenes) and θ_{outer} (between each anthracene and the outer fluorenyl). For simplicity, we assumed the two outer angles to be identical and the individual anthracenes and fluorenyls units to be planar. We considered a single p-orbital per carbon site, locally perpendicular to the

[2]Calculations performed by Ricardo Ortiz and Thomas Frederiksen (Donostia International Physics Center, San Sebastián, Spain).

backbone unit and constructed the corresponding TB Hamiltonian with SISL[91] using the Slater-Koster parametrization of [92].

The variation of J as a function of the two torsional angles is depicted in Figure 2.4b. The singlet is always the ground state (ΔE_{ST} is always positive). for any combination of θ_{inner} and θ_{outer}. However, we observe a clear trend in the evolution of J with the conformation: its value is close to 0 when any of the torsional angles approach 90°, but it progressively increases as the angles reduce. This means that the planarization of the molecular structure (i.e. the decrease of the angles between the units) stabilizes the singlet solution, unveiling an increasingly higher AFM exchange coupling. According to the TB-MFH results shown in Fig. 2.4c, the effect of planarization is drastic: the spin polarization vanishes for angles below 60°, revealing that for smaller angles, the open-shell singlet transforms itself into a (spin-unpolarized) closed-shell singlet.

The experimental observation of a singlet ground state for **2-OS** on Au(111) is in agreement with the trend obtained in the MFH simulations. The interaction with the flat metal substrate is expected to induce a partial planarization of the molecular units (see the DFT calculation of the adsorption geometry in the Appendix, Section 2.8.2), contributing to the stabilization of the AFM order.

From TB-MFH results, the FM solution is always less energetically favorable than the AFM one, even for high values of the torsional angles. This apparently contradicts results from previous DFT calculations, which found a triplet ground state in the gas phase, with a triplet-singlet gap of 26 meV[79]. This discrepancy is explained by considering that the value reported by Zeng et al.[79] takes into account also vibrational effects due to temperature. Including these in our DFT simulations, we reproduced the higher stability of the triplet ground state for a gas-phase relaxed molecule (i.e. with both angles $\theta_{\text{i}} \sim 90°$) and at room temperature (shown in the Appendix, Section 2.8.3). At the lower temperature of our experiment, however, vibrational effects do not play a significant role, and DFT qualitatively reproduces the results of the TB-MFH calculations.

In any scenario, all simulation tools agree that decreasing the torsional angle of the molecular subunits stabilizes the singlet state. As shown in Figure 2.17, this can be explained by the increase in hopping elements across the dihedral angles. These matrix elements primarily enhance kinetic exchange mechanisms, which induce AFM ordering in **2-OS**, while direct Hund's like exchange is expected to be negligible[41,81,93]. Following these theoretical results, the controlled modification of the spin interactions should be achievable by tuning the molecular configuration.

Motivated by the theoretical predictions indicating a correlation between the geometry of **2-OS** and the exchange coupling J, we explored the possibility of modifying its spin excitation gap and magnetic ground state by manipulating the molecular conformation using the STM tip. We note that the non-planar structure of **2-OS** arises from hindrance among different conjugated units, imposing the persistance of a dihedral angle even on the metal substrate (see Figure 2.18). Consequently, we anticipated that approaching the STM tip towards the central part of the molecule would exert attractive or repulsive forces over these submolecular units, forcing variations of their dihedral angles[94,95], as observed in our DFT simulations in the Appendix Figure 2.19.

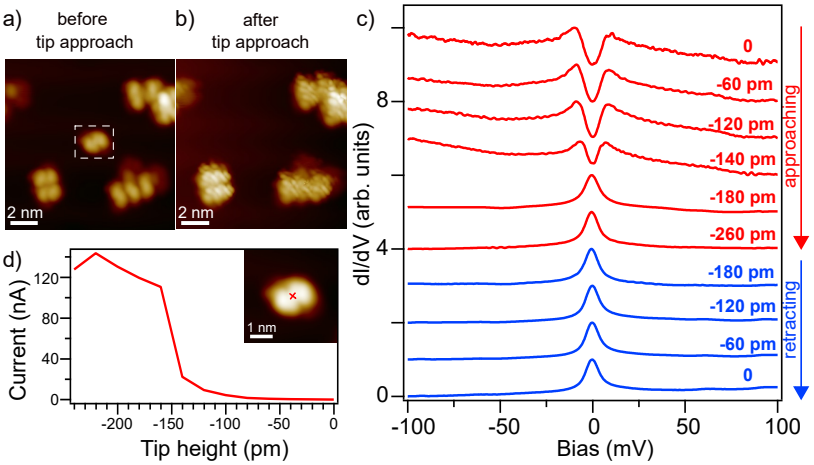

Figure 2.5: Manipulation experiments on **2-OS**. (a) Constant-current STM image of the molecule on which the tip approach experiment is performed, as seen before starting the process ($V = -1.25$ V; $I = 30$ pA); (b) Image of the same area after the manipulation, showing that the molecule has been picked up by the tip. (c) Stack of normalized dI/dV spectra recorded during the approach-retract experiment in the position indicated by the cross in the inset in (d), as described in the text. Red curves are recorded during the approach phase, blue curves during retraction. (d) Current measured at different tip heights (with constant tip-sample bias $V = 100$ mV) while approaching the tip. The sharp increase at -150 pm coincides with the change of magnetic fingerprint in the dI/dV spectra, as shown in panel c). Spectroscopy parameters: $V_{mod} = 2$ mV, $I_{set} = 200$ pA.

However, we found that **2-OS** molecules were abruptly modified, and frequently displaced towards the STM tip in response to attractive forces, due to the weak interaction with the surface. This is shown in Figure 2.5, where we report one of such manipulation experiments on an individual **2-OS** molecule. The manipulation procedure is the following: we stabilize the tip above the central units of **2-OS**, in the position indicated by the cross in the inset in Fig-

ure 2.5d, at a starting height ($z = 0$) determined by a setpoint of $V = 100$ mV and $I = 200$ pA; then we approach towards the molecule in steps of 20 pm, measuring dI/dV spectra at each step, and finally rectract back to the starting point. We can observe the appearance of a Kondo peak and simultaneous disappearance of the IET steps at -180 pm. The Kondo feature persists while retracting the tip back to the starting position. This suggests that the change in the spectral feature is due to the quenching of one of the two radicals upon formation of a tip-molecule contact, as confirmed also by the image recorded at the end of the process (Figure 2.5b), which shows that the molecule has been picked up during the process.

2.4 SMe-2OS: a candidate for mechanical manipulation

To overcome the issues related to the high mobility of **2-OS**, we designed an extended version of the diradical, denoted **SMe-2OS** (Figure 2.8a), wherein methylthiophenyl moieties were strategically incorporated at each fluorenyl sub-unit. These moieties were chosen since sulfur groups are widely used for anchoring molecules to gold electrodes[96–98].

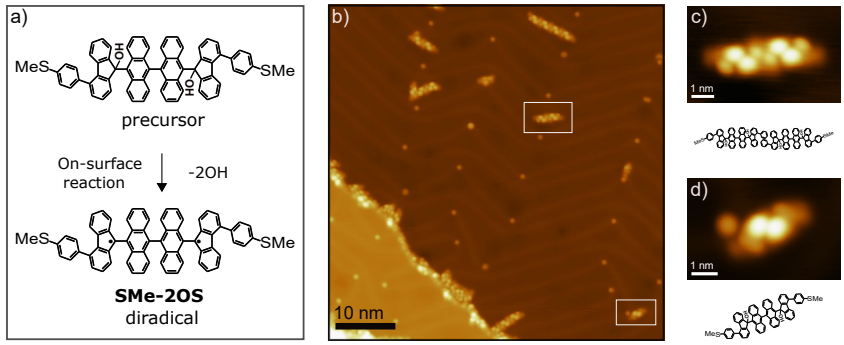

Figure 2.6: (a) Schematic representation of the on-surface generation of the **SMe-2OS** diradical through dissociation of OH protecting groups from the correspondent precursor. (b) Overview STM constant-current image after deposition, revealing chain-like self-assembled structures and an individual molecule ($V = 1$ V; $I = 30$ pA). (c) Image of the self-assembled dimer marked in (b), and possible chemical structure, suggesting the removal of an end group from each molecule. (d) Close-up image of the individual molecular precursor and corresponding chemical model. Isolated intact precursors are generally found close to fragments (the round shaped feature appearing here on the left).

Similar to the **2-OS** base molecule, we generated the **SMe-2OS** diradical on the Au(111) surface starting with a closed-shell precursor containing OH

protecting groups at the two radical sites (chemical model in Figure 2.6a).[3] In this case, the evaporation on the Au(111) substrate resulted mostly in small self-assembled chain-like structures instead of large close-packed domains, as shown in Figures 2.6b-c. Interestingly, we also observed some isolated precursors, generally found close to round features, which could be attributed to gold adatoms captured by the SMe groups (Figure 2.6d). Due to the availability of single molecules on the surface, we activated the OH decapping reactions by applying controlled bias pulses over the molecular moieties.

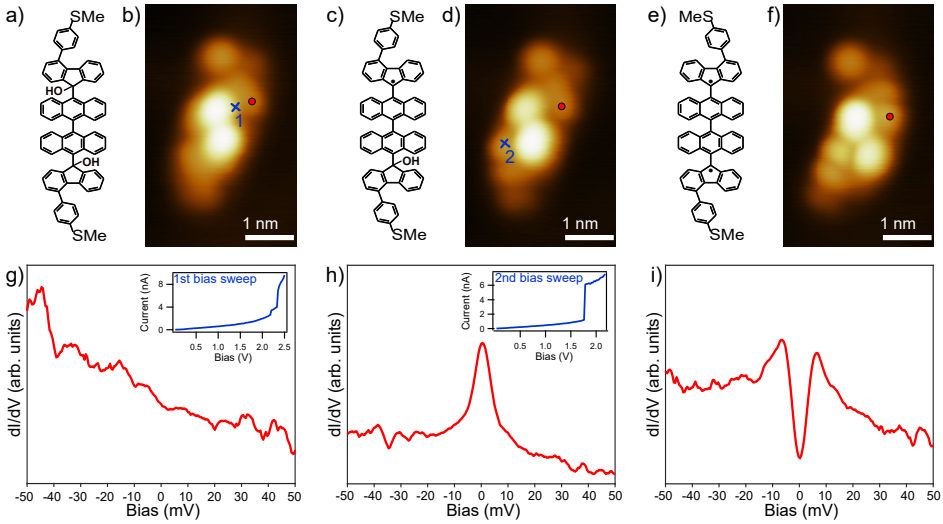

Figure 2.7: On-surface generation of **SMe-2OS** by sequential electron-induced C-OH cleavage. (a-c-e) Chemical models at the different steps of the reaction, (b-d-f) corresponding constant-current STM images and (g-h-i) low-bias dI/dV spectra measured at each step in the positions indicated by the red circles in the STM images. First, the tip is stabilized in the position indicated by the blue cross in (b) (setpoint: $V = 30$ mV, $I = 10$ pA) before opening the feedback and raising the bias above 30 mV. The inset in (g) reports the variation of the tunneling current during the bias sweep: the sudden jump at 2.3 V indicates the C-OH cleavage. The dI/dV spectrum measured after the first bias sweep (h) shows a Kondo peak that emerges as a consequence of the removal of one OH group. After the second bias sweep, performed at the position marked by the cross in (d), clear IET features appear in the dI/dV spectrum (i), indicating the dissociation of the second OH group. The variation of the current as a function of the bias (ramping from 30 mV to 2.1 V) is reported in the inset. Topography parameters: $V = 1$ V; $I = 30$ pA. Spectroscopy parameters: $V_{mod} = 2$ mV, $I_{set} = 500$ pA.

As illustrated in Figure 2.7, the decapping proceeds as follows: we first bring the tip to the position corresponding to a fluorenyl unit and, after open-

[3] In-solution synthesis of the **SMe-2OS** molecular precursor performed by Manuel Vilas-Varela and Diego Peña (CiQUS and Universidade de Santiago de Compostela, Santiago de Compostela, Spain).

ing the feedback, we slowly increase the tip-sample bias voltage, until we observe a jump in the current (inset in Figure 2.7g), signalling the activation of the C-OH cleavage. The dI/dV spectrum measured afterwards (Figure 2.7h) displays a resonance that can be attributed to a S=1/2 Kondo, thus confirming the generation of a monoradical. We repeat the same procedure on the opposite fluorenyl unit (as shown in Figure 2.7d) and measure a new dI/dV spectrum: now, similarly to **2-OS**, clear spin excitation features are observed, indicating the presence of two coupled spins. It is important to point out that the pulse-induced generation of **SMe-2OS** presented here appears more controlled and reproducible compared to the analogous procedure for **2-OS** illustrated in Figure 2.3, due to the absence of neighbouring molecules and to the stronger anchoring to the substrate provided by the SMe groups.

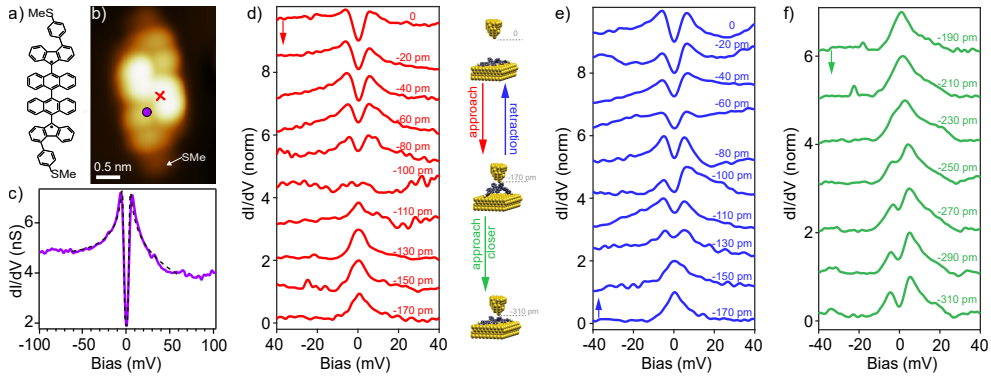

Figure 2.8: Manipulation experiments on **SMe-2OS**. (a) Chemical model of **SMe-2OS**, the sulfide substituted analogue of **2-OS** synthesized for the manipulation experiment. (b) STM image ($V = -1.25$ V; $I = 30$ pA) of **SMe-2OS**, as obtained after the on-surface generation of the diradical. (c) dI/dV spectrum measured on the molecule at the position indicated by the purple circle in (b), displaying the same IET feature as **2-OS**. The black dashed line is a fit to the data using the perturbative model by Ternes[85], revealing an antiferromagnetic exchange $J = 3$ meV. (d-f) Mechanical manipulation of the spin state of **SMe-2OS**, as indicated in the central scheme. The STM tip is stabilized on the molecule in the position marked by the red cross in (b) at a starting height (here indicated as 0) determined by $I = 200$ pA and $V = 50$ mV. dI/dV spectra are measured after approaching the tip by the indicated distances, in three sequences: (d) while approaching the tip down to 170pm with respect to the starting position; (e) when retracting back towards the starting position; (f) while continuing approaching to lower tip-sample distances from the end of (d). At some positions, a peculiar IET peak asymmetry is observed, attributed to particle-hole asymmetries[99], probably caused by the coupling to the tip[86]. Spectroscopy parameters: $V_{mod} = 2$ mV, $I_{set} = 200$ pA.

The STM constant-current images of the resulting **SMe-2OS** molecules, shown in Figure 2.7f and in Figure 2.8b, reveal bulky features similar to those of the **2-OS** species. However, they also display two additional lobes (one

bright and one darker) at each end, which can be attributed to the methylthiophenyl end groups.

The differential conductance spectra measured on **SMe-2OS** (Figure 2.8c) reproduce similar features as in **2-OS**, namely, IET onsets attributed to singlet-triplet spin excitation, accompanied by a dI/dV decrease characteristic of Kondo fluctuations in the excited state. This confirms that the addition of the edge groups preserves the magnetic ground state of **2-OS**. The singlet-triplet gap in **SMe-2OS** is ~ 3 meV, thus smaller than on **2-OS**. Owing to the strong sensitivity of the intramolecular exchange with the conformation reported in Figure 2.4, the smaller value of J reflects the slightly larger values of torsional angles in the relaxed structure of **SMe-2OS** on gold, probably induced by the bonding of SMe end groups with the substrate.

To study the evolution of spin interactions in **SMe-2OS** as a function of structural changes, we stabilized the STM tip above the center of the molecule (red cross in Figure 2.8b) and performed dI/dV measurements while the STM tip was approached to or retracted from the molecule in steps of 10 or 20 pm. Figure 2.8d displays spectra measured while approaching the tip 170 pm from the starting position. The width and depth of the excitation gap decreases along the first approaching steps until collapsing into a zero-bias peak at 100 pm. This change can be interpreted as a transition to a new spin state of **SMe-2OS** caused by the structural modification induced by the STM tip. The approach of a tip to a molecular adsorbate is known to cause attractive forces of tens of piconewtons[100], which can induce detectable distortions in the structure of the adsorbed molecules[101,102]. In the present case, vertical forces rearrange the internal anthracene units into a less planar conformation, as shown in the schematic representation of Figure 2.8 d. DFT simulations shown in the Appendix (Figure 2.19) find that the major distortion caused by the approach of an arbitrary STM tip is an increase in both inner and outer dihedral angles. As suggested by the MFH results, an increase in one or both the torsional angles results in the reduction of the intramolecular spin-spin coupling. Therefore, the zero-bias peak observed in the final steps of the approach can be attributed to a Kondo-like feature, emerging when the two spins become non-interacting.

The mechanical manipulation of the spin state of the diradical is reversible (Figure 2.8e). Retracting the tip back to the starting position restores the initial inelastic spectral features, thus indicating that the molecule is brought back into the original conformation stabilized by the substrate. The reversibility of this process demonstrates that the change in the spectra is caused by mechanical modifications rather than by the formation of a tip-molecule bond (and consequent quenching of a spin).

The antiparallel spin configuration is restored back when the STM tip is moved further towards the molecule from the closest point in Figure 2.8d. Figure 2.8f shows dI/dV spectra measured while approaching the tip from 190 pm to 310 pm from the starting position in Figure 2.8d. In this range, the Kondo peak gradually develops a gap, opening as the STM tip approaches, attributed to the reactivation of an inelastic spin excitation. This indicates that the molecule is gradually pushed back towards the substrate, progressively restoring the original torsional angles between the central anthracenes and recovering the antiparallel spin interaction. This agrees with previous non-contact AFM results[100], which revealed that attractive forces in the tip-sample junction persist for about 300 pm of tip approach before entering a regime of repulsive interactions. Curiously, this gap-reopening is smooth, in contrast to the first range of the approach (Figure 2.8d), where a sudden gap closing occurred. This suggests that the dihedral angle can be tuned gradually in the range of pushing, while during the initial pulling regime, the attractive forces acting at larger distances induce a more sudden structural reorganization.

These results demonstrate that the spin-spin coupling in **2-OS** can be tuned using mechanical manipulation reversibly, confirming the theoretical prediction of a strong interplay between precise structural conformation and magnetic state.

2.5 Tuning the spin interaction in two-terminal transport measurements

We further explored the mechanical manipulation of the spin state of **SMe-2OS** by conducting *lifting* experiments. It has been shown in several works that the STM tip can be used to contact a molecule and partially lift it from the substrate in a controlled manner. In this way a molecular junction is created and two-terminal transport experiments can be performed[103–105]. In our case, this procedure allows us to probe the spin state of the system while progressively reducing the partial planarization induced by the substrate and thus recovering conformations closer to the gas phase. The presence of the methylthiophenyl groups at the terminations of the molecule is particularly suitable for this purpose, since it allows to create stable tip-molecule contacts without quenching the radical units, which are mostly delocalized over the fluorenyl moieties.

Furthermore, an interesting advantage offered by this procedure is the possibility of reproducing experimental configurations similar to those obtained in break-junction devices, where a single molecule is suspended be-

tween two metal electrodes. The **2-OS** diradical has been previously studied in mechanically-controlled break junction (MCBJ) experiments, where different spin states were detected depending mostly on the position and geometry of the molecule within the junction[80]. This technique allows the exploration a wide range of molecular conformations due to the high variability of the geometry of the molecule-electrode contacts. However, it lacks the spatial resolution, single-molecule control, and high reproducibility provided by STM. Therefore, in this section we will also compare the results from STM lifting experiments on **SMe-2OS** with those obtained in the same molecule in an MCBJ setup, to establish a link between the two techniques. [4]

2.5.1 Lifting SMe-2OS with the STM tip

We start the experiment by activating the diradical state of an isolated **SMe-2OS** precursor via tip-induced reactions, as described in the previous section. Then, we stabilize the STM tip on one edge of the molecule at $V = 500$ mV and $I = 30$ pA, in correspondence to a sulfur atom, and open the feedback loop (Figure 2.9a). After reducing the tip-sample bias to $V = 30$ mV, we start approaching towards the molecule in controlled steps of 10 pm, while simultaneously recording the tunneling current signal, as illustrated in Figure 2.9c, until a sudden increase in the current is detected. This indicates the formation of a chemical bond between the tip apex and the molecule, as confirmed by the conductance detected while retracting the tip, which is always higher than the one measured at the corresponding tip heights during the approach[103,104]. The most probable chemical process occurring here is the removal of the methyl group followed by the formation of a Au-S bond, which is expected to provide a robust and stable contact for the transport measurements[98].

To study the evolution of the spin-spin interaction while partially lifting **SMe-2OS** from the substrate, we recorded low-bias dI/dV spectra at each retraction step. After the jump to contact (tip height z=0), the usual spin excitation feature is still observed, with a gap of 3.3 meV, demonstrating the preserved diradical character upon formation of the tip-molecule bond. In the first stages of the tip retraction (up to $z = 170$ pm), the dI/dV spectra keep displaying the same features, although with changes in their lineshape, particularly in the bias overshoots on top of the IET peaks, likely due to variations of the Kondo exchange coupling with the substrate (Figure 2.9d). Interestingly, after retracting the tip 200 pm, the IET feature starts to change,

[4]The MCBJ measurements were performed by Thomas Y. Baum in the group of Herre van der Zant at Delft University of Technology (Delft, The Netherlands) and reported in his PhD thesis[106].

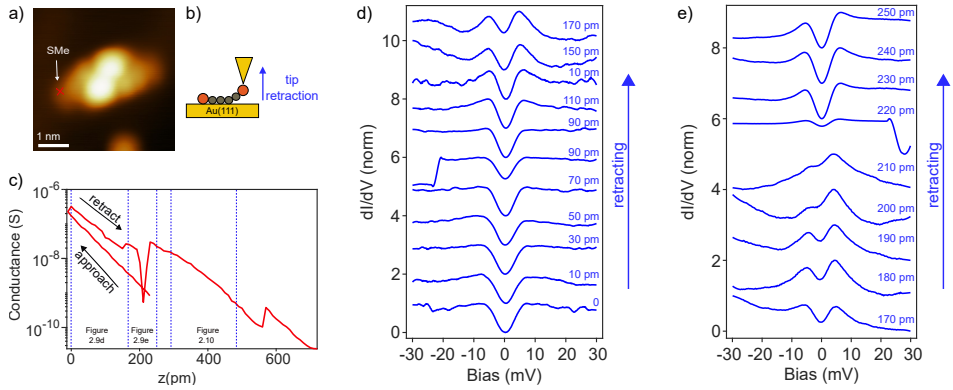

Figure 2.9: (a) STM constant-current image ($V = -1.25$ V; $I = 30$ pA) of an isolated **SMe-2OS** molecule. (b) Schematic model of the manipulation experiment described in the text. (c) Conductance measured at different tip heights z, while approaching the tip towards the molecule and during the subsequent retraction steps. The position at which the tip-molecule contact is formed is indicated as 0. (d) dI/dV spectra recorded at different z (as indicated for each curve) in the first range of retraction, from the jump to contact to $z = 170$ pm. (e) dI/dV spectra measured from $z = 170$ pm to $z = 250$ pm. The z limits of both sets of spectra are indicated as dashed lines in the conductance curve in (c). Spectroscopy parameters: $V_{mod} = 2$ mV, $V_{set} = 30$ mV.

showing a gradual reduction in the inelastic gap (Figure 2.9e). However, after a steep jump in the current, the initial features are fully recovered. This suggests that in this range of retraction we are starting to induce some modification in the dihedral angles but then a structural reorganization, indicated by the current jump, brings the system back to its initial conformation.

Nevertheless, a full transition in the spin state of the molecule is observed within a few retraction steps between $z = 350$ pm and $z = 430$ pm, as illustrated in Figure 2.10. The initial IET gap, associated to the antiferromagnetic alignment of the two unpaired electrons, with a coupling exchange $J = 2.7$ meV, progressively merges into a Kondo resonance, which can be interpreted as the fingerprint of a configuration of loosely interacting spins. This change is therefore attributed to a gradual reduction of the intramolecular exchange J, as a consequence of the increase in one or more torsional angles during the lifting process. Determining the structural modifications occurring while pulling the molecule is not straightforward, but we can assume that at this stage of the retraction (around 500 pm from the contact), at least the fluorenyl unit closer to the tip-molecule bond position is fully detached from the substrate, thus rotating its orientation with respect to the inner moieties.

While further retracting the tip, the conductance keeps decreasing exponentially, as expected for non-resonance transport through a molecular

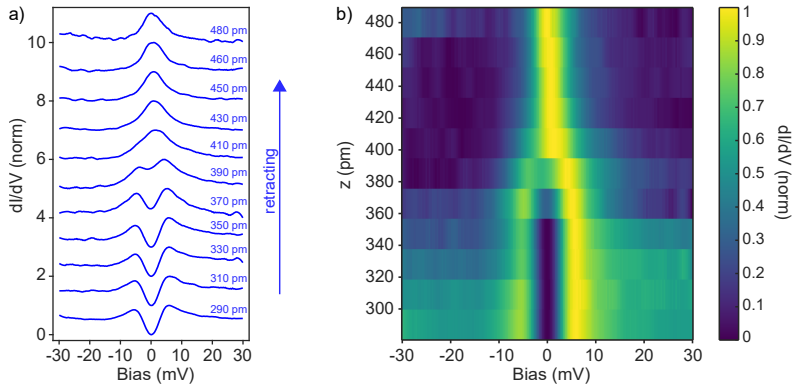

Figure 2.10: (a) Set of dI/dV spectra and (b) corresponding colorplot measured while continuing retracting the tip ($z = 290$ pm to $z = 480$ pm) after the initial lifting stages reported in Figure 2.9. The z limits of this set of spectra are indicated as dashed lines in the conductance curve in Figure 2.9c. Now a full and gradual transition from the spin excitation feature to a Kondo resonance is observed, suggesting a progressive reduction of the intramolecular exchange coupling. Spectroscopy parameters: $V_{mod} = 2$ mV, $V_{set} = 50$ mV.

junction[104]. Finally, at a tip height around $z = 520$ pm, the Kondo signal vanishes, as shown in Figure 2.11. Interestingly, the Kondo resonance is subsequently recovered in the dI/dV spectra after a further jump in the current (at $z = 560$ pm), which can be related to the detachment of a molecular moiety from the substrate or to another conformational change, due to the high structural flexibility of **SMe-2OS**.

After the lifting process, we started to gradually reduce the tip-sample distance, with the aim of bringing the molecule back to its initial on-surface configuration, while simultaneously measuring differential conductance spectra.

As illustrated in Figure 2.12, during this process, the Kondo resonance vanishes and IET features are recovered. However, now we observe higher exchange values compared to the lifting stage, with the gap progressively increasing up to 36 meV, and smaller conductance overshoot over the steps. The wider spin excitation gaps suggest that, while pushing the molecule towards the substrate, we are able to induce structural conformations with smaller dihedral angles compared to those stabilized by adsorption on the surface. However, at $z = 140$ pm. we detect an abrupt structural change, which results in a sudden reduction in the IET gap. Finally, when bringing the tip height to values close to the starting position of the lifting experiment, after another sharp change, the initial singlet-triplet excitation features are fully recovered, with an exchange $J = 4.7$ meV, closer to the value measured when **SMe-2OS**

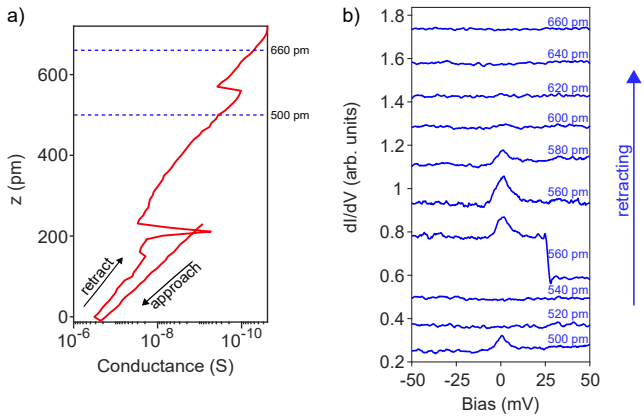

Figure 2.11: Two-terminal transport measurements performed while lifting **SMe-2OS**, at larger tip retraction heights with respect to Figure 2.10. (a) Conductance curve recorded during the whole lifting experiment, with the dashed lines highlighting the z range considered here (from $z = 500$ pm to $z = 660$ pm). (b) Stack of dI/dV spectra measured at different z (as indicated for each curve). At this stage the Kondo signal vanishes but is then recovered after a structural modification in the molecular junction, in correspondence to the steep jump in the current detected at $z = 560$ pm.

is lying on the substrate. This suggests that, after forcing more planar configurations with the STM tip, the system reorganizes into the more stable on-surface adsorption conformation with larger torsional angles. These results demonstrate the reversibility of the manipulation process and the robustness of the diradical state of the molecule, as well as the variety of structural phases that can be explored in this two-terminal experimental configuration.

Finally, we want to point out then the importance of the exact contact position in single-molecule transport measurements. As illustrated in Figure 2.13, we studied the effect of picking up **SMe-2OS** from a fluorenyl moiety, hence in a position closer to a radical site. Before approaching the STM tip, we measured the usual spin excitation features in STS (Figure 2.13b). Then, we followed the same procedure described before and contacted the molecule in the position marked by the cross in Figure 2.13a.

After the formation of a tip-molecule bond (tip height $z = 0$), a new broad and asymmetric feature appears in the dI/dV spectra at 0 bias, as shown in Figure 2.13d. While retracting the tip, the feature acquires a more symmetric shape, compatible with a Kondo resonance, although some instability is observed during the process (e.g., in correspondence to the jump in the current at $z = 50$ pm). The drastic change in the transport spectral features upon formation of the tip-molecule contact can be attributed to the suppression

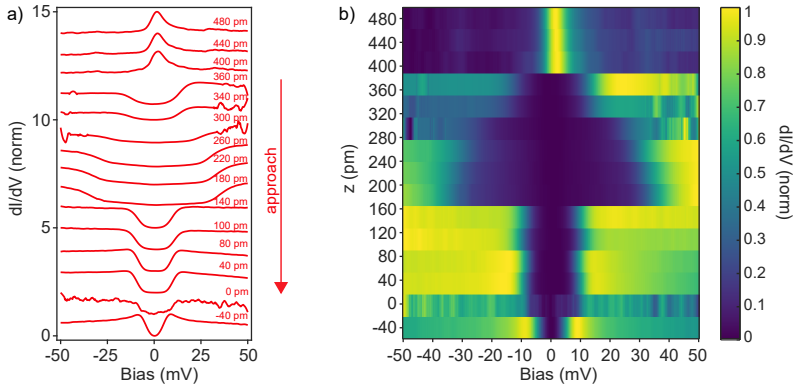

Figure 2.12: (a) Set of dI/dV spectra and (b) corresponding colorplot measured when bringing the molecule back towards the substrate, after the lifting process illustrated in Figures 2.9 and 2.10. During this process new structural modifications occur, determining the appearance of distinct spectral features. In the end, the original singlet-triplet excitation spectrum is recovered. Parameters: $V_{mod} = 2$ mV, $V_{set} = 50$ mV.

of the radical unit hosted by the fluorenyl moiety where the bond is formed. Consequently, the symmetric zero-bias peak recovered while further retracting the tip can be ascribed to a $S = 1/2$ Kondo resonance related to the remaining unpaired electron, as previously observed in similar manipulation experiments on graphene nanostructures[58].

As expected, the contact formed in this position is more fragile than in the sulfur-hosting end groups: as displayed in Figure 2.13c, after retracting the tip around 260 pm from the initial height, a steep decrease in conductance occurs, suggesting that the contact has been lost. We report in Figure 2.13e-f dI/dV spectra measured before and after the breaking of the tip-molecule bond. Interestingly, we observe that when the molecule "falls" back to the surface, the Kondo resonance disappears and the singlet-triplet excitation features are fully recovered in the STS spectra, which demonstrates the reversibility of the spin quenching effect induced by the tip.

In conclusion, the two-terminal transport measurements performed in partially suspended configurations provide a further confirmation of the tunability of the spin state of **SMe-2OS** and its relation to the molecular structural arrangement.

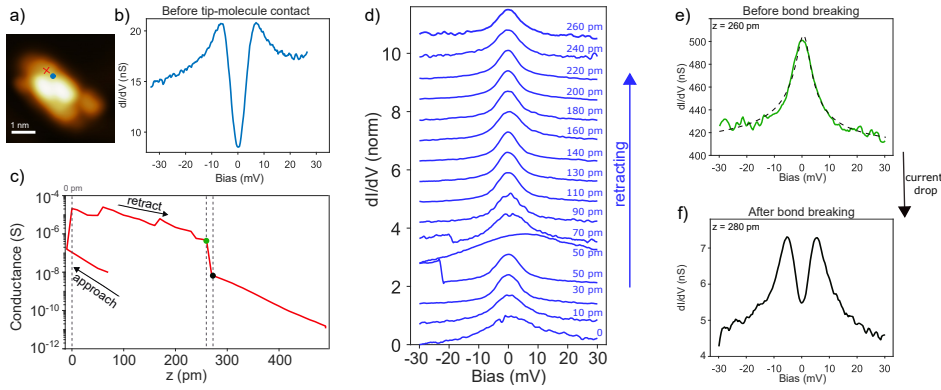

Figure 2.13: Picking up the molecule from a fluorenyl moiety. (a) STM constant-current image of the **SMe-2OS** molecule, indicating the site of the tip-molecule contact. (b) dI/dV spectrum measured on the molecule in (a), in the position marked by the circle, before contacting it with the tip ($V_{mod} = 2$ mV, $V_{set} = 30$ mV, $I_{set} = 500$ pA). (c) Conductance measured at different tip heights z, while approaching the tip towards the molecule and during the subsequent retraction steps (tip-sample bias $V = 30$ mV). The position at which the tip-molecule contact is formed is indicated as 0. (d) dI/dV spectra recorded at different z (as indicated for each curve) from the jump to contact ($z = 0$ pm) to $z = 260$ pm. (e) dI/dV spectrum measured at $z = 260$ pm, before the current drop highlighted in (c) by the dashed line. The spectrum displays a zero-bias peak that can be attributed to a Kondo resonance. The black dashed line is a fit with a Frota function, yielding a HWHM=6.50 meV. (f) dI/dV spectrum recorded after the current drop, now revealing recovered spin excitation features. The steep reduction in the conductance suggests that the tip-molecule contact has been lost at this position. Spectroscopy parameters: $V_{mod} = 2$ mV, $V_{set} = 30$ mV.

2.5.2 Comparison with mechanical manipulation in break-junction devices

The experimental configurations explored by contacting individual molecules with the STM tip allow for a direct comparison with single-molecule transport measurements performed in mechanically controlled break junctions (MCBJ), another common technique for investigating the electronic properties of single molecules[107,108].

In MCBJ experiments a metal wire, fixed on a flexible support, is progressively broken by applying mechanical strain with a rod controlled by a piezoelectric actuator, so that a small gap, of the order of a nanometer, is opened. When a molecular solution is drop-cast onto the device and the solvent is completely evaporated, one or a few molecules may remain trapped within the gap during the breaking process. In this way it is possible to contact a single molecule with two metal electrodes, and thus probe charge transport through an individual molecular junction. Additionally, in the MCBJ setup the elec-

trode spacing can be precisely tuned by bending the substrate, which also allows for manipulation of the molecule's conformation within the junction.

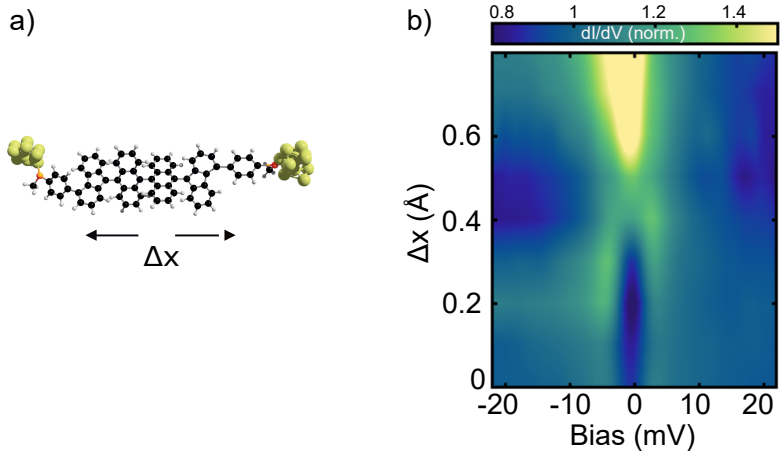

Figure 2.14: (a) Schematic representation of the manipulation of the **SMe-2OS** diradical in a mechanically controlled break junction (MCBJ). The two electrodes contacting the molecule are progressively separated, while I-V characteristics are simultaneously recorded. Then, dI/dV spectra are numerically computed to study the evolution of the spin state. (b) Colorplot of dI/dV spectra measured as a function of the electrode displacement Δx, showing a transition from a spin-flip signal to a Kondo resonance. The spectra are normalized to the average background between 10 mV and 20 mV. Figure adapted from [106].

We focus here on the spectroscopic features observed when introducing **SMe-2OS** diradicals in the MCBJ setup and on the variations detected while progressively separating the metal electrodes, as represented schematically in Figure 2.14a.

First, a solution of the diradical diluted in dichloromethane (DCM) was drop-cast onto the device. Importantly, we note that in the MCBJ experiment the diradical was deposited already in its open-shell form, with the solvent playing a role in preserving its radical state. Afterwards, the solvent was evaporated and the system was pumped to $P = 10^{-6}$ mbar and cooled down to liquid Helium temperature. The atomic-scale contact was then opened and the gap progressively increased in controlled steps (around 5 pm), while simultaneously recording $I - V$ characteristics as a function of the electrode displacement Δx. The differential conductance spectra were then calculated numerically[80].

Interestingly, similar spectroscopic features were obtained in the two experimental configurations (MCBJ and STM), despite the different procedures for the diradical deposition and the different contact geometries. As illus-

trated in Figure 2.14b, the MCBJ measurements performed at low electrode displacements reveal, in fact, bias-symmetric steps with significant conductance overshoots and lack of zero-bias resonances. These features, which can be attributed to an inelastic singlet to triplet excitation, are similar to those observed in the STM dI/dV spectra measured on **SMe-2OS** molecules adsorbed on the Au substrate (Figure 2.8c). Additionally, an exchange coupling $J \approx 3$ meV, close to the one measured in STM, can be inferred from the onset of the inelastic steps, suggesting analogous intramolecular arrangements in the two configurations.

A transition from this spin-flip signal to a zero-bias feature is detected after an electrode displacement $\Delta x = 0.5$ Å. This change appears remarkably similar to the transition from IETS to Kondo observed in the STM lifting experiment (as shown in Figure 2.10), that we had attributed to a progressive increase in the dihedral angles of the molecule while detaching it from the Au(111) surface. However, considering the different manipulation processes (displacement of the contact electrodes versus partial lifting of the molecule from a substrate), it is not straightforward to relate these similar spectral modifications to analogous changes of the molecular structural conformation. Due to the difficult determination of the exact molecule-electrode contact positions in the MCBJ setup, we cannot safely discard a process of spin quenching that reduces the number of unpaired electrons from N=2 to N=1.

Overall, these results demonstrate that both the MCBJ and STM techniques allow for controlled and fine-tuned single-molecule manipulation. While MCBJ is generally valued for the mechanical stability of the junctions, it also presents several limitations, mostly related to the lack of direct information on the shape and the composition of the molecular junctions, including the actual number of contacted molecules. As a result, statistical analysis of a large series of conductance curves is generally required for the determination of single-molecule properties[109–111]. In contrast, STM allows for the direct visualization and characterization of the molecules at the junction. The results from our mechanical manipulation experiments highlight the advantages of directly comparing MCBJ with STM: the similarity in spectral features observed in the MCBJ trace and in the two-terminal STM lifting experiment provides a direct confirmation of the single-molecule nature of the **SMe-2OS** junctions formed using the MCBJ technique.

2.6 Spin manipulation by chemical tuning

Finally, we studied how modifications of the chemical structure affect the intramolecular spin-spin interaction in the **2-OS** diradical. For this purpose, we

considered a derivative featuring a single anthracene moiety, and thus a shorter distance between the radical-hosting units, and investigated its properties on a Au(111) substrate.

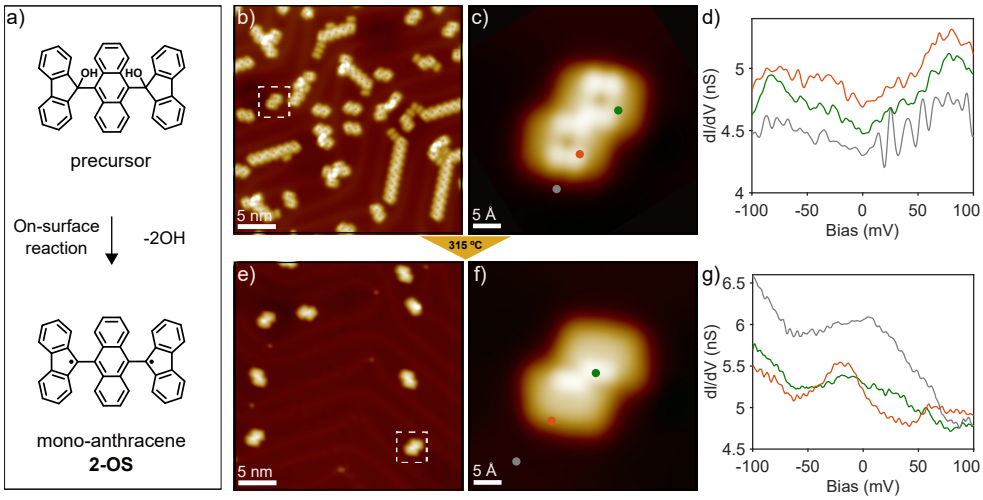

Figure 2.15: Generation of the mono-anthracene-**2-OS** diradical on Au(111). (a) Envisioned on-surface synthesis of the diradical from a closed-shell precursor featuring OH capping groups. (b) STM image recorded after deposition of the precursor onto Au(111), revealing mostly molecular chains and several isolated units, as the one highlighted in the dashed box. (c) Close-up image of the structure in (b). (d) Low-bias dI/dV spectra measured in the positions marked in (c), indicating a closed-shell structure. (e) STM image after annealing the sample at 315°C. A higher degree of planarization is observed now in the molecular structures, as highlighted in the close-up image in (f), suggesting that the OH groups may have been removed. (g) dI/dV spectra measured in the positions marked in (f), still displaying no fingerprint of magnetism. Topography parameters: $V = 1$ V; $I = 30$ pA. Spectroscopy parameters: $V_{mod} = 1$ mV; $V_{set} = 200$ mV; $I_{set} = 1$ nA.

As shown in the scheme in Figure 2.15a, we followed the same on-surface synthesis procedure envisioned for the original **2-OS** diradical, starting with a closed-shell precursor containing OH capping groups incorporated at the two radical sites.[5] After sublimation of the precursor onto the Au(111) surface through flash evaporation, we observed mostly self-assembled molecular chains as well as some fragments (likely corresponding to detached fluorenyl moieties) and many identical isolated structures, as illustrated in Figure 2.15b.

A close-up STM image of one of such structures is reported in Figure 2.15c. As in the case of the **2-OS** diradical, it is not straightforward to identify its components and attribute them to the different molecular moieties, due to

[5]In-solution synthesis of the precursor performed by Manuel Vilas-Varela and Diego Peña (CiQUS and Universidade de Santiago de Compostela, Santiago de Compostela, Spain).

the presence of non-planar features. We observe, however, that the system consists of two identical units, each with a lateral length of around 1 nm, which suggests that it may correspond to a dimer-like structure. Additionally, the observation of self-assembled chains containing both odd and even number of units (each unit being the square-like structure that forms half of the system in Figure 2.15c) supports the identification of these structures as dimers rather than individual molecules. As expected for a closed-shell precursor, the low-bias dI/dV spectra measured on different positions along the alleged dimers do not show any magnetic features, such as clear zero-bias resonances or bias-symmetric IETS steps.

We then annealed the sample at progressively higher temperatures in order to induce the C-OH cleavage reaction. We observed structural changes in the molecules after annealing at 315°C. As shown in Figures 2.15e-f, in addition to the disassembly of the chains and an overall desorption of material from the surface, the individual dimer-like structures now display a higher degree of planarity, a change that could be interpreted as an indication of the removal of the OH capping groups. However, the low-bias dI/dV spectra shown in Figure 2.15g still do not reveal any magnetic signatures.

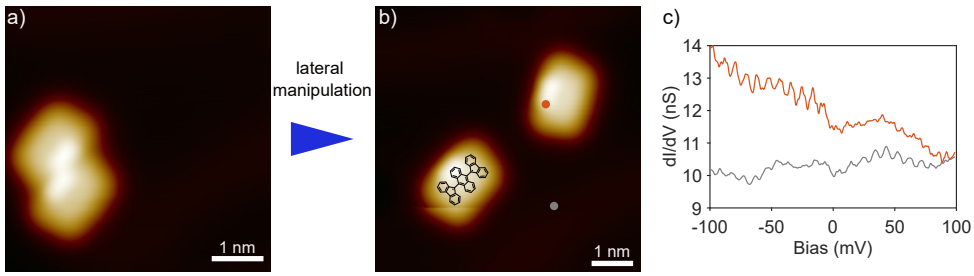

Figure 2.16: Lateral manipulation of the molecular structures formed after the annealing (Figure 2.15), revealing the presence of two self-assemble molecules. (a) STM image before manipulation; (b) image after separating the units composing the dimer (with the chemical structure superimposed on one unit); (c) dI/dV spectra measured on one monomer and on the bare Au, revealing the absence of magnetic features in the individual molecules. Topography parameters: $V = 1$ V; $I = 30$ pA. Spectroscopy parameters: $V_{mod} = 1$ mV; $V_{set} = 100$ mV; $I_{set} = 1$ nA.

To gain a better understanding of the nature of the molecular structures found after the annealing, we performed lateral manipulation using the STM tip, as illustrated in Figure 2.16. The structure reported in Figure 2.16a could easily be separated into two identical units (Figure 2.16b), confirming its identification as a dimer composed of two non-covalently bonded mono-anthracene-**2-OS** molecules. We observe that each molecule displays a bright

lateral feature in the centre, that can be reasonably attributed to the inner anthracene unit, exhibiting some rotation with respect to the substrate. This interpretation is supported by comparison with the **2-OS** diradical (see the STM image in Figure 2.1c), where, after the dissociation of the OH groups, the internal anthacene units appeared brighter with respect to the end fluorenyl moieties.

We then performed dI/dV spectroscopy on an isolated single molecule and still did not detect any fingerprint of magnetism, as reported in Figure 2.16c. Assuming that the structural changes observed after the annealing can be attributed to the removal of the OH groups, the lack of magnetic features in the spectra suggests that the molecule is in a closed-shell state even when its radical units are not quenched.

A possible explanation of this result is that the reduction in the spin-spin separation, which is expected to enhance the intramolecular exchange coupling[27,112,113], could lead to the formation of a closed-shell singlet state in the case of strong hybridization of the two radicals wavefunctions. This is also suggested by the TB-MFH calculations for the original **2-OS** diradical (reported in Figure 2.4c), which show that for high exchange couplings ($J \gtrsim$ 200 meV) the open-shell singlet transforms into a spin-unpolarized closed-shell singlet.

2.7 Conclusions

In summary, we have demonstrated that the **2-OS** diradical, a derivative of the Chichibabin's hydrocarbon, retains its open-shell character on Au(111) with a singlet ground state. Through the cleavage of protecting groups of the deposited diol precursors followed by spatially resolved scanning tunneling spectroscopy measurements, we resolved a singlet ground state with an exchange coupling $J \sim$ 7.3 meV. The robust singlet ground state measured at low temperature contrasts with the triplet ground state previously reported at room temperature[79]. We attributed this difference to the effect of thermally excited vibrational deformations at room temperature.

Theoretical TB-MFH simulations found that the substrate-induced partial planarization of **2-OS** favors the antiparallel coupling of the unpaired π electrons, while increasing the torsional angle between the molecular moieties progressively reduces the spin exchange coupling. Thus, we demonstrated the possibility of tailoring the magnetic interactions in a **2-OS** analogue functionalized with anchoring end groups, which fix the molecule to the metal substrate while inducing structural modifications by approaching the STM tip. We observed that the spin-spin interaction decreases when the molecule is partially

lifted from the substrate (thus acquiring a more orthogonal conformation), and that the initial singlet state can be recovered when bringing it back to a more planar arrangement.

Similar changes in the spin coupling were detected in two-terminal transport measurements when directly contacting the molecule with the STM tip in the position of the anchoring groups in order to lift it from the substrate in a controlled way. Interestingly, this configuration also allowed to reproduce the spectra obtained in mechanical manipulation experiments performed in a MCBJ setup.

In addition, we studied a shorter **2-OS** analogue, with a reduced distance between the radical-hosting units, caused by the removal of one anthracene moiety, and showed that this chemical modification transforms the original open-shell ground state into a closed-shell singlet.

Overall our results demonstrate the high tunability of the magnetic ground state of derivatives of the Chichibabin's hydrocarbon and, in particular, their high sensitivity to mechanical interactions, suggesting their strong potential as new all-organic spin-cross over materials.

2.8 Appendix

2.8.1 MF-Hubbard modeling based on Slater-Koster parametrization

In order to explore the role of the torsion angles of **2-OS** we implemented an effective non-orthogonal tight-binding description based on a Slater-Koster parametrization[114]. Our model considers a single p orbital per carbon site perpendicular to the anthracene (or fluorenyl) plane to which the atom belongs.

Using a custom implementation based on SISL[91], some characteristic hopping matrix elements t_{ij} between fluorenyl and anthracene sites are shown in Figure 2.17.

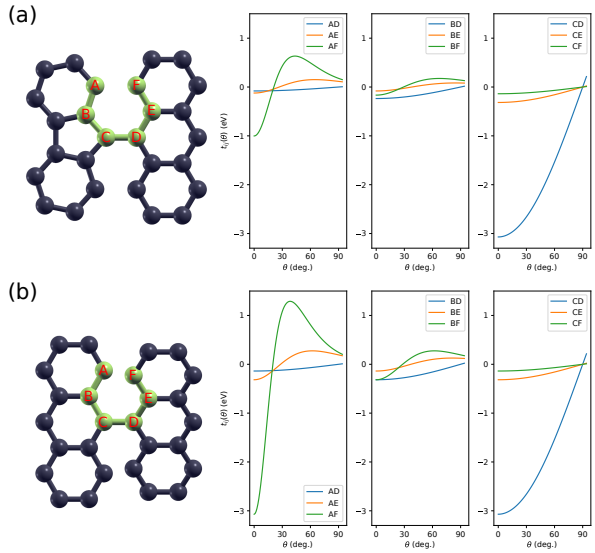

Figure 2.17: Selective Slater-Koster hopping matrix elements t_{ij} between characteristic sites as a function of the torsional angle θ around the C–D bond connecting (a) fluorene and anthracene or (b) two anthracene units.

In addition to this effective one-orbital-per-site SK model, we consider in the main text (Figure 2.4) also a local onsite Coulomb repulsion U in the mean-field approximation (MF-Hubbard). We solve iteratively for the symmetry-broken solutions corresponding to $S_z = 0$ (AFM or unpolarized) and $S_z = 1$ (FM) using HUBBARD[90].

2.8.2 DFT study of 2-OS adsorption geometry on Au(111)

In our study, Density Functional Theory (DFT) calculations were executed using SIESTA[115] to understand the interactions between **2-OS** and the metallic surface. The adsorption geometry is shown in Fig. 2.18. In this adsorption configuration we could not stabilize the antiferromagnetic spin state of the gas-phase molecule, but it was recovered by increasing the molecule-surface distance by 0.5 Å or more. The image shown in the inset of Figure 2.1c (main text) was obtained from the calculated charge density using the WSxM software[72].

To explore the impact of attractive forces from the STM tip on the adsorption geometry of **2-OS** on Au(111), we also performed additional 6 geometry optimizations in the presence of a model tip constrained at different positions near the center of the molecule as shown in Fig. 2.19. The variation in the dihedral angles are summarized in Tab. 2.1. We found that the three key dihedral angles in all cases increased due to attractive interactions with the tip. This corroborates the interpretation of a reduced exchange coupling J induced by attractive forces to the STM tip according to the model of Figure 2.4 in the main text. Such a change is consistent with the experimentally observed effects reported in Figure 2.8 in the main text for **SMe-2OS**.

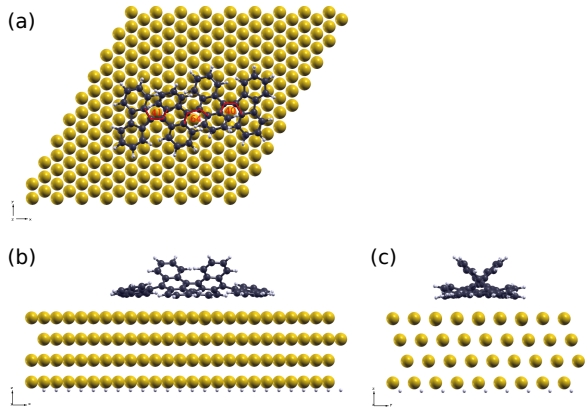

Figure 2.18: Adsorption geometry of **2-OS** on Au(111) obtained with SIESTA. The three torsional angles indicated in panel (a) corresponds to $\theta^{\text{surf}}_{\text{outer}} = 40\text{-}41^\circ$ and $\theta^{\text{surf}}_{\text{inner}} = 64^\circ$. As reference, the corresponding angles in the gas phase were found to be $\theta^{\text{free}}_{\text{outer}} = 54^\circ$ and $\theta^{\text{free}}_{\text{inner}} = 71^\circ$.

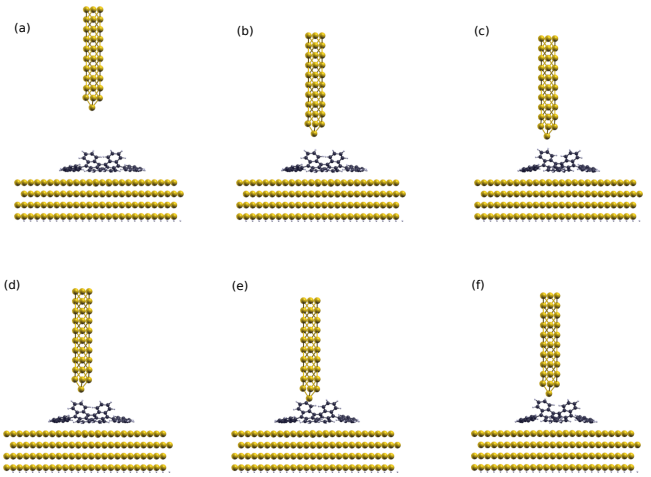

Figure 2.19: Adsorption geometries of **2-OS** on Au(111) in the presence of a model STM tip at different positions obtained with SIESTA, (a) with the tip far from **2-OS**, (b-f) with the tip progressively closer to the molecule.

Configuration	x (Å)	y (Å)	z (Å)	$\theta_{\text{outer},1}$	θ_{inner}	$\theta_{\text{outer},2}$
Fig. 2.19(a)	16.5	11.4	16.6	40.8 (0.0)	64.4 (0.0)	40.2 (0.0)
Fig. 2.19(b)	16.5	11.4	10.9	42.1 (1.3)	65.1 (0.8)	40.2 (0.0)
Fig. 2.19(c)	15.4	11.4	10.3	43.5 (2.7)	66.9 (2.6)	41.9 (1.6)
Fig. 2.19(d)	16.5	11.4	9.9	43.3 (2.5)	66.1 (1.7)	40.3 (0.0)
Fig. 2.19(e)	16.5	9.4	7.9	41.6 (0.8)	68.3 (4.0)	43.2 (3.0)
Fig. 2.19(f)	16.5	11.4	8.9	46.2 (5.4)	71.4 (7.0)	42.9 (2.7)

Table 2.1: Summary of molecular conformation for different STM tip apex atom positions (x, y, z) relative to the Au(111) surface, indicating the three dihedral angles θ_i and, in parentheses, the changes relative to those without the tip.

2.8.3 Thermochemistry effects on DFT calculations

In this section we will address the effects of considering thermochemistry (vibrations, rotational motion, etc.) to DFT calculations on **2-OS**. As it is discussed in the main text, according to MF-Hubbard calculations the open-shell $S = 0$ solution is lower in energy that the triplet. A variation of the angles $\theta_{o,i}$ affects the ΔE_{TS} energy separation, but it does not change the spin quantum number of the ground state. The effect of $\theta_{o,i}$ on the hoppings is calculated with a Slater-Koster parametrization in the case of MF-Hubbard, obtaining that ΔE_{TS} decreases when the angles are increased. The antiferromagnetic character of the kinetic exchange driven by hopping makes the $S = 0$ solution more stable, becoming degenerate with a $S = 1$ solution when two anthracene units, or an anthracene and an external fluorenyl unit, are perpendicular.

In Gaussian (g16)[116] it is possible to include the effects of temperature by the "`freq`" flag[117]. This flag entails the computation of different contributions to the entropy (S_{tot}) and internal thermal energy (E_{tot}). Specifically, this program considers the contributions from translation, electronic motion, rotational motion and vibrational motion. Then, it considers a thermal correction to the enthalpy and free energy, respectively, as:

$$H_{corr} = E_{tot} + k_B T, \tag{2.1}$$

and

$$G_{corr} = H_{corr} - T S_{tot}, \tag{2.2}$$

where $S_{tot} = S_t + S_r + S_v + S_e$ and $E_{tot} = E_t + E_r + E_v + E_e$ consider the different contributions that have been mentioned, where t, r, v and e refer, respectively, to the contributions from translation, rotational motion, vibrational motion and electronic motion.

By comparing the sum of electronic and thermal free energies for the $S = 1$ and open-shell $S = 0$ solutions ($G_{S,T}$) for different values of the temperature with a relaxed gas phase geometry ($\theta_i \approx 90°$), we can conclude that the thermochemistry effects are responsible of the $S = 1$ ground state in gas phase (see Figure 2.20), since for low T the $S = 0$ is the ground state but very soon the $S = 1$ becomes more stable when the temperature is increased. Then, if the geometry is planarized, the $S = 0$ solution is stabilized in account of an enhancement of the kinetic antiferromagnetic exchange, in accordance with MF-Hubbard.

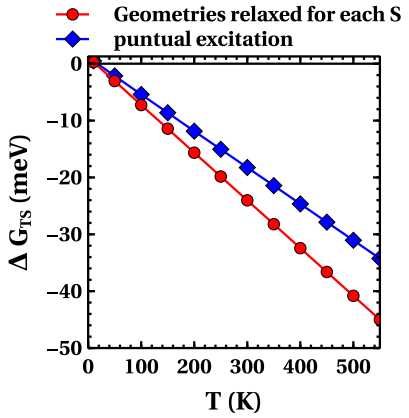

Figure 2.20: Variation of $G_T - G_S = \Delta G_{TS}$ with the temperature (T), calculated with DFT. It was used the PBE exchange-correlation density functional[118] and the STO-3G basis[119,120] with the Gaussian package[116] and the thermochemistry flag. For the red circles the geometry was relaxed for both spin solutions, and for the blue squares it was used the $S = 1$ relaxed geometry for all the calculations. The geometries were relaxed without the "`freq`" flag.

	PBE/STO-3G (5K)	PBE/STO-3G (100K)	BLYP/6-31G (5K)	BLYP/6-31G (100K)
ΔG_{TS} (meV)	0.7	-7	-0.2	-9

Table 2.2: Difference in energy between the open-shell $S = 0$ and $S = 1$ solutions for different density functional/basis and temperatures. The geometries were relaxed for every S in gas phase and without thermochemistry.

3 Spin interactions in a ferromagnetic molecular trimer

Triangulenes are prototypical examples of open-shell nanographenes. Their magnetic properties, arising from the presence of unpaired π electrons, can be extensively tuned by modifying their size and shape or by introducing heteroatoms. Different triangulene derivatives have been designed and synthesized in recent years, thanks to the development of on-surface synthesis strategies. Triangulene-based nanostructures with polyradical character, hosting several interacting spin units, can be challenging to fabricate but are particularly interesting for potential applications in carbon-based spintronics. In this chapter, we combine pristine and N-doped triangulenes into a more complex nanographene, **TTAT**, predicted to possess three unpaired π electrons delocalized along the zigzag periphery. We generate the molecule on a Au(111) surface and detect direct fingerprints of multi-radical coupling and high-spin state using scanning tunneling microscopy and spectroscopy. With the support of theoretical calculations, we show that its three radical units are localized at distinct parts of the molecule and couple via symmetric ferromagnetic interactions, which result in a $S = 3/2$ ground state, thus demonstrating the realization of a molecular ferromagnetic Heisenberg-like spin trimer.

An article based on the results reported in this Chapter has been submitted to *Journal of the American Chemical Society*.

- On-surface Synthesis of a Ferromagnetic Molecular Spin Trimer

  Alessio Vegliante, Manuel Vilas-Varela, Ricardo Ortiz, Francisco Romero-Lara, Manish Kumar, Lucía Gómez-Rodrigo, Fabian Schulz, Diego Soler, Hassan Ahmoum, Emilio Artacho, Thomas Frederiksen, Pavel Jelínek, Jose Ignacio Pascual and Diego Peña.

  Submitted to *Journal of the American Chemical Society*.

3.1 Introduction

Graphene flakes with triangular shapes represent a paradigmatic platform for studying interacting quantum spins. As shown in Chapter 1, the net spin of triangulene molecules depends on the flake's size and can be modified by heteroatom substitution[22,36–40,42,64]. The high-spin states of triangulenes are exceptionally robust because their singly-occupied orbitals (or zero-energy states) live in the same carbon sublattice, thus having a large spatial wavefunction overlap. Consequently, Hund's exchange coupling and the spin excitation energies generally amount to a significant fraction of an electronvolt. While systems with considerable energy gaps between the ground and excited spin states can be attractive for some applications related to classical magnetism, this can be a drawback for applications using the full spin spectrum of the nanographene.

Nanographenes with weakly interacting spins have been successfully synthesized on surfaces by covalently-bonding triangulene building blocks through their vertices[27,42,112,121–123]. This strategy maintains the triangulene integrity because the zero-energy modes have a low density of states over these connecting sites, and results in antiferromagnetic interactions between the monomer units, as we will see in the next chapter. An alternative strategy, explored more rarely, is connecting the nanographenes through their zigzag edges. While this method modifies the electronic and magnetic configuration of the original structure[124], it allows to build customized flakes hosting interacting localized radicals[88].

Here, we implement this strategy to synthesize a large, triangular nanographene hosting three ferromagnetically interacting radical units. By fusing three [3]triangulenes (3T) onto the edges of an aza[3]triangulene (A3T) core, we form **TTAT** (tris-triangulene-aza-triangulene, Figure 3.1), a high-spin triradical nanographene behaving as a symmetric Heisenberg spin trimer.

Each 3T unit hosts two unpaired π electrons localized along majority zigzag sites[22,40]. As shown in Figure 3.1a, this connection strategy pairs majority sublattice sites in opposite orientations, thus reducing the number of zero-energy states (i.e., their nullity) from eight to four and resulting in four unpaired π electrons for the pristine carbon structure.

Within the A3T core, nitrogen substitution at a majority site introduces an additional electron to the π system, stabilizing a D_{3h} symmetric configuration with three unpaired electrons at the zigzag corners.

Structurally, TTAT resembles an aza[8]triangulene with six fewer six-membered rings, two per triangular side. This change creates three distinct gulf

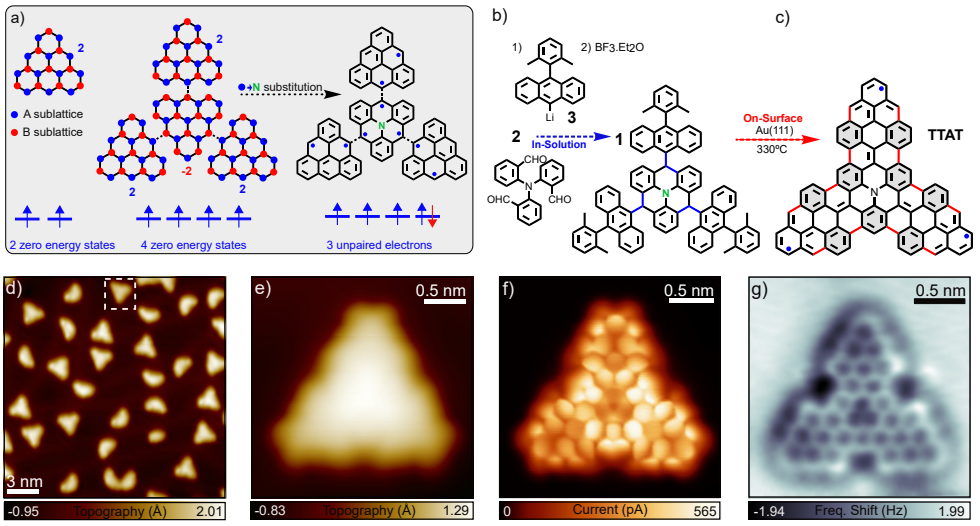

Figure 3.1: (a) Schematic representation of the formation of **TTAT** (c), obtained by coupling three [3]triangulene building blocks through an aza[3]triangulene core. (b-c) In-solution and on-surface reaction steps leading to the synthesis of **TTAT**, with the C-C bonds formed during each step indicated in blue and red, respectively. (d) STM constant-current image ($V = 0.9$ V, $I = 30$ pA) after deposition of the precursor on Au(111) and subsequent annealing at 330 °C. The white dotted square highlights an intact and planar molecule, corresponding to target product. (e) STM constant-current image of **TTAT** measured with a CO-functionalized tip ($V = 200$ mV, I= 30 pA). (f) Constant-height bond-resolved STM current scan ($V = 5$ mV) and (g) constant-height bond-resolved AFM image (oscillation amplitude $A = 60$ pm), both performed with CO-functionalized tips.

regions along the edges, each formed by two conjoined bay areas that accommodate nine Clar sextets (see Figure 3.1c).

In the following, we report the on-surface generation of **TTAT** on a Au(111) surface and demonstrate that it behaves as a ferromagnetic Heisenberg spin trimer. Combining low-temperature STM measurements with theoretical simulations, we resolve its structural integrity on the surface and demonstrate that it lies in a neutral charge state, maintaining a $S = 3/2$ ground state. The resolution of low-energy spectroscopic fingerprints and their simulation through multiconfigurational simulations reveal the presence of a triradical character with ferromagnetic interaction among the unpaired electrons. This nanographene represents, therefore, a unique system for investigating entanglement in a single-molecular architecture.

3.2 On-surface synthesis of TTAT

We envisioned the synthesis of **TTAT** through a combination of in-solution and on-surface synthesis, as represented in Figure 3.1b. First, we addressed the preparation of the TTAT precursor **1** following the synthesis strategy of an aza-[5]-triangulene precursor[64], shown schematically in the figure.[1]

We deposited the **TTAT** precursor **1** onto a Au(111) surface at room temperature via flash annealing of a silicon wafer loaded with molecular grains. Subsequently, the sample was annealed at 330°C to activate the dehydrogenation reactions necessary to induce the formation of the twelve C-C bonds marked in red in Figure 3.1c and achieve full molecular planarization. The overview STM constant-current image recorded after annealing (Figure 3.1d) shows intact triangular-shaped products alongside smaller molecular fragments. A closer inspection reveals that many triangular products retain one or more methyl groups, which appear as protruding rounded lobes in the STM images. Nevertheless, we identified the target product, **TTAT**, in a small fraction (around 5%) of the non-fragmented molecules. The molecular structure appears fully planarized in this case and displays chamfered corners (Figure 3.1e). To conclusively demonstrate the successful on-surface generation of **TTAT**, we performed bond-resolved (BR) constant-height STM and non-contact AFM imaging using a CO-terminated tip[52] (Figures 3.1f-g). The BR images resolve the molecular backbone, revealing the absence of structural defects and the preserved three-fold symmetry of **TTAT** upon adsorption on the surface. Additionally, the bond-resolved STM image, recorded at $V = 5$ mV, displays an apparent increase in the current signal along the zigzag edges near the triangulene corners and in the gulf regions around the center, providing a first indication of an enhanced density of states around the Fermi level, likely due to the presence of radical states[58].

3.3 Open-shell state of TTAT on Au(111)

To address the electronic and magnetic properties of **TTAT** on Au(111), we performed differential conductance (dI/dV) spectroscopy (Figure 3.2a). First, we explored the low-energy spectral window, where spin fingerprints appear in the density of states. Spectra measured on the corners of the outer triangulenes show low-bias features indicative of an open-shell character: a weak zero-bias peak, characteristic of a Kondo resonance, and bias-

[1] In-solution synthesis of the molecular precursor performed by Manuel Vilas-Varela, Lucía Gómez-Rodrigo and Diego Peña (CiQUS and Universidade de Santiago de Compostela, Santiago de Compostela, Spain).

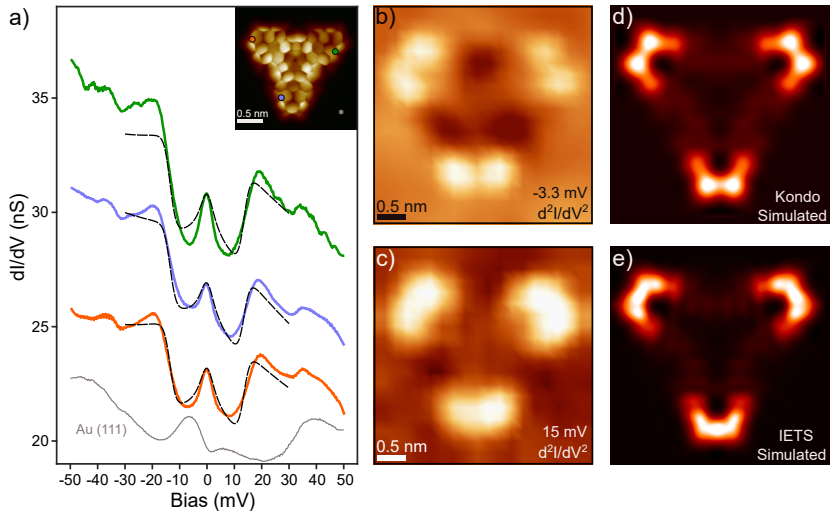

Figure 3.2: (a) Low-energy dI/dV spectra measured with a CO-functionalized tip along the zigzag edges of **TTAT** at the positions indicated in the bond-resolved CO image in the inset. The spectra display similar features: a Kondo resonance and spin excitation features centered at $V \approx \pm 15$ mV. The black dashed lines represent fits to the data using the perturbative model by Ternes[85], for the case of three S=1/2 spins coupled with a ferromagnetic exchange $J = 9$ meV. The higher energy steps at ± 35 mV (also visible on the bare Au(111) surface) are observed when recording spectra with a CO-functionalized tip, and are generally attributed to the excitation of a frustrated rotational mode of the CO molecule[125]. Spectroscopy parameters: $V = 50$ mV, $I = 1$ nA, $V_{mod} = 2$ mV. (b-c) d^2I/dV^2 maps at distinct bias ($V = -3.27$ mV and $V = 15$ mV, respectively), obtained by numerical differentiation from a grid of dI/dV spectra. The maps allow to probe the spatial distribution of the Kondo resonance (b) and the spin inelastic excitation (c). (d) Simulated Kondo and (e) spin excitation dI/dV maps, computed from the Kondo orbitals (d) and Natural Transition Orbitals (NTOs), respectively (Kondo orbitals and NTOs reported in the Appendix Figures 3.12 and 3.11, respectively).

symmetric step-like features at $V \approx \pm 15$ mV, which are related to inelastic spin excitation processes[86,88,122,123,126]. To probe the spatial distribution of both Kondo and inelastic electron tunneling spectroscopy (IETS) features, we mapped the derivative of the differential conductance (i.e., d^2I/dV^2 maps) at $V = -3.27$ mV and $V = 15$ mV, respectively. At these bias values, Kondo and IETS features appear as peaks in d^2I/dV^2 spectra, with amplitude proportional to the weight of the Kondo and inelastic channels (see Appendix Figure 3.8). As shown in Figures 3.2b and 3.2c, in both maps the d^2I/dV^2 signal appears localized on the corners of the three outer triangulenes, indicating that the radical character of the molecule stems primarily from orbitals distributed over the edge of the external moieties, as we will discuss later.

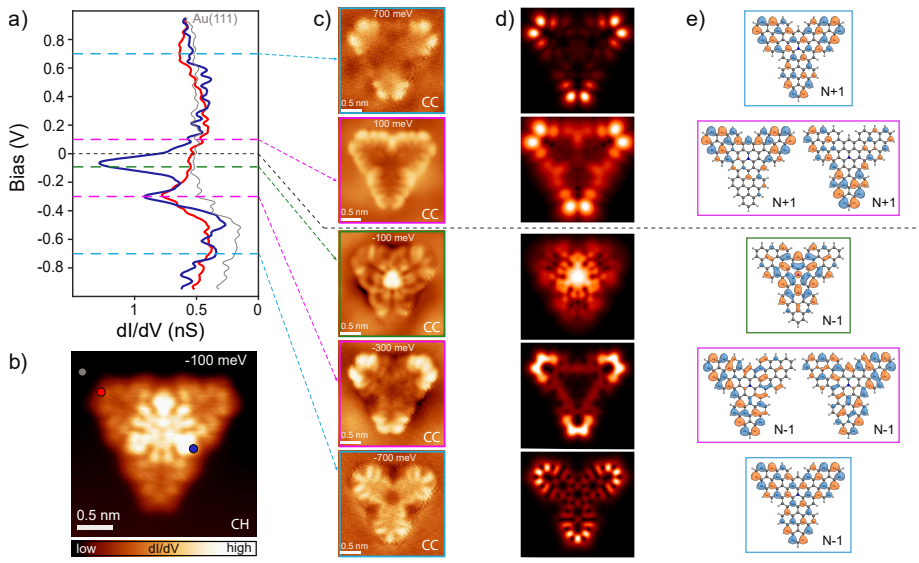

Figure 3.3: (a) dI/dV spectra measured at the points indicated in (b), revealing molecular orbital resonances ($V = 1$ V, $I = 500$ pA, $V_{\mathrm{mod}} = 10$ mV). (b) Constant-height (CH) dI/dV map recorded at $V = -100$ mV with a CO-functionalized tip, corresponding to an orbital with non-vanishing signal over the inner N-doped triangulene (open feedback parameters: $V = -100$ mV, $I = 300$ pA, $V_{\mathrm{mod}} = 10$ mV) . (c) Constant-current (CC) dI/dV maps recorded at different bias values around 0, with a CO-terminated tip ($I = 300$ pA, $V_{\mathrm{mod}} = 10$ mV). (d) Simulated dI/dV maps, obtained using Dyson orbitals, corresponding to the processes of adding and removing electrons. (e) Dyson orbitals isosurfaces.

Resolution of the **TTAT** frontier orbitals and their distribution over the molecular architecture provides a glimpse of the molecular spin ground state. We measured dI/dV spectra on a broader bias range (1V, -1V) on distinct molecular positions (Figure 3.3a) and found several peaked resonances attributed to molecular states. The dominant one is a resonance centered at around -100 mV, with spatial distribution over the central aza moiety, as probed by the constant-height dI/dV map reported in Figure 3.3b. The tail of this resonance crosses through zero bias and causes the tilted background in the low-energy spectra of Figure 3.2a. It also accounts for the increased current around the center observed in bond-resolved constant-height images like in Figure 3.1f.

As shown in Figure 3.3c, a non-vanishing signal over the central aza moiety is only found in the dI/dV map measured at -100 meV, with no replica at positive bias. This points towards a doubly-occupied state over the center of the flake, in agreement with results from DFT calculations reported in the Appendix (Figure 3.9) for a free molecule. According to DFT, the zero-energy

orbital A_1 (with the largest amplitude over the N site and C_{3v} symmetry) hosts the extra electron provided by the N heteroatom substitution in the neutral charge state. The molecule spin is primarily hosted in the three remaining singly-occupied orbitals (SOMOs), two of which are degenerated, with E symmetry, and the third one is the C_{3v} symmetric A_2 orbital[127]. These orbitals are distributed mainly along the molecular edges, with a weak contribution from the inner aza group.

Their singly occupied character can be concluded from dI/dV maps throughout a wider energy region: characteristic dI/dV patterns attributed to the SOMOs and their correlated singly unoccupied orbitals (SUMOs) appeared at −700 meV and −300 meV, and at 100 meV and 700 meV, respectively. Since all states detected around E_F lie close in energy, the molecular system is expected to exhibit a strong multiconfigurational character. Therefore, to identify and interpret the dI/dV maps, we computed the relevant Dyson orbitals[128] using the natural orbitals obtained from Complete Active Space Configuration Interaction (CASCI) calculations (see Appendix Figure 3.10). [2] In agreement with DFT, we obtained three Dyson orbitals accounting for electron addition and four for electron removal (Figure 3.3e), as expected for a ground state composed of three singly occupied and one doubly occupied state. In Figure 3.3d, we show the simulated dI/dV maps resulting from the computed Dyson orbitals, including a CO-functionalized tip, calculated with the PP-STM code[129]. The simulations reproduce the experimental dI/dV maps in great detail, further confirming the identification of three singly occupied states hosting the spin properties of the molecule.

The simulations indicate that **TTAT** maintains a neutral charge state on the electrophilic Au(111) surface. Kelvin probe force microscopy (KPFM) measurements confirm that the molecule remains in a neutral state on Au(111)[130]. As reported in Figure 3.4, we measured the local contact potential difference (LCPD) between tip and sample on the molecule and on the bare Au(111) at different tip heights. The LCPD measured on the molecule is always more negative than on the substrate. However, the very little variation of the LCPD when approaching the tip towards the molecule (around 22 mV across a range of 1 nm), as well as the small difference between the values recorded on the molecule and on the bare surface, suggest that **TTAT** is in a neutral charge state on Au(111)[131].

This behavior contrasts with the cationic state found for the structurally similar molecule aza[5]triangulene (A5T), despite both molecules having the same spin imbalance and nullity[39,64,132]. Although the precise factors driving

[2] Calculations performed by Manish Kumar, Diego Soler, and Pavel Jelínek (Institute of Physics, Czech Academy of Sciences, Prague, Czech Republic).

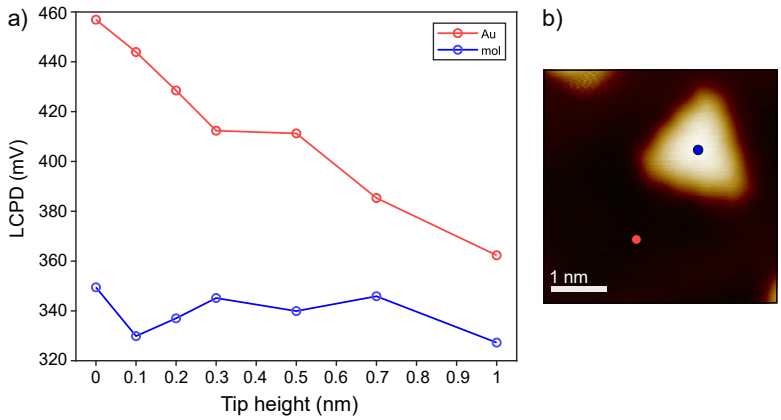

Figure 3.4: Kelvin probe force microscopy (KPFM) measurements on **TTAT**. (a) Local contact potential difference (LCPD) values measured at different tip-molecule distances on the molecule and on the bare Au(111) surface, as indicated in the constant-current STM image in (b). The 0 distance corresponds to the setpoint ($I = 30$ pA; $V = 200$ mV) over the centre of the molecule. For each tip height, we first measure a $\Delta f(V)$ spectrum (frequency shift as a function of the tip-sample bias) in the range (-0.1V, 0.9V) on the molecule, then we move the tip to the bare Au (with the feedback loop open) and record the same spectrum at the same height, and determine the LCPD for each position from the vertex of the KPFM parabola[130].

charge transfer differences near chemical equilibrium would require further study, we speculate that the neutral stability of **TTAT** (compared to **TTAT**$^+$) is related to its enhanced aromaticity, evidenced, for example, by the larger number of Clar sextets. In contrast, the antiaromaticity of neutral A5T species accounts for its tendency to oxidize on Au(111)[64].

These observations suggest that **TTAT** has a spin ground state $S = 3/2$ on Au(111), with parallel spin alignment due to Hund's exchange interactions among the three SOMOs[41,133]. We thus attribute the zero-bias resonance in the STS spectra to an underscreened Kondo effect associated with this high-spin state. Nanographenes with spin above $S = 1/2$ generally exhibit partial Kondo screening on surfaces, leading to smaller zero-bias resonances[40,57], as seen in Figure 3.2a. Additional evidence for this underscreened Kondo effect is the resonance splitting under an external magnetic field ($B = 2.7$ T) shown in Figure 3.5. An underscreened Kondo resonance, in fact, is expected to undergo a splitting as soon as the Zeeman energy ($g\mu_B B$) becomes greater than the thermal broadening ($k_B T$), which in our experiment ($T = 1.2$ K) corresponds to a field $B \approx 1$T[58]. A fully screened $S = 1/2$ Kondo resonance, on the other hand, would not display any splitting at this relatively low field, as shown in previous works[57,64].

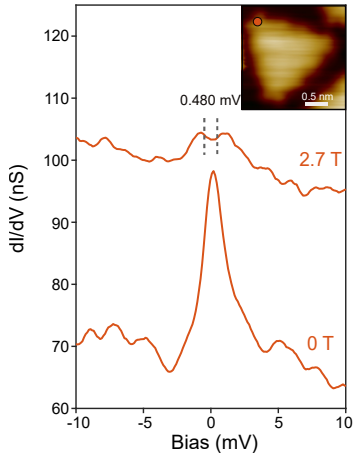

Figure 3.5: Comparison of low-bias dI/dV spectra measured in the position indicated in the inset, in the absence of external magnetic field, and at 2.7 T field. The Kondo resonance displays a splitting of 0.480 mV when applying the magnetic field. This can be interpreted as an indication of an underscreend Kondo effect. Parameters: $V = 10$ mV, $I = 1$ nA, $V_{mod} = 0.5$ mV. These measurements were performed at $T = 1.2$ K.

3.4 Triradical character of TTAT and Heisenberg spin trimer model

To rationalize the high-spin triradical ground state of **TTAT**, and the origin of the IETS features observed in dI/dV spectra, we performed multiconfigurational calculations with the complete active space self-consistent (CASSCF) method.[3] Considering a CAS(7,10), we obtain that three natural orbitals (highlighted in the dashed box, Figure 3.6a) have an electron occupation close to 1 in the ground state, thus indicating the presence of three unpaired electrons. In accordance with the DFT calculations and the experimental results, a natural orbital with A_1 symmetry and centered on the N heteroatom appears with a larger electron occupation.

As shown in the many-body energy levels in Figure 3.6b, the CASSCF calculations confirm the quartet ($S = 3/2$) ground state of **TTAT**, which accordingly is predominantly described by a single determinant[134], as depicted in Figure 3.6c.

The first two excited states are two nearly degenerate spin $S = 1/2$ levels found at 19 meV and 22 meV above the ground state. These values lie close to the experimental excitation gap obtained from the IETS steps ($\Delta \sim$

[3]Calculations performed by Ricardo Ortiz, Thomas Frederiksen (Donostia International Physics Center, San Sebastián, Spain).

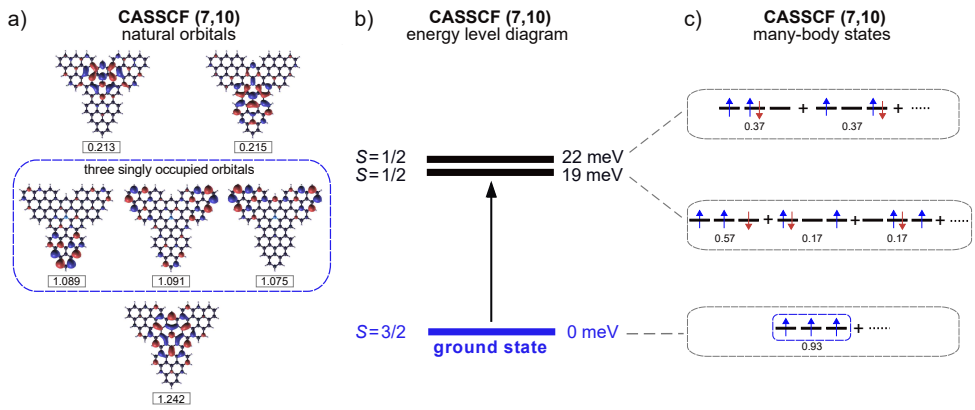

Figure 3.6: (a) Natural orbitals computed by CASSCF(7,10). The numbers at the bottom of each orbital indicate the electron occupation. We find three orbitals with occupation close to 1, spatially distributed over the triangulene edges. (b) Diagram representing the energy and the total spin of the many-body ground state and first two excited states of **TTAT**, as computed by CASSCF(7,10). (c) Schematic representation of the most relevant Slater determinant for each of the many-body states in (b), displaying the electronic occupation of the three natural orbitals highlighted in the dashed box in (a). The number below each Slater determinant refers to its weight in the corresponding many-body state.

15 meV), supporting the identification of the inelastic spectral features with a spin excitation process from $S = 3/2$ to $S = 1/2$. These doublets are described by a linear combination of different Slater determinants with similar weight (Figure 3.6c), justifying the multiconfigurational methods used in Figure 3.3.

The multiconfigurational nature of the doublet excited states is likely reflected in the experimental magnetic fingerprints shown in Figures 3.2b-3.2c. To explain the spatial localization of the Kondo signal, we used the concept of Kondo orbitals recently introduced in [132] to describe the Kondo effect in open-shell polyradical molecular systems. In this framework, the Kondo orbitals are associated with scattering processes between molecular electrons and conduction electrons of the underlying metal featuring antiferromagnetic exchange coupling. Using CASCI calculations, we obtained the set of Kondo orbitals shown in Appendix Figure 3.12, which were then used for calculating the corresponding Kondo dI/dV map using the PP-STM code[129]. The simulated dI/dV map shown in Figure 3.2d reproduces the shape and distribution of the experimental Kondo map, further confirming the interpretation of the Kondo signal as the fingerprint of a $S = 3/2$ spin state.

Similarly, the inelastic spin excitation from the quadruplet ground state to the two doublet excited states is represented by CASCI Natural Transition Orbitals (NTOs) shown in the Appendix Figure 3.11. The simulated spin

excitation dI/dV map[129] reported in Figure 3.2e was obtained by summing the contributions of the NTOs corresponding to the spin excitation to the two degenerate excited states. The excellent agreement with the experimental map of the IETS signal supports the origin of the inelastic signal as a quartet-doublet spin excitation.

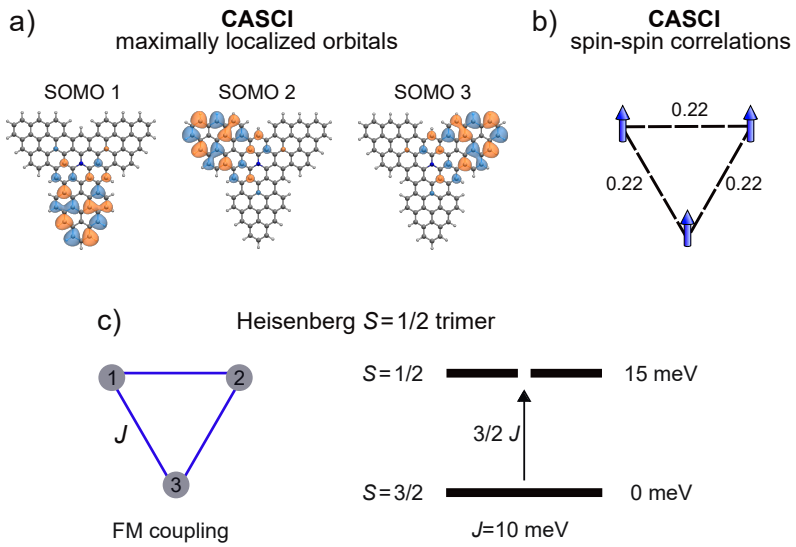

Figure 3.7: (a) Representation of the three singly occupied orbitals using a maximally localized basis set, which shows that each spin is mostly located on an individual triangulene corner. (b) Spin-spin correlation between each pair of spins computed using the orbital representation in (a). This picture allows the description of the magnetic state of **TTAT** in terms of a symmetric Heisenberg ferromagnetic trimer, as illustrated in (c). According to this model the experimental quartet-doublet energy gap of 15 meV corresponds to an exchange coupling $J = 10$ meV[135].

The localization of spin fingerprints at the three vertices suggests that the open-shell character of **TTAT** could be described by three spatially localized radicals rather than a set of overlapping SOMOs. Using a maximally localized orbital basis set, we obtain a representation where each of the three unpaired electrons is mostly located at an individual triangulene corner, as displayed in the SOMOs in Figure 3.7a. We computed the spin-spin correlation $A_{ij} = \langle \hat{S}_i \hat{S}_j \rangle - \langle \hat{S}_i \rangle \langle \hat{S}_j \rangle$ for each pair of spins i and j in those maximally localized orbitals. The results, illustrated in Figure 3.7b, confirm the ferromagnetic coupling between three unpaired spins in the ground state with a value of the spin-spin correlation $A_{ij} = 0.22$ au.

This representation suggests the possibility of describing the triradical molecule **TTAT** as a symmetric Heisenberg $S = 1/2$ trimer[135]. Considering an equal ferromagnetic coupling J between the three unpaired spins (Figure 3.7c),

a Heisenberg spin model yields a ground state with total spin $S = 3/2$ and two degenerate doublets ($S = 1/2$) as first excited states, similarly to the results of the many-body CASSCF calculations. In the case of an equilateral Heisenberg trimer, the exchange J is given by $J = \frac{2}{3}\Delta E$, where ΔE is the quartet-doublet energy difference. Therefore, considering the experimental excitation energy $\Delta E = 15$ meV, we determine for **TTAT** an exchange coupling $J = 10$ meV, in good agreement with the value of 9 meV obtained from the fit to the STS data using the perturbative model by Ternes[85].

3.5 Conclusions

In summary, we have presented a polyradical aza-nanographene (**TTAT**) hosting three unpaired π electrons localized at the vertices of a triangle and coupled through symmetric ferromagnetic interactions.

The system was designed by combining well-known molecular building blocks, all-carbon and N-doped [3]triangulenes, and fabricated via a combination of in-solution and on-surface synthesis. The detection of clear magnetic fingerprints in scanning tunneling spectroscopy (i.e., both a weak Kondo resonance and IETS step-like features) demonstrated the open-shell and polyradical character of the molecule on Au(111). Combining differential conductance spectra and orbital maps with DFT and multi-configurational calculations, we revealed the presence of three radical units and their ferromagnetic alignment, resulting in a $S = 3/2$ (quartet) ground state, and showed that the molecule can be described as a Heisenberg ferromagnetic spin-1/2 trimer.

The evidence of multi-radical interactions and the high-spin configuration make this system a suitable platform for the exploration of magnetic states in extended molecular structures. More broadly, our results demonstrate that triangulene units can be strategically coupled through their zigzag edges, giving rise to more complex nanostructures with customized spin states.

3.6 Appendix

3.6.1 Second derivative spectra

We report here the low-bias d^2I/dV^2 spectra as obtained by numerical differentiation from a grid of dI/dV spectra. The peaks corresponding to the Kondo resonance and the spin excitation are marked in the plot. Those energies are selected to map the spatial distribution of the two signals, as shown in Figures 3.2b-c in the main text.

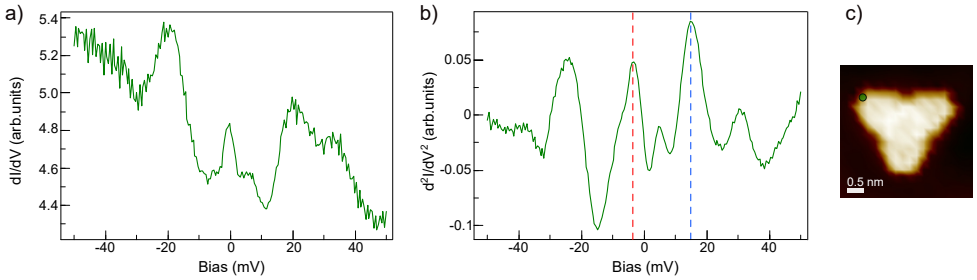

Figure 3.8: Single dI/dV spectrum (a) and corresponding d^2I/dV^2 plot (b) extracted from a dI/dV grid in the position indicated in (c). Alongside the Kondo and spin excitation features, we can observe inelastic steps around $V = \pm 5$ mV and $V = \pm 35$ mV that originate from vibrational modes of the CO molecule attached to the tip. The red and blue dashed lines in (b) indicate the peaks (at $V = -3.3$ mV and $V = 15$ mV) that were selected to map the spatial distribution of the Kondo and the spin excitation feature, respectively, as reported in Figures 3.2b-c in the main text. Parameters: $V = 50$ mV, $I = 1$ nA, $V_{mod} = 2$ mV.

3.6.2 Complementary theoretical results

DFT simulations First-principles calculations were performed using density-functional theory (DFT) implemented in the SIESTA code using the PBE generalized-gradient approximation.[4] The energy level diagram and the orbital isosurfaces of the single-particle states are reported in Figure 3.9.

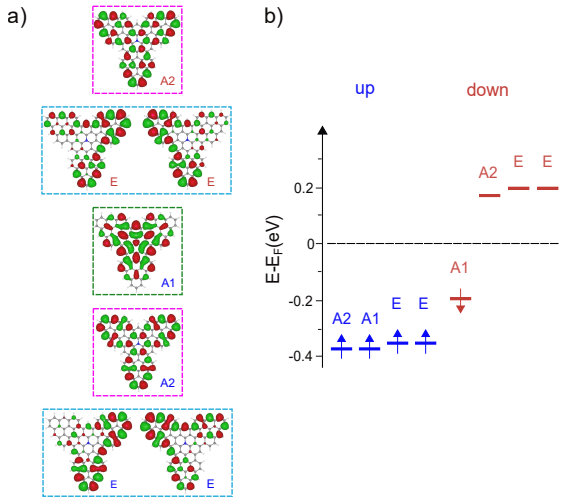

Figure 3.9: (a) Molecular orbital isosurfaces corresponding to the single-particle states shown in the energy level diagram in (b) obtained from spin-polarized DFT calculations. The labels refer to the symmetry of each orbital, defined in terms of irreducible representations of the C_{3v} symmetry point group. The singly occupied orbitals are three: two degenerate orbitals with E symmetry, and one with A2 symmetry. The only orbital with the highest intensity on the N site is the A1, which is fully occupied.

CASCI calculations We report here the results from the complete active space configuration interaction (CASCI) method, employed to obtain an accurate description of the wave function and electronic energies. The full many-body Hamiltonian was constructed from these integrals in the π-orbital subspace of 11 electrons in 11 orbitals and diagonalized in our in-house many-body code. By diagonalizing the one-particle density matrix from the ground state CASCI wavefunction, we have calculated the occupation of natural orbitals and constructed the natural orbitals, see Figure 3.10b. The fractional occupation of natural orbitals gives an insight into the radical character of the molecules within the many-body framework.

[4]DFT calculations performed by Hassan Ahmoum and Emilio Artacho (CIC NanoGUNE, San Sebastián, Spain).

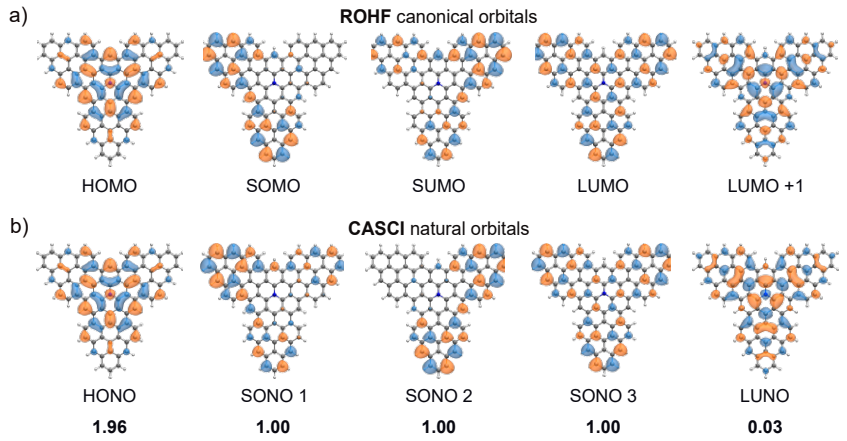

Figure 3.10: a) Restricted open-shell Hartree-Fock (ROHF) orbitals and (b) complete active space configuration interaction (CASCI) natural orbitals of **TTAT**. The numbers below the natural orbitals indicate their fractional electronic occupation. As for the CASSCF calculations reported in the main text, three singly occupied natural orbitals (SONO) are obtained.

Natural Transition Orbitals (NTO) To simulate the dI/dV maps corresponding to IETS spin excitation maps, we have calculated the Natural Transition Orbtals (NTOs)[136], which correspond to the electronic transition density matrix of single spin flip process from the quartet ground state to the doublet excited states obtained from CASCI calculations. Figure 3.11 displays the calculated NTOs with corresponding amplitudes.

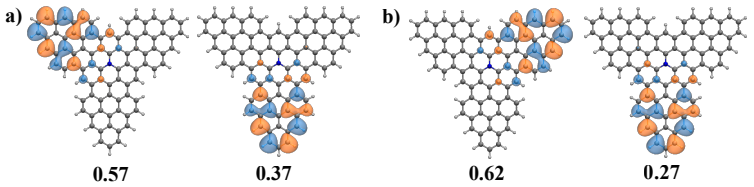

Figure 3.11: NTOs for the spin excitation from quartet ground state to a) first doublet and b) second doublet.

Kondo Orbitals (KO) Kondo orbitals are calculated by diagonalizing the Hamiltonian derived from the multi-channel Anderson model, which considers the many-body multiplet structure of molecules obtained from the CASCI calculation for the neutral ground state and virtual charge states[132]. The computed KOs and their coupling to the substrate are reported in Figure 3.12.

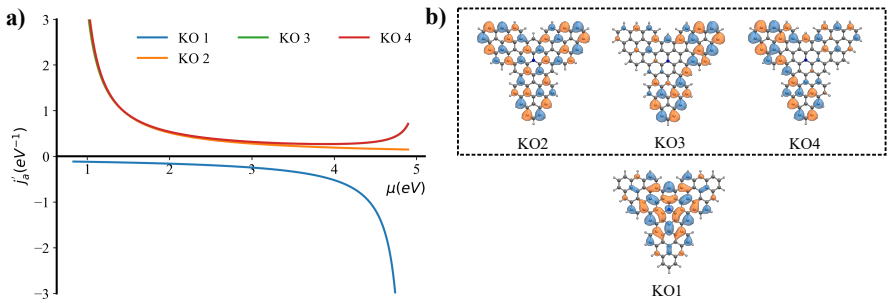

Figure 3.12: Results from the multi-orbital Kondo analysis, used to simulate the Kondo spatial distribution map presented in the main text. (a) Coupling constants j_a computed as a function of the chemical potential for each Kondo orbital (KO). (b) Orbital isosurfaces of the four KOs with non-zero coupling to the conduction electrons of the substrate at a chemical potential of 3 eV. Three of these orbitals (highlighted in the dashed box) correspond to channels with antiferromagnetic coupling ($j_a > 0$) to the electron bath and therefore are involved in the many-body Kondo screening process.

Dyson Orbitals In Figures 3.13 and 3.14 we report the calculated Dyson orbitals and their amplitudes for removal/addition of a single electron. As described in the main text, Dyson orbitals were used to simulate the experimentsl dI/dV maps (Figure 3.3c).

Theoretical dI/dV maps of NTOs and Kondo orbitals were calculated by the Probe Particle Scanning Probe Microscopy (PP-SPM) code[129] for a CO-like tip. For NTO we have chosen the tip composed of pxpy (90%) and s (10%) orbitals while for Kondo orbitals the tip is composed of pxpy (85%) and s (15%) orbitals to match the experimental dI/dV maps.

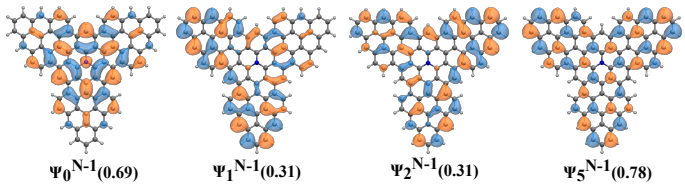

Figure 3.13: Dyson orbitals for the process of removal of one electron with the norm of the wavefunction below.

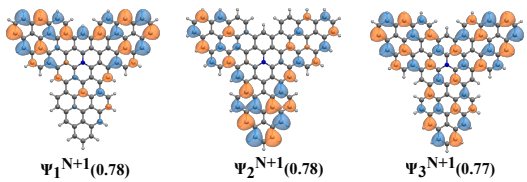

Figure 3.14: Dyson orbitals for the process of adding one electron with the norm of the wavefunction below.

4 Collective spin states in a triangulene-based hexamer

In the previous chapter we have shown that triangulene building blocks can be combined to generate a larger open-shell graphene nanostructure, exhibiting a higher spin state than the original units, and containing three unpaired π electrons. Here we go a step further and investigate spin interactions in a macrocycle formed by six [3]triangulenes, obtained via a combination of in-solution and on-surface synthesis. This triangulene-based hexamer hosts 12 unpaired π electrons, which give rise to a many-body singlet ground state originated by the antiferromagnetic interaction of six $S = 1$ spin units. We use inelastic electron tunneling spectroscopy to detect collective spin excitations from the ground state to many-body triplet states, and demonstrate that the system can be described as a Heisenberg S = 1 spin ring. Furthermore, we study the effects of opening the ring macrocycle by investigating the magnetic properties of a hexamer with a quenched radical unit and of open-ended triangulene chains.

Part of the results reported in this Chapter are published as an article in *Angewandte Chemie International Edition*.

- On-Surface Synthesis and Collective Spin Excitations of a Triangulene-Based Nanostar

  Jeremy Hieulle, Silvia Castro, Niklas Friedrich, Alessio Vegliante, Francisco Romero-Lara, Sofía Sanz, Dulce Rey, Martina Corso, Thomas Frederiksen, Jose Ignacio Pascual and Diego Peña.

  Angewandte Chemie International Edition **2021**, 60, 25224.

  https://doi.org/10.1002/anie.202108301

4.1 Introduction

The [3]triangulene, with its $S = 1$ ground state, represents the perfect building block for the design of open-shell carbon-based nanostructures with different spin quantum numbers. During the last years, indeed, several triangulene-based nanographenes, exhibiting different magnetic states, have been generated via on-surface synthesis[37,57,137]. Some of these nanostructures display characteristic low-energy spectral fingerprints associated with spin excitations induced by inelastic tunneling electrons[23,27]. As shown in the previous chapter, such inelastic features allow to quantify spin interactions in nanographenes and to test current theoretical models for describing many-body spin states.

In this chapter, we present the synthesis and characterization of a new triangulene derivative consisting in six [3]triangulenes coupled at their vertices, thus forming the macrocycle **TNS** (Triangulene-based NanoStar, shown in Figure 4.1). This molecule is particularly appealing due to its large number of unpaired electrons (twelve) organized in a cyclic structure, which makes it a model system for investigating collective interactions in a spin ring.

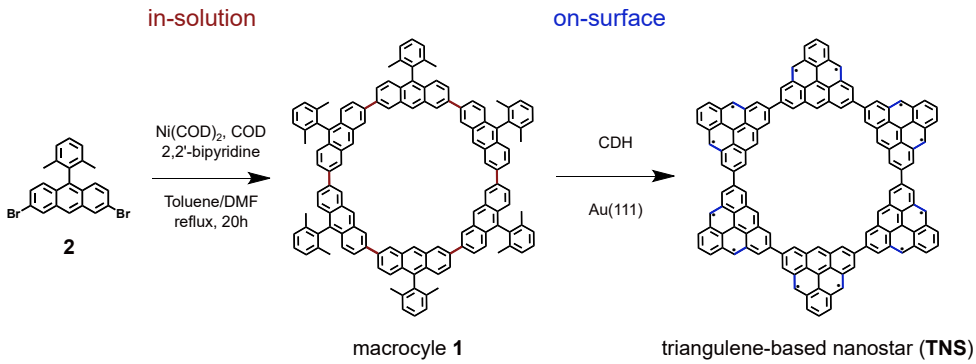

Figure 4.1: Schematic representation of the synthesis of the triangulene-based nanostar (**TNS**), obtained through a combination of in-solution and on-surface chemistry. The first step is the in-solution coupling of 2,7-dibromo-10(2,6-dimethylphenyl)-anthracene molecules (**2**), which results in the macrocycle **1**. The second step consists in surface-assisted cyclodehydrogenation (CDH), which forms the C-C bonds marked in blue, leading to the generation of the **TNS**.

We envisioned the preparation of the **TNS** via a combination of in-solution and on-surface synthesis, as illustrated in Figure 4.1. First, triangulene precursors, each consisting of a di-brominated anthracene core attached to a dimethylphenyl group (**2**), were coupled in solution to generate the macrocycle

1.[1] Then, the on-surface cyclodehydrogenation (CDH) of **1** was activated on Au(111) in one annealing step, leading to the generation of the **TNS** via the formation of twelve C-C bonds (highlighted in blue in Figure 4.1).

We also explored an alternative route for the synthesis of the **TNS**, consisting in the on-surface Ullmann-like coupling of precursors **2**, followed by a CDH reaction step. This pathway, however, did not lead to the formation of the hexamer but resulted instead in a wide variety of triangulene-based oligomers, including open-ended triangulene chains. We will describe these different products in the final part of the chapter, demonstrating that the breaking of the cyclic structure results in a modification of the spin state of the system and in the emergence of peculiar edge states[138].

4.2 On-surface synthesis of the TNS

Considering the large molecular mass of macrocycle **1**, we sublimated it via flash-annealing of a silicon wafer loaded with grains of the compound. Figure 4.2a shows an overview STM image of the Au(111) substrate after deposition. Molecular rings surviving thermal sublimation appear in closed-packed molecular islands, surrounded by polymeric fragments, probably from rings broken during the thermal sublimation: for the coverage of Figure 4.2a, about 8 % of the material deposited corresponds to the intact precursor **1**. Individual precursors can be extracted from the domains by lateral manipulation with the STM tip. This is achieved by stabilizing the tip at the centre of a macrocycle (setpoint: $V = 5$ mV; $I = 3$ nA) before opening the feedback and slowly moving the tip laterally. As shown in Figure 4.2b, the individual precursors appear in STM images as six protruding lobes corresponding to the six dimethylphenyl groups attached to the anthracenes moieties.

To induce the full planarization of the macrocycle **1** and generate the targeted **TNS**, we annealed the substrate to 330°C. At this temperature, the CDH reaction is activated at the methyl groups, resulting in the formation of twelve C-C bonds per hexamer (blue in Figure 4.1). However, due to the high temperatures required to fully planarize the whole rings and to their radical character, the CDH competes with additional C-C coupling and bond-breaking reactions, resulting in a few isolated **TNS** and in the formation of many triangulene oligomers, as shown in Figures 4.2c-d. Bond-resolved scanning tunneling microscopy (BR-STM) images of individual molecular rings, obtained using a CO functionalized STM tip, resolved the triangulene units

[1] In-solution synthesis operformed by Silvia Castro, Dulce Rey, Diego Peña (CiQUS and Universidade de Santiago de Compostela, Santiago de Compostela, Spain).

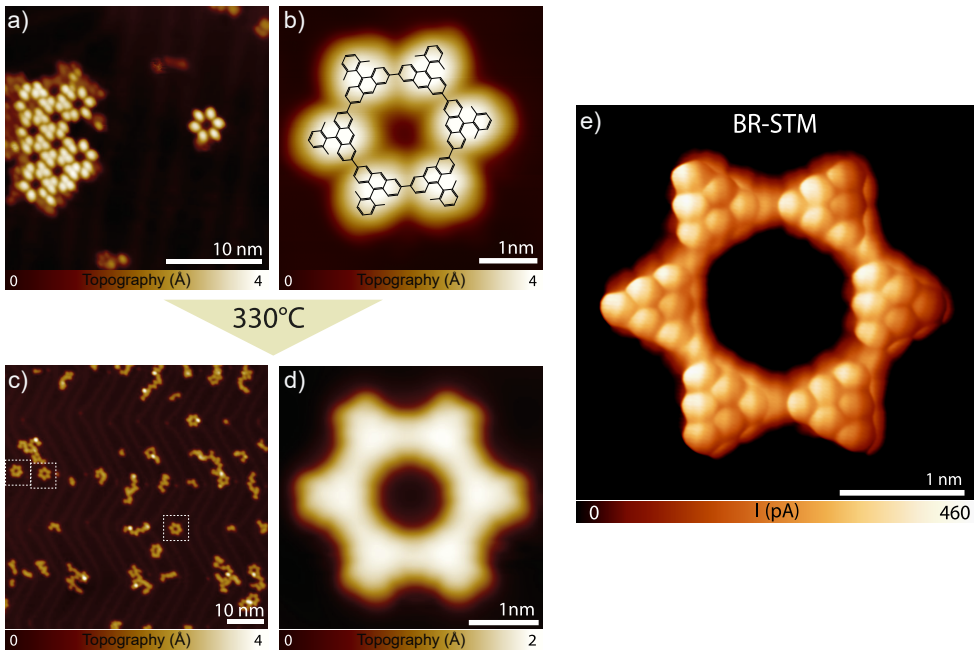

Figure 4.2: (a) STM image ($V = 0.5$ V; $I = 60$ pA) recorded after sublimating the macrocycle **1** onto Au(111) via flash evaporation. Closed-packed molecular islands are formed upon deposition. The individual molecule in the image ($V = 0.2$ V; $I = 40$ pA) in (b) was separated from the island via tip manipulation. (c) Overview STM image ($V = 1$ V; $I = 40$ pA) recorded after annealing the sample. Several triangulene oligomers are obtained, but also a few isolated **TNS**, as the one highlighted in the close-up image ($V = 1$ V; $I = 100$ pA) in (d). The successful on-surface generation of the triangulene nanostar is confirmed by the constant-height bond-resolved STM image ($V = 5$ mV) reported in (e).

connected in a closed ring structure (Figure 4.2e), demonstrating the successful on-surface generation of the **TNS**. Each individual [3]triangulene hosts two unpaired π electrons, coupled through a strong ferromagnetic exchange interaction[27]. Therefore, the resulting structure can be seen as a ring of six S=1 spin units, one for each triangulene, which are expected to interact through the π-conjugated system and stabilize a collective spin state.

4.3 Unravelling multiple spin excitations

A first insight into the spin state of the ring was obtained by mean-field Hubbard (MFH) simulations. As illustrated in the spin density map in Figure 4.3a, the intramolecular parallel magnetic coupling remains strong in the **TNS**, building a total spin $S = 1$ in each triangulene, and dominating over a weaker

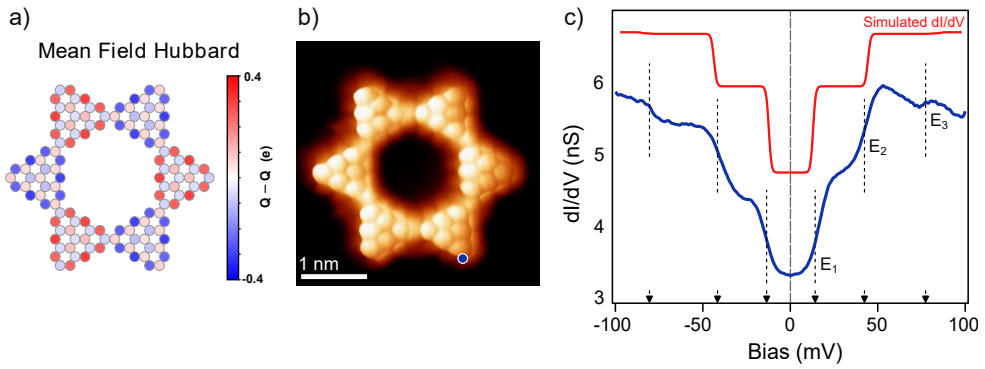

Figure 4.3: (a) Spin density map of the **TNS** obtained from mean-field Hubbard simulations with an on-site Coulomb potential U = 3.5 eV. (b) Bond-resolved constant-height STM image of the **TNS** indicating the position where the spectrum in (c) was measured. (c) dI/dV spectrum taken on the triangulene unit in (b), displaying three inelastic steps at $E_1 = \pm 14$ mV, $E_2 = \pm 42$ mV and $E_3 = \pm$ 80 mV. Parameters: $V = 100$ mV, $I_{set} = 500$ pA, $V_{mod} = 2$ mV. The red line represents a simulation of the spectrum. obtained from the Heisenberg model with exchange constant J = 18 meV, as explained in the text.

anti-parallel coupling between neighbouring triangulene units. Such interaction pattern is expected to lead to a global spin singlet ground state. Interestingly, antiferromagnetic (AFM) rings of integer spins have been widely studied theoretically for demonstrating the Haldane conjecture[139], stating that the spin excitation spectrum of an infinite Heisenberg $S = 1$ AFM chain remains gapped, with an energy value close to 0.4 J (J being the Heisenberg exchange constant). Such a gapped spectrum is an anomalous behavior of integer AFM spin chains, which contrasts with the gapless spin excitation spectrum of similar chains made of half-integer spins (Heisenberg chains)[140,141].

To experimentally determine the spin configuration of the **TNS**, we probed the excitation spectrum by means of Inelastic Electron Tunneling Spectroscopy (IETS)[67,142]. We measured dI/dV spectra over the edges of the triangulene units. As shown in Figure 4.3c, the spectra display bias-symmetric steps, which can be interpreted as fingerprints of spin excitations induced by inelastic electron tunneling. Specifically, we observe three steps of different height centered at $E_1 = \pm 14$ mV, $E_2 = \pm 42$ mV and $E_3 = \pm 80$ mV. The first two dI/dV steps have similar height (each amounting to a relative increase of conductance of ≈ 35 %), while the third one appears with a smaller spectral weight (<7 %).

As illustrated in Figures 4.4a-b, the same stepped spectral features are found across the different triangulene units of the hexamer. Furthermore, the stacked dI/dV plot of Figure 4.4c clearly shows that the inelastic signal is

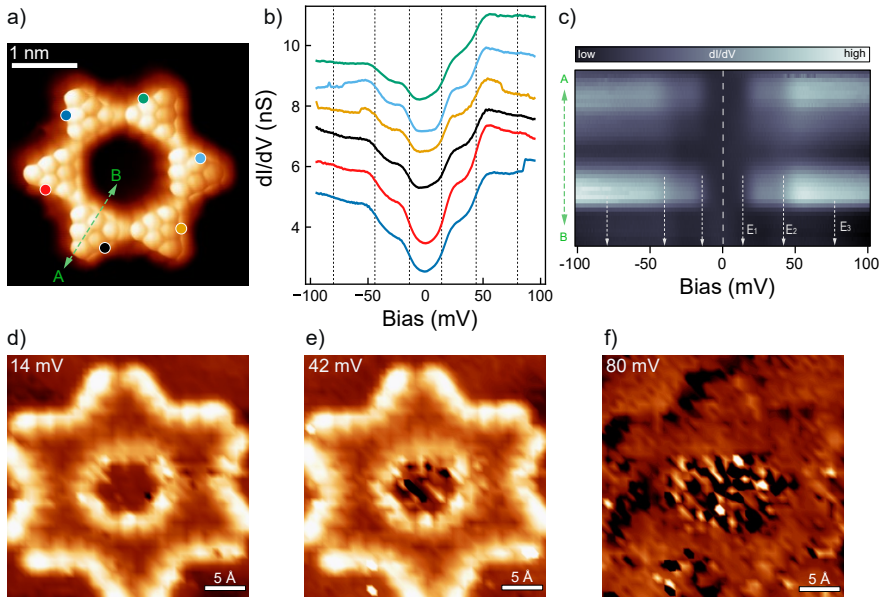

Figure 4.4: (a) Bond-resolved constant-height STM image of the **TNS** indicating the positions where the spectra in (b) and (c) were measured. (b) dI/dV spectra taken on the six triangulene units, displaying the same stepped features at the same bias onsets. (c) dI/dV stacked line plot measured along one triangulene unit, in the direction indicated in (a). The plot clearly shows the localization of the inelastic signal on the triangulene edges. Spectroscopy parameters: $V_{set} = 100$ mV, $I_{set} = 100$ pA, $V_{mod} = 2$ mV; individual spectra were offseted to appear with the same zero-bias conductance. (d-f) d^2I/dV^2 maps recorded at the bias values corresponding to the onset of each of the three spin excitation steps. The maps were obtained by numerical derivation of a grid of dI/dV spectra taken over the whole **TNS**.

mostly localized over the edges of the triangulenes. Such localization effect is also pictured by mapping the derivative of the differential conductance at the energies corresponding to the onset of the three spin excitation steps. The resulting d^2I/dV^2 maps, reported in the Figures 4.4d-f, show indeed a strong signal over the edges, in particular at the onset of the first and second spin excitations, while the signal associated to the third excitation appears much fainter. These results confirm that the excitation probability of the collective spin states of the **TNS** coincides with the larger spin density over the edge sites of the triangulenes, as expected for π-radical states[23,42,58].

The presence of three spin excitation steps in the dI/dV spectra is a remarkable feature that contrasts with the single-stepped spectra that were measured in [3]triangulene dimers[27] and in other graphene nanostructures[23,42,43,58,143]. Due to the $\Delta S = 0, \pm 1$ selection rule imposed by conservation of the angular momentum[27,67], these IETS steps were attributed to singlet-triplet transitions

induced by the tunneling electrons. Similar single-stepped spectra would be expected also for the **TNS** according to the classical picture provided by the MFH simulations (Figure 4.3a). Therefore, the multi-step features observed in our spectra unveil a complex excitation pattern of collective spin states in the ring, which imposes to turn to a different theoretical model to describe the magnetic properties of the system.

4.4 Many-body singlet ground state and collective spin excitations

To explain the origin of the multiple inelastic steps, we modeled the coupled spin system with an isotropic Heisenberg Hamiltonian

$$\hat{H}_{Heisenberg} = J \sum_i \vec{S}_i \cdot \vec{S}_{i+1}, \tag{4.1}$$

where $\vec{S}_i$ represents the spin-1 operator at the i unit, and J the exchange coupling.[2]

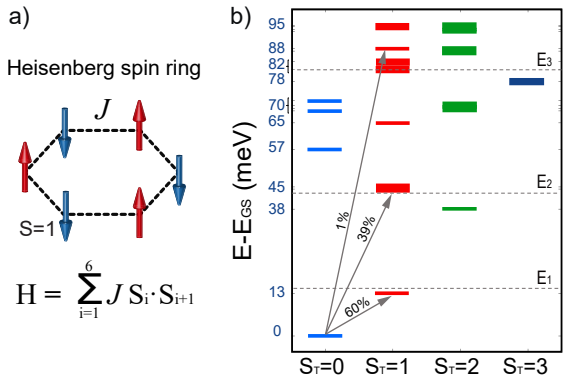

Figure 4.5: (a) Schematic model of a six-membered S=1 spin ring, simulated using the Heisenberg spin Hamiltonian written below. (b) Diagram representing the excitations of the collective spin states as obtained from the model in (a) with J = 18 meV. Only excited states up to a total spin $S_T = 3$ are shown here. Thin/thick lines indicate singly/doubly degenerate total spin states, while the arrows highlight the three dominant transitions induced by tunneling electrons, which coincide in energy and weight with the three steps observed in the dI/dV spectra.

We considered a closed ring of six $S = 1$ spins coupled though an AFM exchange interaction ($J > 0$), as shown in the model in Figure 4.5a. The many-

[2]Calculations performed by Sofía Sanz, Thomas Frederiksen (Donostia International Physics Center, San Sebastián, Spain), Niklas Friedrich and Francisco Romero-Lara (CIC NanoGUNE, San Sebastián, Spain).

body ground state of the **TNS**, obtained by exact diagonalization of the spin Hamiltonian, has a total spin $S_T = 0$, corresponding to a global singlet, and consists in the superposition of the classical solutions of antiferromagnetically coupled triangulene units (i.e., the ground state from the MFH model in Figure 4.3a), and other combinations of the triangulene spins resulting in a global singlet ($S_T = 0$). Similarly, the set of excited states are collective spin modes with total spin amounting from $S_T = 0$ to $S_T = 6$, which can also be described as superpositions of triangulene $S = 1$ multiplet states.

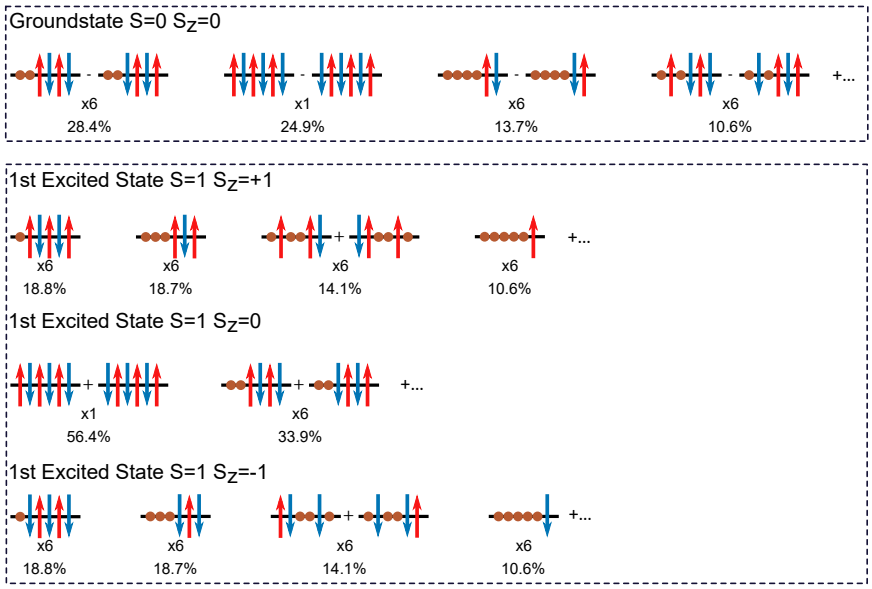

Figure 4.6: Schematic representation of the most relevant combinations of $S = 1$ triangulene spins contributing to the ground state and first excited state of the **TNS**, as obtained with the Heisenberg model. The individual triangulene $S = 1$ multiplet states are represented with a red or blue arrow ($S_z = 1$ and $S_z = -1$, respectively) or with a filled circle ($S_z = 0$). The numbers below each term indicate the multiplicity and the contribution to the total many-body state.

To rationalize the excitation spectrum, we consider that the IETS steps correspond to transitions with $\Delta S = \pm 1$ and adjust the Heisenberg exchange constant J to fit the lowest allowed excitation with the first dI/dV step (centered at ± 14 mV). The best spectral match occurs using J = 18 meV. Figure 4.5b shows the computed excitations with energy up to 100 meV, classified according to their global spin (up to $S_T = 3$). Several singlet and triplet excited states appear within the energy window of the IETS spectrum, including triplet states grouped around the excitation energy values $E_1 = \pm 14$ mV, $E_2 = \pm 42$ mV and $E_3 = \pm 80$ mV, in agreement with the three dI/dV steps

in the experimental spectra. A representation of the singlet ground state and the first triplet excited state in terms of combinations of individual triangulene $S = 1$ multiplet states is reported in Figure 4.6.

To explain the different dI/dV step heights found in the experiment, we calculated the cross-section of each spin transition following the expression[85]:

$$|M_{mn}|^2 = \frac{1}{2}\left|\langle m|\hat{S}_+|n\rangle\right|^2 + \frac{1}{2}\left|\langle m|\hat{S}_-|n\rangle\right|^2 + \left|\langle m|\hat{S}_z|n\rangle\right|^2, \tag{4.2}$$

where n and m indicate the initial and final states, respectively, while $\hat{S}_+$, $\hat{S}_-$ and $\hat{S}_z$ represent the raising, lowering, and z-projection spin operators, respectively, acting on a specific spin-1 unit.

This quantity reflects the scattering probability of a tunnel electron with every collective spin eigenstate and, thus, is related to the step height of the inelastic signal. The first excitation at 13 meV has the largest spectral weight (60 %, as shown by arrows in Figure 4.5b), while several states bundled at around $E_2 = 45$ meV contribute to most of the remaining weight (39 %). Higher states are weaker in terms of spectral weight and produce a faint step in spectrum. A table with the results from the solution of the Heisenberg spin Hamiltonian, including all the eigenstates with energy below 100 meV, their degeneracy, and the cross-section of the active excitations is reported in the Appendix (Figure 4.11).

The simulated spin excitation spectrum shown in Figure 4.3c (red plot) reproduces with good agreement the position and the height of the three steps observed in the experimental dI/dV curve. There are, however, small differences in the step positions and in the relative height that can be accounted for by including a more precise description of spin interactions. In our model, in fact, we consider six $S = 1$ spin units due to the strong ferromagnetic coupling within the individual trangulenes. However, we can also include a finite intra-triangulene coupling and apply the Heisenberg model to a system of twelve S=1/2 spins. As we show in the Appendix Section 4.8.2, this allows to better reproduce the equal height of the first and the second excitation steps.

4.5 Defect-induced modifications of the spin state of the TNS

In addition to the pristine **TNS**, we obtained several rings with structural defects, such as non-planar regions, missing units, or quenched spins. Here we focus on a planar molecule showing a bright triangulene in bond-resolved STM imaging (Figure 4.7c). The increased low-bias current signal detected

on a single triangulene indicates the breaking of the six-fold symmetry of the **TNS** and suggests the presence of a localized radical state[23]. As indicated by the arrow in Figure 4.7c, a distorted and sharp carbon ring appears in the neigbouring triangulene. In bond-resolved STM, this feature is a well-known fingerprint of an sp^3-hybridized carbon, bonded to an additional hydrogen atom[22,38,57]. The presence of the extra H is expected to quench one of the two radical units of the triangulene, resulting in a significant modification of the overall spin state of the hexamer, as discussed below.

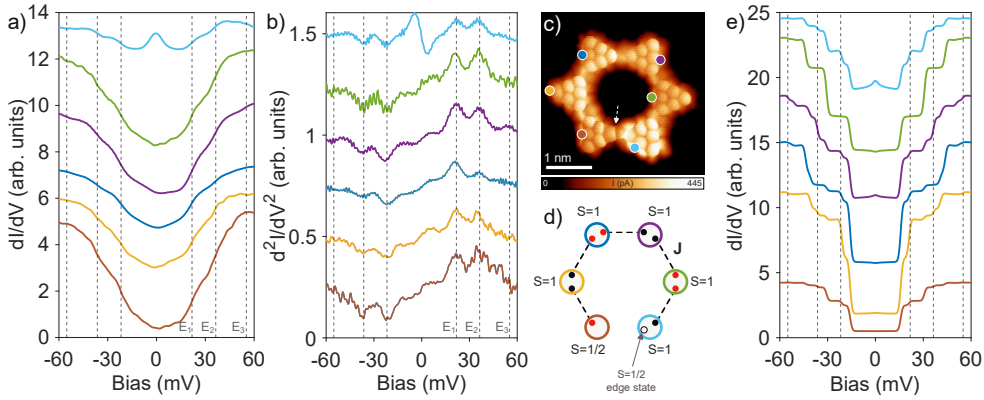

Figure 4.7: (a) dI/dV spectra measured with a CO-functionalized tip on a **TNS** with a defective triangulene unit, reported in the STM bond-resolved image in (c). The spin excitation step-like features appear centered at the bias values $E_1 = \pm 21$ mV, $E_2 = \pm 36$ mV and $E_3 = \pm 55$ mV (dashed grey lines). Additionally, a Kondo resonance is observed at a single triangulene unit. The weaker low-energy step features can be attributed to the excitation of translational modes of the CO molecule on the tip apex[125]. Parameters: $V_{set} = 80$ mV, $I_{set} = 500$ pA, $V_{mod} = 2$ mV. (b) Corresponding d^2I/dV^2 spectra obtained by numerical differentiation of the experimental dI/dV data, enabling the determination of the energy onset of the excitations. (c) Constant-height bond-resolved image recorded at $V = 5$ mV. The molecule displays a brighter triangulene, likely due to the presence of an additional H atom in the neighbouring unit, as indicated by the arrow. (d) Model of an open chain of five S=1 spin units, with an extra S=1/2 unit linked to one end of the chain. All the spin units interact through the same Heisenberg exchange constant J. In the valence-bond solid picture, each $S = 1$ unit is described as the union of two $S = 1/2$ spins (smaller circles, where red and black represent spin up and spin down, respectively). (e) Simulated dI/dV spectra corresponding to the spin system in (d), obtained using the program by Ternes[85], with a Heisenberg exchange $J = 18$ meV, as in the case of the pristine **TNS**. The dashed vertical lines indicate the energies corresponding to the onset of the excitation steps observed in the experimental dI/dV spectra.

Differential conductance spectra measured in the bias range (60 mV, -60 mV) reveal a Kondo resonance on the unit appearing brighter in the bond-resolved image, while all the other triangulenes show only step-like inelastic features (Figure 4.7a).

Now the IETS steps appear centered at the bias values $E_1 = \pm 21$ mV, $E_2 = \pm 36$ mV and $E_3 = \pm 55$, as clearly seen in the corresponding d^2I/dV^2 spectra in Figure 4.7b. The deviation of the energies of the inelastic features from those measured in the pristine **TNS** (Figure 4.3), indicates a variation of the collective spin states of the system, probably caused by the local structural modification.

To rationalize these observations, we simulated the experimental dI/dV spectra using the perturbative model by Ternes[85], applied to the spin system represented in Figure 4.7d. We considered five $S = 1$ units, corresponding to the pristine triangulenes, and one $S = 1/2$ unit (brown in the model) to account for the triangulene with a single unpaired electron, resulting from the presence of the additional H atom. We also assumed a negligible interaction between the $S = 1/2$ unit and the neighbouring $S = 1$ triangulene closest to the extra H (blue unit in Figure 4.7d), resulting in an open-ended structure, as shown in the model. Considering then the same Heisenberg exchange coupling used in the simulations for the pristine **TNS** ($J = 18$ meV), we obtained the dI/dV spectra reported in Figure 4.7e.

We observe that the simulations qualitatively reproduce the experimental results, revealing multiple IETS steps in all units and a Kondo resonance localized at the $S = 1$ end of the chain, but absent on the defective triangulene (the $S = 1/2$ unit in the simulations). However, the number of the spin excitations as well as their energies clearly do not match the experimental data. The poor quantitative agreement with the STS results highlights the limitations of the Heisenberg model in reproducing the spin properties of $S = 1$ open chains. Indeed, as shown by Mishra et al. in their work on triangulene-based Haldane chains[138], the IETS features measured on such systems are better captured within the framework of the BLBQ model, considering the spin-1 Hamiltonian

$$\hat{H}_{BLBQ} = J \sum_i \left[\vec{S}_i \cdot \vec{S}_{i+1} + \beta (\vec{S}_i \cdot \vec{S}_{i+1})^2 \right], \tag{4.3}$$

which includes both bilinear and biquadratic exchange terms (with β being a parameter that determines the relative strength of the biquadratic term)[141].

The ground state solution for an AFM chain is given by the so-called valence-bond solid[138,140]. In the case of an $S = 1$ chain, each unit can be described as the sum of two virtual $S = 1/2$ spins, as shown in Figure 4.7c. The formation of singlet states between virtual spins belonging to adjacent AFM coupled $S = 1$ units results in the emergence of a global singlet ground state and, interestingly, in the appearance of $S = 1/2$ unpaired spins at the chain edges (fractional edge states). According to this description, the Kondo

resonance observed in our spectra can be related to the edge state located at the $S = 1$ terminal unit of the chain. This picture also accounts for the absence of Kondo features at the opposite chain end: the unpaired electron provided by the triangulene with the additional H atom, in fact, forms a singlet with one of two two $S = 1/2$ spins of the adjacent unit, quenching the edge state that would be expected there in the case of a pristine $S = 1$ chain.

4.6 Open-ended chains

Open-ended triangulene chains can be directly generated on Au(111) using the dibrominated triangulene precursor **2** already introduced in Figure 4.1 and reported here in Figure 4.8a. The deposition of this molecule, followed by surface-assisted intermolecular Ullmann-like coupling and CDH, can lead, in principle, to the formation of the **TNS**, but is more likely to result instead in the synthesis of non-cyclic structures (Figure 4.8a).

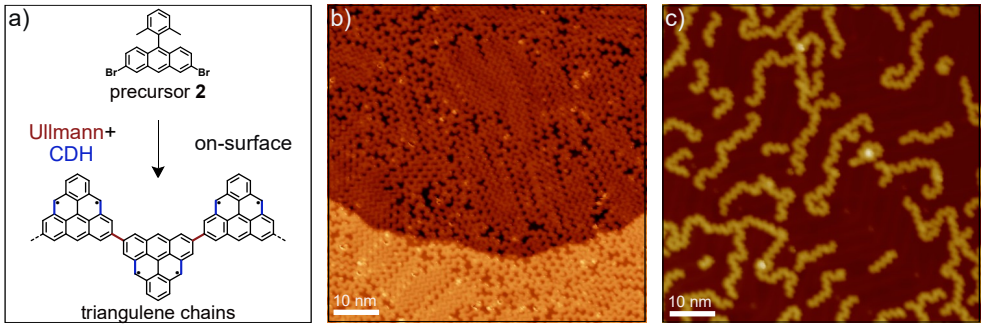

Figure 4.8: (a) Schematic representation of the on-surface synthesis of one-dimensional triangulene-based nanostructures from the 2,7-dibromo-10(2,6-dimethylphenyl)-anthracene precursor (**2**), consisting in two reaction steps: Ullmann-like coupling and CDH. (b) Overview STM image ($V = 2.5$ V; $I = 20$ pA) recorded after deposition of the precursor via flash evaporation and annealing in one step at $350°$C. The high coverage leads to the formation of long and interconnected triangulene chains. (c) STM image ($V = 1$ V; $I = 50$ pA) after deposition of a lower amount of precursor **2** and subsequent annealing at $340°$C, displaying now smaller structures, including isolated open-ended chains.

Indeed, planar triangulene-based one-dimensional nanostructures were easily obtained when depositing **2** onto Au(111) and subsequently annealing the sample at $340 - 350°$C, as displayed in the overview STM images in Figures 4.8b-c. The use of this debrominated precursor can result in the formation of oligomers of arbitrary length, including long and interconnected chains as those shown in Figure 4.8b, which extend over tens of nm, covering the surface terraces almost entirely and creating large and ordered molecular assemblies.

Tuning the amount of deposited molecules allows to obtain shorter and isolated structures (Figure 4.8c), thus enabling the investigation of triangulene chains with varying number of constituent units.

These systems have been already extensively studied by Mishra et al. in a recent work[138]. The authors provide there a systematic experimental characterization of open-ended chains with a number of triangulene units ranging between N=2 and N=20, and a description of their spin properties based on the BLBQ model (equation 4.3). Here we will focus on two representative structures obtained in our preparations.

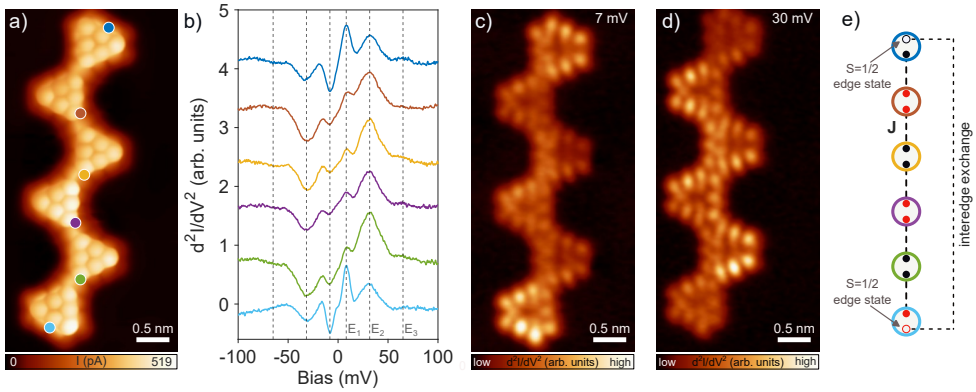

Figure 4.9: (a) Constant-height bond-resolved STM image ($V = 5$ mV) of a chain composed of six triangulene units. (b) d^2I/dV^2 spectra measured on the different units at the positions marked in (a). The dashed lines indicate the average energy onset of the three excitations measured in this energy range: $E_1 = \pm 9$ mV, $E_2 = \pm 32$ mV and $E_3 = \pm 65$ mV. Parameters: $V_{set} = 100$ mV, $I_{set} = 1$ nA, $V_{mod} = 5$ mV. (c-d) Constant-height d^2I/dV^2 maps recorded at bias values corresponding to the two lower excitation energies, revealing their spatial distribution. All measurements were performed with a CO-functionalized tip. (e) Representation of the N=6 open-ended chain in the valence-bond solid picture: each $S = 1$ unit is composed of two $S = 1/2$ spins, here represented as filled smaller circles (red and blue indicate spin up and down, respectively). The two edge states couple via an interedge exchange, as described in the text.

First, we investigated an open-ended chain composed of six triangulene units (Figure 4.9). The bond-resolved STM image reported in Figure 4.9a demonstrates the successful on-surface generation of a defect-free chain from precursor **2**. To characterize the spin properties of the system, we recorded d^2I/dV^2 spectra on all the triangulene units, as displayed in Figure 4.9b. The direct measurement of d^2I/dV^2 plots, in fact, allows us to better identify the energy onset of the inelastic spin excitations and their modulation over the different triangulene units. We observe three IETS features in the bias range (100 mV, -100 mV), corresponding to peaks centered at $E_1 = \pm 9$ mV,

$E_2 = \pm 32$ mV and $E_3 = \pm 65$ mV, with the third feature being much fainter than the two lower energy ones in all units.

The spin excitations appear at different energies compared to the **TNS**, despite the same number of constituent units, demonstrating the impact of the breaking of the cyclic structure on the spin state of the system. Furthermore, the loss of the equivalence among the units expected in the open-ended structure is reflected in the variations in the spectra observed across the different triangulenes, mainly with respect to the spectral weight of the spin excitations.

This is highlighted in the constant-height d^2I/dV^2 maps recorded at the energies corresponding to the onset of the two lowest spin excitations (Figures 4.9c-d). We observe that the signal associated to the first excitation is mostly localized on the terminal triangulene units, while the intensity of the signal recorded at the onset of the second spin excitation is much more intense over the internal units. This result is in agreement with the findings of the BLBQ model for $S = 1$ open-ended spin chains[138]. As already described in Section 4.5, in fact, the ground state of the system is represented by the valence-bond solid, characterized by a total spin $S = 0$ and featuring $S = 1/2$ edge states at the chain termini. These two states are expected to couple to each other through an antiferromagnetic exchange (Figure 4.9e), which decreases as the number of units increases. In small chains, such interedge exchange dominates over the Kondo coupling of the individual edge states with the substrate, resulting in the appearance of a low-energy singlet-triplet splitting in the dI/dV spectra. Therefore, the lowest energy inelastic feature (measured at $E_1 = \pm 9$ mV and spatially confined at the termini) can be attributed to the excitation of the singlet formed by the edge states, while the higher energy ones can be associated to many-body bulk excitations involving the total spin state of the chain, similarly to those observed in the **TNS**[138].

Finally, as reported in Figure 4.10, we investigated a chain made up of three triangulene units. The bond-resolved STM image recorded on the molecule (Figure 4.10) displays an increase in the low-bias current signal on one of the two terminal units, suggesting the presence of a $S = 1/2$ edge state. This is confirmed by differential conductance spectroscopy, that reveals a Kondo resonance only in the corresponding triangulene, as shown in Figure 4.10b. All three units then display inelastic spin excitations, centered at bias values around $E_1 = \pm 31$ mV and $E_2 = \pm 62$ mV, as can be better visualized in the corresponding d^2I/dV^2 spectra reported in Figure 4.10c.

The observation of a single $S = 1/2$ edge state can be explained considering the existence of a local defect in one of the two terminal units. As seen in the bond-resolved image in Figure 4.10a, in fact, the bottom triangulene contains a six-membered carbon ring appearing with an elongated shape. This

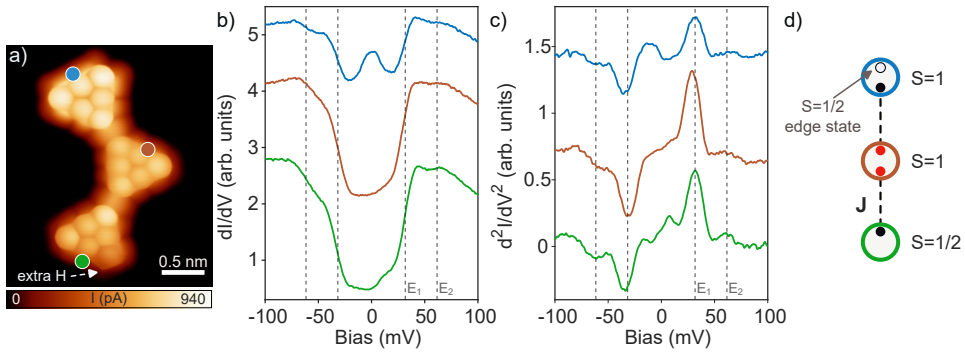

Figure 4.10: (a) Constant-height bond-resolved STM image ($V = 5$ mV) of a chain composed of three triangulene units, containing an additional H atom in the bottom unit, as indicated by the arrow. (b) dI/dV spectra measured on the three triangulenes, at the positions marked in (a). Parameters: $V_{set} = 100$ mV, $I_{set} = 500$ pA, $V_{mod} = 2$ mV. (c) d^2I/dV^2 spectra recorded at the same positions. The dashed lines highlight the two spin excitations revealed by the spectra: $E_1 = \pm 31$ mV and $E_2 = \pm 62$ mV. Parameters: $V_{set} = 100$ mV, $I_{set} = 1$ nA, $V_{mod} = 5$ mV. The measurements were performed with a CO-functionalized tip. (d) Representation of the spin state of the system in the valence-bond solid picture, revealing the existence of a $S = 1/2$ edge state only in one of the two terminal units.

indicates the presence of an additional H atom, which passivates one of the two unpaired electrons of this triangulene. According to the valence-bond solid picture, no edge state is expected at this chain end (model in Figure 4.10d), similar to what we observed in the hexamer with a defect discussed in Section 4.5. Consequently, the zero-bias resonance detected at the opposite terminal unit (the defect-free end) can be attributed to the Kondo screening of the corresponding $S = 1/2$ edge state, while the IETS steps measured across all the triangulenes are associated to transitions from the many-body singlet ground state to excited triplet states.

4.7 Conclusions

In conclusion, we have demonstrated the successful generation of a macrocycle of six [3]triangulenes through a combination of in-solution synthesis coupling and on-surface cyclodehydrogenation. We characterized the spin state of this triangulene-based ring by means of scanning tunneling spectroscopy, detecting collective spin excitations from a many-body singlet ground state to three triplet states. We showed that the spin excitation pattern exhibited by the hexamer follows the predictions of the Heisenberg model for a ring composed of six $S = 1$ spin units coupled through an antiferromagnetic exchange.

Furthermore, we investigated how the breaking of the cyclic structure affects the collective spin states of the system. Specifically, we characterized a ring with a quenched radical unit and two open-ended triangulene chains. In particular, we observed the emergence of $S = 1/2$ edge states at the termini of such non-cyclic structures, in agreement with theoretical predictions. We also highlighted the key role of extra H atoms, which can dramatically alter the spin configuration of the system.

Overall, our results demonstrate the potential of using the well-known [3]triangulene molecule as a basic unit for the realization of atomically precise one-dimensional nanostructures with different geometries, enabling the investigation and manipulation of complex spin states in all-organic molecular platforms.

4.8 Appendix

4.8.1 Transition rates of the spin excitations

We present here the results from the solution of the Heisenberg spin Hamiltonian, indicating the eigenstates with energy below 100 meV, their degeneracy (including S_z multiplets), and the transition probabilities of the excitations from the singlet ground state to different triplet final states. The excitation spectrum for scattering with tunneling electrons is dominated by three collective spin excitations, with the two lowest energy ones having a much higher spectral weight compared to the third excitation, in agreement with the experimental dI/dV spectra.

ENERGY VALUES (meV)	DEGENERACY
0	1
12,97	3
38,80	5
44,92	6
45,59	6
57,02	1
65,11	3
68,75	1
69,46	10
70,41	10
71,84	2
77,73	7
81,42	6
83,77	6
87,04	10
87,85	3
93,04	5
93,66	5
94,62	6

FINAL STATE	TRANSITION RATE	TRANSITION RATE (% norm)	%Excitation
1	0,40960853	20,003	
2	0,40960854	20,003	60,009
3	0,40960855	20,003	
9	0,17370307	8,483	
10	0,01507207	0,736	
11	0,03114157	1,521	
12	0,15816743	7,724	
13	0,1853627	9,052	
14	0,02403847	1,174	
15	0,02500253	1,221	39,272
16	0,03546538	1,732	
17	0,06588653	3,218	
18	0,02856793	1,395	
19	0,02181164	1,065	
20	0,0399678	1,952	
77	0,00490359	0,239	
78	0,00490359	0,239	0,718
79	0,00490359	0,239	
SITE 0 and 3		**100,000**	

Figure 4.11: Eigenstates (with energy up to 100 meV) of the Heisenberg Hamiltonian for a ring of six $S = 1$ units, and transition probabilities of the active excitations observed in this energy range.

4.8.2 Heisenberg model for a ring of twelve S=1/2 spins

We explored the effect of including a finite intra-triangulene ferromagnetic exchange coupling in the Heisenberg spin model. In this case we considered a ring of twelve $S = 1/2$ spin units:

$$\hat{H} = 4J' \sum_{i=1}^{6} \vec{S}_{2i-1} \cdot \vec{S}_{2i} + 4J \sum_{i=1}^{6} \vec{S}_{2i} \cdot \vec{S}_{2i+1}, \qquad \vec{S}_i = \vec{S}_{i+12}, \tag{4.4}$$

where $\vec{S}_i$ is the spin-1/2 operator on site i (two sites per triangulene), J and J' are the (antiparallel) inter- and (parallel) intra-triangulene exchange couplings, respectively. For comparison between the two case models a factor 4 is conveniently included (arising from normalization of the spin operators).

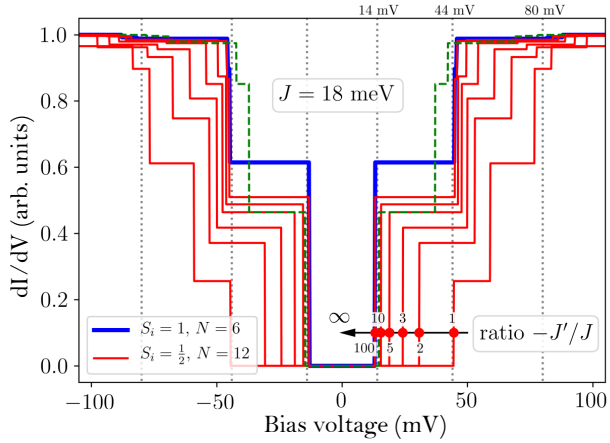

Figure 4.12: Simulated dI/dV spectra of the TNS as obtained using different models: (blue) ring of six $S = 1$ units, as described in the main text; (red) ring of twelve $S = 1/2$ units, with varying intra- and inter- triangulene exchange couplings. The best agreement with the experimental spectra is achieved for large but finite $-J'/J$ ratios; (green) ring of twelve $S = 1/2$ units with $J = 14$ meV and $-J'/J = 5$.

The comparison between the two models is shown in Figure 4.12 for fixed $J = 18$ meV and varying $-J'/J$ ratios. We observe that by including a large but finite value for J' (e.g., $-J'/J$ =10 or 100), the step heights of the first and the second excitations become similar in magnitude, as we find in the experiment and in contrast to the $\approx 60/40$ ratio obtained in the $S = 1$ model (blue curve in Figure 4.12 and Figure 4.3 in the main text). Thus, we conclude that a finite intra-triangulene coupling between the two unpaired electrons simulates better the experimental results.

We also considered the effect of a small intra-triangulene coupling J': as J' is reduced, we observe an upward shift of the excitation onsets, with the

first threshold shifting the most. By fixing the ratio $-J'/J$ to 5, we can fit the first experimental threshold energy by lowering the AFM coupling to $J = 14$ meV (green dashed curve in Figure 4.12). However, then the second step does not match the energy of the second excitation detected in the experiment: this confirms that the assumption $|J'| \gg |J|$ is still reasonable to describe the triangulene ring.

5 Towards two-dimensional triangulene-based networks

Following the on-surface synthesis and characterization of the polyradical graphene nanostructures reported in the previous chapters, here we explore strategies for fabricating extended carbon-based systems on metal surfaces, studying the potentiality of open-shell triangulene molecules as building blocks for two-dimensional covalent networks. We focus on different approaches based on distinct reaction pathways and molecular precursors. We will highlight the limitations of the different strategies and look for the best conditions and the most promising directions to overcome the challenges associated to the growth of ordered two-dimensional nanostructures.

5.1 Introduction

Since the first generation and characterization of the [3]triangulene, many efforts have been devoted to the realization of larger structures based on this paradigmatic open-shell molecule. In particular, as discussed earlier, different one-dimensional systems, from dimers to chains[27,126,138,144], have been synthesized via strategic Ullmann-like coupling and cyclodehydrogenation reactions on metal substrates, allowing the study of magnetic interactions and the build up of collective spin states.

Recently, theoretical investigations have started exploring the properties of triangulene-based *two-dimensional* (2D) crystals[145–147]. In these systems, the intermolecular hybridization between the zero-energy modes of neighbouring triangulenes is expected to give rise to weakly dispersive energy bands located close to the Fermi energy. Such bands are generally associated to strong electronic correlations leading to exotic phases: an example is the excitonic insulator ground state, which was recently predicted for [4]triangulene-based Kagome lattices[148].

The collective magnetic properties of triangulene-based crystals can be predicted by application of the Lieb's theorem, valid in the case of half-filling. A network with a symmetric unit cell (made up of two equal [n]triangulenes), thus with no sublattice imbalance, is expected to exhibit a $S = 0$ ground state and antiferromagnetic intermolecular interactions; on the contrary, unit cells composed of triangulenes of different sizes are predicted to give rise to long-range ferromagnetic or ferrimagnetic order[145].

Triangulene-based lattices could be ideal platforms for studying strongly correlated electronic phases and for investigating and manipulating metal-free magnetism in two dimensions[146]. However, their synthesis remains particularly challenging.

Ullmann-type intermolecular reactions have been successfully employed to fabricate one-dimensional triangulene-based nanostructures[138,144], but long-range polymerization in two dimensions is not straightforward. In general, it is limited by the irreversibility of covalent coupling reactions and by the absence of self-correction mechanisms, which lead to poor order and high defect density[21,149]. There are a few examples of successful growth of low-defect 2D covalent organic structures based on closed-shell triangulene units[150,151], but large-area networks composed of open-shell nanographenes have not yet been reported. The incorporation of radical units requires additional reaction steps (i.e., cyclodehydrogenation, dissociation of radical-protecting functional groups, etc.) which are expected to introduce further complexity into the 2D growth process.

Here we explore the possibility of growing these structures on metal substrates following different design concepts and strategies. We will consider three distinct molecular precursors (a pristine triangulene molecule and two aza-triangulene ones), designed for specific on-surface reaction processes aimed at generating radical units within extended covalent structures.[1]

5.2 Tri-brominated [3]triangulene precursor

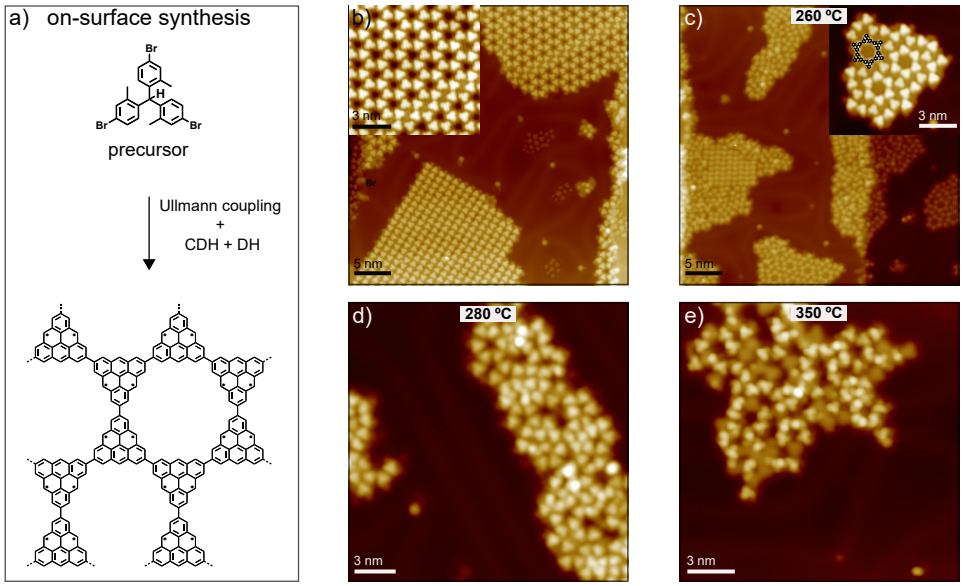

Figure 5.1: (a) On-surface reaction mechanism envisioned for generating a 2D covalent network starting with the tri-brominated triangulene precurso, consisting in Ullmann-like coupling and cyclodehydrogeantion (CDH) and dehydrogenation (DH) reactions. (b) Overview STM constant-current image recorded after depositing the precursor onto the Au(111) surface kept at room temperature. In the inset, STM image showing the spatial organization of the molecules inside the self-assembled domains. (c) STM image after annealing at 260°C; the inset highlights an island with some non-planar triangulenes arranged in six-membered rings. (d) STM image after annealing at 280°C, showing only disordered structures, and (e) after annealing at 350°C, displaying similar structures but with more planar regions. STM parameters: $V = 1$ V; $I = 5$ pA.

Our first approach involves the [3]triangulene precursor depicted in Figure 5.1a, containing three bromine substituents strategically incorporated at

[1] In-solution synthesis of the molecular precursors performed by Manuel Vilas-Varela, Diego Peña (CiQUS and Universidade de Santiago de Compostela, Santiago de Compostela, Spain).

the triangulene vertices. The halogen atoms are positioned in such a way to promote symmetric Ullmann-like polymerization in two dimensions. The intermolecular C-C coupling reaction, together with the cyclodehydrogenation of the three methyl groups in each triangulene, needed for the formation of the zigzag edges, is expected to lead to the generation of honeycomb networks, as illustrated in Figure 5.1a. This approach, therefore, represents the first and most immediate strategy to attempt an "extension" of the **TNS** (Chapter 4) into large-area 2D structures.

Following a procedure similar to that of the on-surface synthesis of the triangulene chains, we first sublimated the molecule on a Au(111) surface kept at room temperature and then annealed the sample to thermally activate the surface-assisted reactions. The deposition of the precursor, achieved through flash evaporation from a Si wafer, resulted in large self-assembled close-packed molecular domains, displaying both hexagonal and square-like symmetry, as depicted in the STM image in Figure 5.1b.

We then annealed the sample at progressively higher temperatures, starting at 260°C. At this step we already expect dehalogenation and subsequent C-C coupling on Au(111), while the cyclodehydrogenation reaction is generally activated around 300°C or above. As shown in Figure 5.1c, after the first annealing stage we can observe a spatial reorganization of the molecules inside the close-packed domains, but this leads only to partial intermolecular coupling, which results in the formation of a few hexagonal rings with the expected corner-to-corner links (inset in the figure). The low yield of the polymerization reaction is likely due to the highly non-planar geometry of the precursor, caused by the presence of the three bulky methyl groups, that can increase the activation barrier for the intermolecular coupling[152].

We thus annealed to higher temperatures in order to induce the cyclodehydrogenation reaction and promote molecular planarization. However, the further heating only resulted in highly irregular structures which were generally still retaining three-dimensional features, as seen after annealing at 280°C and 350°C (Figures 5.1d-e, respectively).

We conclude that the bulky structure of the precursor and the interplay between the planarization and polymerization reactions limit the formation of extended covalent structures and hinder the generation of ordered intermolecular bonds in the desired honeycomb symmetry. It is therefore necessary to turn to less three-dimensional molecular precursors and consider different reaction pathways.

5.3 CH_2-substituted aza-triangulene precursor

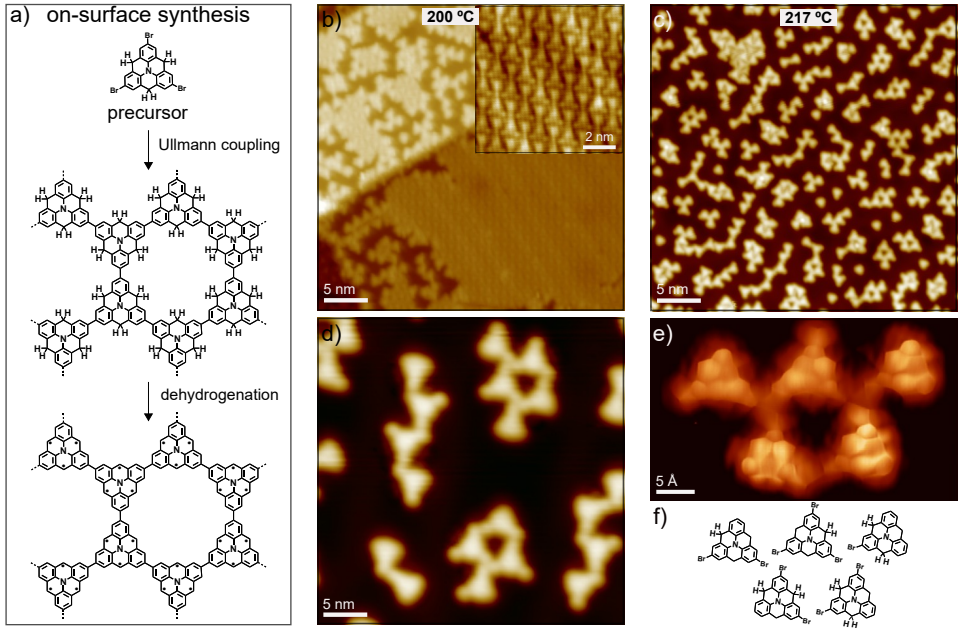

Figure 5.2: (a) Schematic representation of the on-surface reaction mechanism envisioned for growing 2D covalent structures starting with a CH_2-substituted aza-triangulene. (b) STM image ($V = 1$ V; $I = 30$ pA) recorded after deposition of the precursor on a Au(111) surface kept at $200°$C. Large self-assembled domains of brominated precursors can be observed, as highlighted in the close-up image in the inset. (c) Constant-current image ($V = 500$ mV; $I = 50$ pA) recorded after deposition on the Au(111) surface kept at $217°$C: small structures of non-covalently bonded molecules are observed; the image in (d) highlights a few of such structures ($V = 500$ mV; $I = 70$ pA). (e) Bond-resolved constant-height STM image ($V = 5$ mV) of a supramolecular structure composed of five triangulenes. (f) Tentative chemical model of the assembly in (e).

An alternative candidate for the generation of 2D networks is the precursor depicted in Figure 5.2, consisting in a tri-brominated aza-triangulene molecule substituted with methylene groups at the zigzag edges. This precursor exhibits a less three-dimensional structure; also, in this case the envisioned reaction mechanism involves thermally activated Ullmann coupling followed by dehydrogenation. The second reaction step can be induced either by annealing at higher temperature or via tip-induced reactions, thus allowing, in principle, to selectively generate radicals inside the covalent network.

Instead of first sublimating the molecule and then annealing the sample, now we deposited the precursor directly on a hot Au surface, with the aim of

enhancing surface diffusion and favour intermolecular coupling[151]. We started by depositing on the substrate kept at 200°C. As shown in Figure 5.2b, after annealing to this temperature only self-assembled domains are observed, as the precursors still retain their bromine atoms, appearing as rounded lobes at the triangulene corners (see the inset of Figure 5.2b).

Deposition at 217°C (Figure 5.2c) results in a different outcome, mostly small aggregates of molecules with several geometries. The close-up STM image in 5.2d, highlighting a few of such structures, shows that at this stage the triangulenes are non-covalently bonded. The bromine atoms, in fact, are still visible in most molecules, suggesting that these structures correspond to supramolecular assemblies, stabilized by electrostatic interactions. This interpretation is supported by the STM bond-resolved image of a structure made up of five triangulenes (Figure 5.2e), which clearly demonstrates the absence of intermolecular covalent coupling. Considering the relative orientation of the Br atoms inferred from the STM image (and represented in the chemical model in Figure 5.2f), it is likely that the molecules are held together by Br···Br halogen bonds, or Br···H electrostatic interactions established between a Br atom of one triangulene and an edge H atom close to the corner of a neighbouring one[153].

It is worth mentioning also that at this temperature some H atoms are already removed from the methylene groups, as a few carbon rings in the triangulenes appear smaller and less sharp compared with those containing hydrogenated sp^3-hybridized carbons, as seen in Figure 5.2e and indicated in the model in Figure 5.2f.

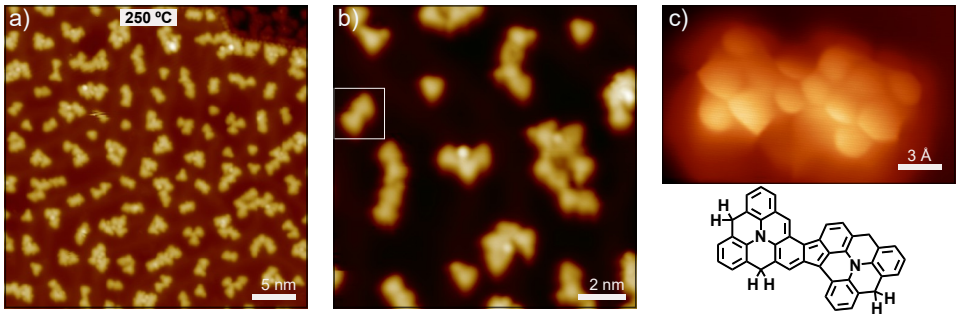

Figure 5.3: (a) STM image ($V = 1$ V; $I = 30$ pA) of the sample after deposition of the same precursor on the Au surface kept at 250°C. At this temperature, we obtain small covalent structures, made up of only a few units, as shown in the image in (b). (c) Bond-resolved constant-height STM image ($V = 5$ mV) of the triangulene dimer marked by the white box in (b) and tentative chemical model, showing the formation of a lateral bond.

Covalent coupling between the molecular units was only achieved when depositing on a substrate heated at 250°C (Figure 5.3), although resulting in small and irregular structures. A close-up image to some of these products is shown in Figure 5.3b, which displays also a few isolated aza-triangulene monomers. We focused on the dimer marked by the white box, in which two triangulenes are apparently fused laterally, and performed bond-resolved STM (Figure 5.3c) in order to determine its exact structure. We observe that covalent bonds have been formed between a de-brominated vertex of one triangulene and the center of a zigzag edge of the other, in the position initially hosting a methylene group. This outcome is likely due to a competition between the dehalogenation and dehydrogenation reactions, which are activated at similar energies, thus promoting irregular intermolecular links in lateral positions, instead of the targeted corner-to-corner bonds. Therefore, strategies to kinetically decouple the two reactions are needed, in order to achieve regular structures with the desired coupling geometry.

For this purpose, we first explored the possibility of activating the same reaction steps on a different substrate, Ag(111), with the idea of employing organometallic intermediates as templates for the generation of regular covalent networks. It is known, in fact, that extended and ordered metal-organic structures, involving carbon-metal-carbon bonds, are easily formed on this substrate, while they are more rarely observed on Au, due to the lower stability of the C-Au bond[154–157].

Indeed, deposition of the precursor onto the substrate kept at room temperature gave rise directly to the formation of large honeycomb-like organometallic networks, as illustrated in Figure 5.4a. This was possible since partial debromination takes place already at room temperature on Ag(111), as reported in previous works[157,158]. The same structures then persisted after heating the sample to 200°C (Figure 5.4b), without significant modifications.

The metal-organic nature of the networks obtained on Ag(111) is evident in the close-up STM image of the hexagonal structures reported in Figure 5.4c. We can clearly observe, in fact, that the intermolecular bonds between the triangulene units are mediated by Ag adatoms, appearing in the STM images as circular bright lobes (indicated by arrows in the figure)[159]. This interaction results in a center-to-center distance between the triangulenes of around 1.15 nm. Additionally, small round-shaped features are observed near the molecular edges, which can be tentatively attributed to the detached bromine atoms. It is worth noting the relatively good degree of structural order of the network. This is more commonly achieved in organometallic systems, compared to covalent structures, due to the reversibility of the metal-organic bonds, which leads to structural rearrangement and error correction processes[155].

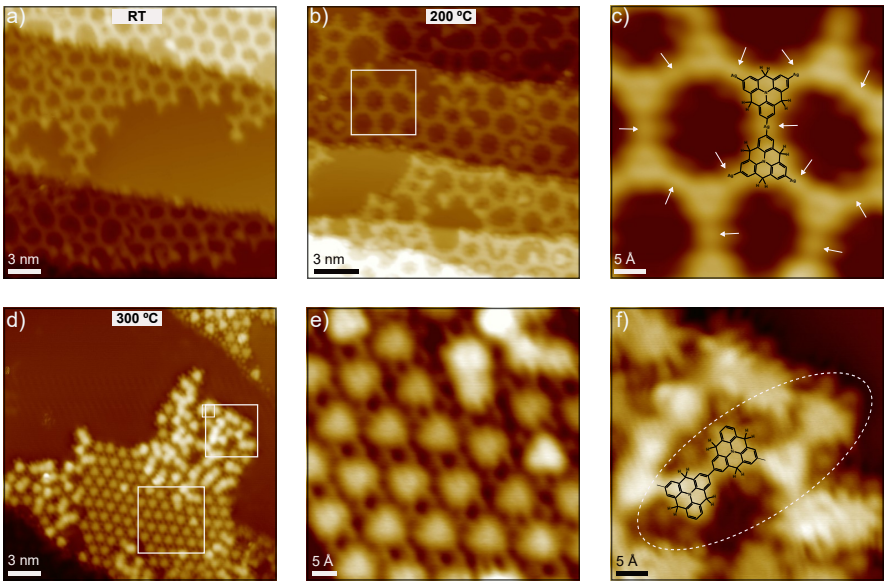

Figure 5.4: (a) STM image ($V = 1$ V; $I = 20$ pA) recorded after deposition of the CH_2-substituted aza-triangulene precursor on the Ag(111) surface kept at room temperature, showing the direct formation of metal-organic coordination networks. (b) STM image ($V = 1$ V; $I = 100$ pA) after annealing the sample at 200°C, displaying the same networks without structural modifications. (c) Close-up image of the area marked by the box in (b). We can clearly observe that the intermolecular links are mediated by Ag adatoms, appearing as protrusions in the middle of the bonds (as indicated by the arrows). (d) STM image ($V = 1$ V; $I = 30$ pA) recorded after annealing at 300°C, showing the conversion of the metal-organic networks into different structures. (e) Close-up image of an ordered assembly of non-bonded triangulenes, surrounded by bromine atoms. (f) Close-up image of the area in (d) containing a small chain of molecules linked through corner-to-corner covalent bonds.

We progressively increased the annealing temperature, without observing changes in the metal-organic complexes. Annealing at 300°C finally resulted in the disruption of the coordination networks and the appearance of different structures, as depicted in the overview image in Figure 5.4d. Two distinct phases were found, as highlighted in the close-up images in Figures 5.4e-f.

In some regions we observe ordered assemblies of non-coupled monomers, surrounded by features which appear to be bromine atoms. This is possible considering that bromine persists on the Ag surface until higher temperatures, with desorption starting only at around 400°C[158]. Nevertheless, small structures made up of coupled triangulenes can be found in other areas. An example is the chain highlighted in Figure 5.4f. Now, the evident lack of Ag adatoms within the intermolecular links suggests the formation of covalent bonds. This is confirmed also by the smaller center-to-center distance mea-

sured between neighbouring molecules (around 8.60 Å), compared with that observed in the metal-organic network (1.15 nm). It is important to point out that these covalent bonds are formed in the expected geometry, i.e., between the debrominated triangulene corners, unlike the irregular ones obtained on Au (Figure 5.3). They generate, however, only disordered and small-area structures.

We conclude that the conversion of the honeycomb metal-organic complexes formed on Ag(111) into covalent structures results in the loss of the initial structural order and geometry; therefore, this approach does not appear suitable for the formation of large and regular networks.

5.4 Ketone-substituted aza-triangulene precursor

A promising strategy for overcoming these issues is based the ketone-substituted precursor depicted in Figure 5.5a. It was already reported that the deposition of this molecule on a pre-heated Au surface can lead to the formation of ordered 2D covalent networks[151]. This is due in particular to the molecular structure, containing carbonyl groups that ensure a more planar and rigid geometry compared to the previous precursors, thus improving π-conjugation.

In addition, it was recently demonstrated that the open-shell aza-[3]triangulene monomer can be successfully generated on metal substrates from a ketone-substituted precursor[38]. The first step of the on-surface synthesis consists in exposure to atomic hydrogen followed by annealing, which results in partial or total deoxygenation of the precursor. After oxygen detachment, CH_2 groups are generally observed at the zigzag edges. Subsequently, the extra H atoms are removed via tip-induced reactions or annealing to obtain the open-shell aza[3]triangulene.

We explored therefore the possibility of growing radical-hosting networks combining these two results, i.e., following the reaction procedure illustrated in Figure 5.5a: i) formation of the 2D structures by thermally induced Ullmann-coupling; ii) exposure to atomic H and iii) further annealing and/or tip manipulation for generating radical units. The possibility of creating radicals via hydrogenation after the formation of the 2D polymer appears as a viable route to avoid competing reactions activated through annealing, like those needed for the precursors described earlier.

We deposited the precursor directly onto a hot Au(111) surface kept at 325°C, with the aim of directly promoting the Ullmann coupling reaction. As shown in the STM image in Figure 5.5b, the surface-assisted reaction resulted indeed in the formation of honeycomb-like networks. The image in Figure 5.5c clearly demonstrates the generation of covalent planar structures. We

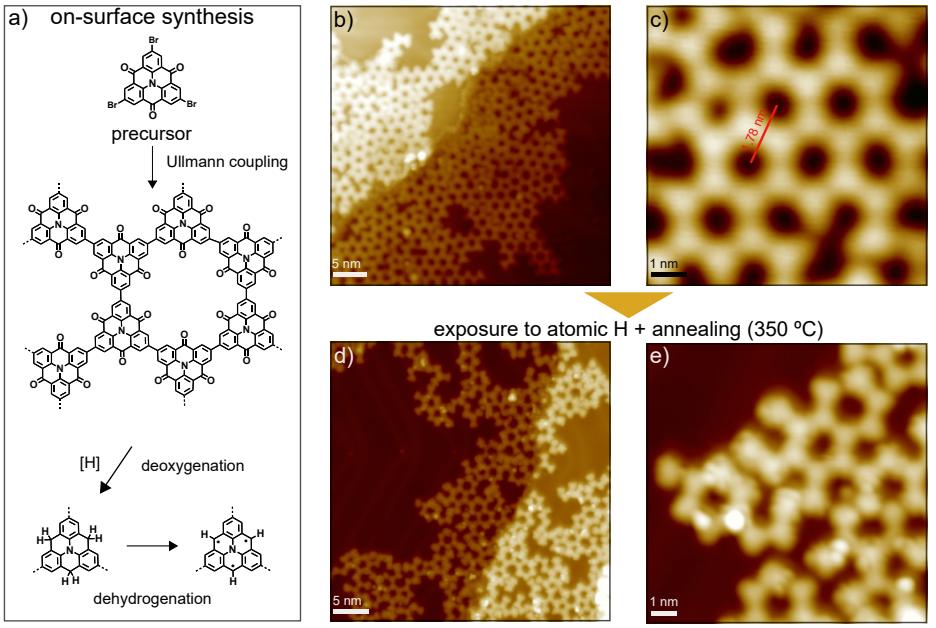

Figure 5.5: (a) Schematic representation of the on-surface synthesis strategy proposed for the generation of the aza-triangulene network. (b) STM image recorded after depositing the precursor onto a Au(111) surface kept at 325°C for 30 minutes. (c) STM image showing the covalently linked structures obtained after deposition on the hot substrate. (d-e) Constant-current images recorded, with a CO-functionalized tip, after exposing the sample to atomic H for 5 minutes, following the procedure described in the text, and subsequent annealing at 350°C. We can observe now a more irregular network, containing several three-dimensional features, due to the generation of sp^3 carbons. STM parameters: $V = 1$ V; $I = 30$ pA.

can observe the expected six-membered macrocycles, with center-to-center distances of around 1.78 nm, in agreement with previous reports[151], but also some defects in the honeycomb lattice and rings with a different number of triangulene units.

The following step is the deoxygenation of the networks. This is achieved by exposing the sample to a flux of atomic hydrogen originated by thermally splitting molecular hydrogen through a tungsten tube heated by electron bombardment[160]. From previous experiments on the individual aza[3]triangulenes, it is known that the hydrogenation generates several sp^3-hybridized carbons inside the molecules and therefore a subsequent annealing is needed to recover the planar structures[38].

We filled the preparation chamber with molecular hydrogen to a pressure of 1.0×10^{-7} mbar, and applied 40 W of heating power to the tungsten capillary (reaching a temperature $T = 2400$ K). The sample, kept at room temperature,

was placed in front of the H source for 5 minutes and subsequently annealed at 350°C. The STM images in Figures 5.5d-e, recorded after this process, show a significant reduction in the overall structural order of the network, due to the breaking of C-C bonds between the triangulenes. Additionally, several non-planar regions, appearing as brighter lobes, and likely due to the presence of sp^3 carbons, persist after the post-annealing at the relatively high temperature of 350°C.

Different parameters were tuned, such as the H_2 pressure, the exposure time or the heating power of the cracking source. We always observed some disruption of the C-C bonds inside the covalent networks, although the degree of disorder could be reduced using lower heating power. An example is shown in Figure 5.6, which demonstrates the generation of a few segments with the targeted open-shell structures in certain areas.

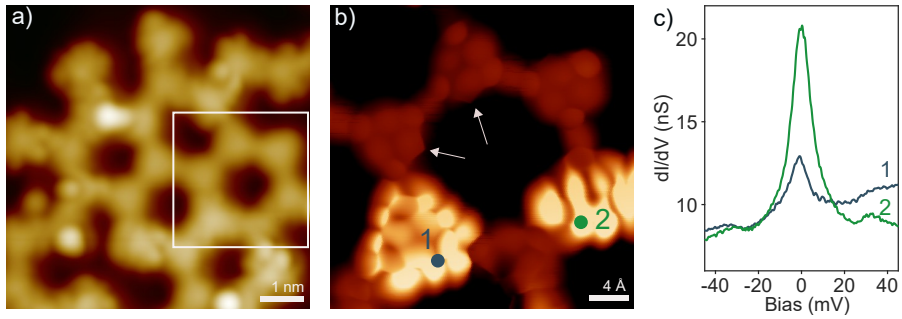

Figure 5.6: (a) STM constant-current image ($V = 1$ V; $I = 30$ pA) of an area of the network after hydrogenation and subsequent annealing. The image was recorded with a CO-terminated tip. (b) Bond-resolved constant-height current image ($V = 5$ mV) of the planar six-membered ring highlighted in the white box in (a). The two arrows indicate possible sites containing hydrogenated sp^3 carbons. (c) dI/dV spectra measured on the bright regions of the bond-resolved image in (b), at the positions indicated by the corresponding circles. The presence of Kondo resonances suggests the existence of localized radical units. Spectroscopy parameters: $V = 50$ mV, $I_{set} = 500$ pA, $V_{mod} = 2$ mV.

Although most triangulenes in the network display three dimensional features, we could identify a few planar units, like those in the macrocycle highlighted in Figure 5.6a. Here, we performed bond-resolved STM with a CO-functionalized tip, recording the low-bias ($V = 5$ meV) constant-height image reported in Figure 5.6b. The increase in the current signal detected in two units suggests the presence of localized radical states. In particular, the triangulene labeled as **1** displays a structure that can be attributed to an aza[3]triangulene after full deoxygenation and removal of the additional H atoms (the expected final product shown in the reaction scheme in Fig-

ure 5.5a). This molecule is supposed to have a S=1 ground state on Au(111), after the electron transfer to the surface[38]. This is compatible with the weak Kondo resonance detected in STS (Figure 5.5c). Bright features are also observed on the unit on the right (labeled as **2**). They make it difficult to resolve the molecular backbone, thereby hindering the determination of the exact chemical structure. The dI/dV spectrum recorded here displays a Kondo peak with a higher intensity than on **1**, suggesting the presence of a localized $S = 1/2$ radical unit.

The remaining planar triangulenes mostly retain their initial carbonyl groups. It is not straightforward to distinguish these units from CH_2 groups. However, in bond-resolved STM, rings containing hydrogenated sp^3 carbons generally appear larger and more elongated, as those indicated by the arrows in Figure 5.6b. Therefore, it is possible that in a few sites, the deoxygenation reaction has occurred but the additional H atoms in the resulting CH_2 groups have not been detached during the subsequent annealing.

Overall, this reaction pathway can generate localized radical states, but the main limitation is represented by the difficulty of achieving efficient and spatially homogeneous deoxygenation without inducing structural disorder into the network. These issues significantly reduce the possibility of generating large-area ordered structures containing multiple interacting radical units.

5.5 Conclusions

In this chapter we have described a few on-surface synthesis strategies aimed at generating radical-hosting 2D organic nanostructures. By exploring different molecular precursors and reaction pathways, we have found two conditions needed to achieve extended and ordered covalent networks: the use of structurally rigid and planar molecules, necessary for enhancing the intermolecular Ullmann-like reaction; and the decoupling of the different steps of the on-surface synthesis, required for avoiding the formation of irregular structures.

In particular, we have pointed out that the competition between Ullmann coupling and (cyclo)dehydrogenation, the most common reactions involved in the fabrication of nanographenes, can easily lead to the formation of irregular intermolecular links during the 2D growth process. For instance, this was clearly observed for the methylene-substituted precursor presented in Figure 5.2. In this case, a possible solution could be the replacement of the bromine substituents with different halogen atoms, like iodine. It is known, in fact, that cleavage of the C-I bond is achieved on Au(111) already at room temperature[161,162]. This would, in principle, enable activation of the Ullmann-like coupling via mild heating: in such a way, this reaction would be kinetically

decoupled from the dehydrogeneration needed to generate the radicals, thus avoiding the lateral fusion and irregular coupling observed when employing the brominated precursors.

Another possibility is to explore hierarchical approaches for the growth of ordered 2D networks[163,164]. Two different halogens with distinct activation temperatures (e.g., I and Br) can be, in fact, strategically incorporated in the triangulene precursors in order to first direct the Ullmann coupling towards the formation of 1D chains, and subsequently interlink these structures laterally to form 2D structures[150].

Among the different approaches presented here, the best results in the generation of 2D covalent networks were achieved using the ketone-substituted triangulene precursor illustrated in Figure 5.5. The deposition of this molecule on a hot Au substrate resulted in large-area structures with good long-range order. This was possible thanks to the structural rigidity of the molecule and to the lack of competing thermally activated reactions. The presence of carbonyl substituent groups on the triangulene edges, in fact, helped confining the Ullmann reaction to the desired corner-to-corner geometry, thus hindering the formation of irregular bonds. However, the subsequent removal of oxygen via atomic hydrogen dosing mostly resulted in the breaking of the C-C bonds between triangulenes. These results show that deoxygenation of carbonyl groups represents a promising route, alternative to the dehydrogenation of methyl or methylene groups, for generating radical units in organic nanostructures. However, further investigation and optimization of the hydrogenation process are necessary in order to efficiently and safely scale up this method for the fabrication of extended covalent structures.

6 Conclusions

In this thesis we investigated the magnetic properties of atomically precise carbon-based nanostructures fabricated on metal substrates through on-surface synthesis techniques. Using low-temperature scanning probe microscopy and spectroscopy, and supported by theoretical simulations, we explored spin interactions within all-organic molecular architectures with varying numbers of unpaired π electrons: a diradical molecule, derivative of the Chichibabin's hydrocarbon (**2-OS**), a triradical aza-nanographene (**TTAT**), and a triangulene-based macrocycle (**TNS**) hosting twelve unpaired electrons. For each of these molecular systems, the emergence of intramolecular magnetic interactions was revealed by characteristic spectroscopic fingerprints like Kondo resonances or inelastic spin excitations. We demonstrated that the spin state of these systems is influenced by the precise molecular structure, and investigated how their properties can be tuned through chemical or mechanical manipulation. Finally, we explored potential strategies for the on-surface synthesis of two-dimensional covalent networks based on spin-hosting triangulene units.

First, we studied the **2-OS** diradical, a non-planar organic molecule featuring non-benzenoid moieties. We demonstrated that it retains an open-shell state on an Au(111) surface, specifically a singlet ground state resulting from the partial molecular planarization induced by the substrate. Interestingly, we showed that the spin exchange interaction in this molecule can be tuned by controlled mechanical manipulation, highlighting the influence of the structural conformation on the spin states of molecular systems. This was demonstrated by using the STM tip to apply local attractive forces and modify the arrangement of the molecular moieties, as well as by directly contacting the molecule to partially lift it from the substrate. Specifically, we observed that the spin coupling became weaker in more orthogonal conformations, and that the original antiferromagnetic spin interaction could be recovered upon bringing the molecule back to a more planar arrangement. We also studied a shorter **2-OS** analogue, with a reduced distance between the radical units, showing that such modification in the chemical structure results in a transi-

tion from an open-shell to a closed-shell singlet state. The capability to tune the spin coupling by means of mechanical or chemical modifications provides new possibilities for the design of molecular architectures with customized and adjustable magnetic properties.

Next, we investigated a triradical aza-nanographene (**TTAT**), synthesized by coupling pristine and nitrogen-doped [3]triangulene building blocks along their zigzag edges. We demonstrated that the three unpaired π electrons hosted by the system interact ferromagnetically, resulting in a high-spin ($S = 3/2$) ground state. This was revealed by the appearance in STS of characteristic spectral features, both an underscreened Kondo resonance and inelastic spin excitations. Supported by advanced multiconfiguational calculations, we concluded that the spin state of the molecule is compatible with a Heisenberg ferromagnetic spin trimer.

Following a different covalent coupling strategy, we also studied a ring architecture formed by six [3]triangulenes bonded through their vertices (**TNS**, triangulene-based nanostar). Through inelastic electron tunneling spectroscopy, we observed collective spin excitations from a global singlet ground state to several many-body triplet states. The multi-step spin excitation pattern found by STS was rationalized by applying the Heisenberg spin model to a ring of six $S = 1$ spin units. Furthermore, we showed that the spin state of the system can be drastically modified by opening the cyclic structure (resulting in open-ended triangulene chains) or by passivating radical units. This offers important insights into the effect of topological modifications or local structural changes on the spin properties of molecular nanoarchitectures.

The generation and characterization of such multi-radical systems demonstrate the potential of triangulene-based nanostructures as platforms for investigating π magnetism and testing quantum models of spin interactions. A natural next step is to employ open-shell triangulenes as building blocks for fabricating extended two-dimensional structures. However, as we discussed in the final chapter, significant obstacles remain in achieving fully ordered two-dimensional networks with unpaired π electrons. The reactions required to incorporate radical units into organic networks add additional complexity to the already challenging process of 2D growth. Future work is needed to further explore and optimize some promising approaches described here, such as the deoxygenation of ketone-substituted precursors via hydrogen dosing.

Overall, the results presented in this thesis provide new insights into the design of molecular architectures with tailored magnetic properties. We have demonstrated that these structures represent ideal model systems for investigating magnetic interactions at the nanoscale. Moreover, the possibility to manipulate their spin states through various methods opens up significant

prospects for the future application of carbon-based systems in quantum technologies.

Acknowledgements

Completing this work and writing this thesis wouldn't have been possible without the help of many people who have accompanied me throughout this long journey. First of all, I want to thank Nacho, for giving me the opportunity to work in his group on such interesting topics, and for his guidance and support over the years. His insights, feedback, and constant encouragement have been essential in achieving all these results. A special thanks goes to the people I've had the pleasure of working with in my lab, Milano, especially Jeremy, Niklas, Fran, and Fabian, for their kind help and everything I've learned from each of them. I'm also grateful to the rest of the group for their support, advice, and for creating such a nice atmosphere over all these years: Alfonso, Andrea, Stefano, Katerina, Leo, Danilo, Dongfei, Jon, Georg and everyone else I've shared this experience with.

I'd also like to thank everyone from outside NanoGUNE I've worked with on various experiments, especially Tao and Martina from CFM, and Thomas, who joined me from Delft for some very nice measurements. I want to acknowledge all our collaborators, whose contributions have been essential. A special mention goes to theory groups, particularly to Thomas, Ricardo, Sofia, and Emilio, here in San Sebastián, and Pavel and his team in Prague. The discussions with all of them and their input were crucial in understanding the results of our experiments and shaping this work. Of course, none of this would have been possible without the very fruitful collaboration with the chemists from Diego's group.

Finally, I'd like to thank everyone who has supported me outside the lab, my friends, here and back in Italy, and especially my family for their constant help, patience, and encouragement, particularly during the more challenging times over these years.

Thanks to everyone!

Bibliography

[1] M. N. Baibich *et al.*, "Giant Magnetoresistance of (001)Fe/(001)Cr Magnetic Superlattices," *Phys. Rev. Lett.*, vol. 61, no. 21, pp. 2472–2475, Nov. 1988. DOI: 10.1103/PhysRevLett.61.2472.

[2] G. Binasch *et al.*, "Enhanced magnetoresistance in layered magnetic structures with antiferromagnetic interlayer exchange," *Phys. Rev. B*, vol. 39, no. 7, pp. 4828–4830, Mar. 1989. DOI: 10.1103/PhysRevB.39.4828.

[3] S. A. Wolf *et al.*, "Spintronics: A Spin-Based Electronics Vision for the Future," *Science*, vol. 294, no. 5546, pp. 1488–1495, Nov. 2001. DOI: 10.1126/science.1065389.

[4] S. D. Sarma, "Spintronics: Fundamentals and applications," *Rev. Mod. Phys.*, vol. 76, no. 2, 2004.

[5] S. Sanvito, "Molecular spintronics," *Chem. Soc. Rev.*, vol. 40, pp. 3336–3355, 6 2011. DOI: 10.1039/C1CS15047B.

[6] A. Gaita-Ariño *et al.*, "Molecular spins for quantum computation," *Nat. Chem.*, vol. 11, no. 4, pp. 301–309, Apr. 2019. DOI: 10.1038/s41557-019-0232-y.

[7] E. Coronado, "Molecular magnetism: From chemical design to spin control in molecules, materials and devices," *Nat. Rev. Mater.*, vol. 5, no. 2, pp. 87–104, Oct. 2019.

[8] W. J. M. Naber, S. Faez, and W. G. van der Wiel, "Organic spintronics," *J. Phys. D: Appl. Phys.*, vol. 40, no. 12, R205–R228, Jun. 2007. DOI: 10.1088/0022-3727/40/12/r01.

[9] K. S. Novoselov *et al.*, "Electric Field Effect in Atomically Thin Carbon Films," *Science*, vol. 306, no. 5696, pp. 666–669, Oct. 2004. DOI: 10.1126/science.1102896.

[10] A. K. Geim and K. S. Novoselov, "The rise of graphene," *Nat. Mater.*, vol. 6, no. 3, pp. 183–191, Mar. 2007. DOI: 10.1038/nmat1849.

[11] O. V. Yazyev, "Emergence of magnetism in graphene materials and nanostructures," *Rep. Prog. Phys.*, vol. 73, no. 5, p. 056 501, May 2010. DOI: 10.1088/0034-4885/73/5/056501.

[12] D. G. de Oteyza and T. Frederiksen, "Carbon-based nanostructures as a versatile platform for tunable π-magnetism," *J. Phys.: Condens. Matter*, vol. 34, p. 443 001, 2022.

[13] H. Min *et al.*, "Intrinsic and Rashba spin-orbit interactions in graphene sheets," *Phys. Rev. B*, vol. 74, no. 16, p. 165 310, Oct. 2006. DOI: 10.1103/PhysRevB.74.165310.

[14] O. V. Yazyev, "Hyperfine Interactions in Graphene and Related Carbon Nanostructures," *Nano Lett.*, vol. 8, no. 4, pp. 1011–1015, Apr. 2008. DOI: 10.1021/nl072667q.

[15] B. Trauzettel *et al.*, "Spin qubits in graphene quantum dots," *Nat. Phys.*, vol. 3, no. 3, pp. 192–196, Mar. 2007. DOI: 10.1038/nphys544.

[16] Y.-W. Son, M. L. Cohen, and S. G. Louie, "Half-metallic graphene nanoribbons," *Nature*, vol. 444, no. 7117, pp. 347–349, Nov. 2006. DOI: 10.1038/nature05180.

[17] W. Y. Kim and K. S. Kim, "Prediction of very large values of magnetoresistance in a graphene nanoribbon device," *Nat. Nanotechnol.*, vol. 3, no. 7, pp. 408–412, Jul. 2008. DOI: 10.1038/nnano.2008.163.

[18] M. Wimmer *et al.*, "Spin Currents in Rough Graphene Nanoribbons: Universal Fluctuations and Spin Injection," *Phys. Rev. Lett.*, vol. 100, no. 17, p. 177 207, May 2008. DOI: 10.1103/PhysRevLett.100.177207.

[19] T. Wang and J. Zhu, "Confined on-surface organic synthesis: Strategies and mechanisms," *Surf. Sci. Rep.*, vol. 74, no. 2, pp. 97–140, May 2019.

[20] S. Song *et al.*, "On-surface synthesis of graphene nanostructures with π-magnetism," *Chem. Soc. Rev.*, vol. 50, no. 5, pp. 3238–3262, 2021. DOI: 10.1039/D0CS01060J.

[21] S. Clair and D. G. De Oteyza, "Controlling a Chemical Coupling Reaction on a Surface: Tools and Strategies for On-Surface Synthesis," *Chem. Rev.*, vol. 119, no. 7, pp. 4717–4776, Apr. 2019. DOI: 10.1021/acs.chemrev.8b00601.

[22] N. Pavliček *et al.*, "Synthesis and characterization of triangulene," *Nat. Nanotechnol.*, vol. 12, no. 4, pp. 308–311, Apr. 2017, Number: 4 Publisher: Nature Publishing Group. DOI: 10.1038/nnano.2016.305.

[23] S. Mishra *et al.*, "Topological frustration induces unconventional magnetism in a nanographene," *Nat. Nanotechnol.*, vol. 15, no. 1, pp. 22–28, Jan. 2020. DOI: 10.1038/s41565-019-0577-9.

[24] P. Suvarnaphaet and S. Pechprasarn, "Graphene-Based Materials for Biosensors: A Review," *Sensors*, vol. 17, no. 10, 2017. DOI: 10.3390/s17102161.

[25] N. M. Peres, "Graphene, new physics in two dimensions," *Europhys. News*, vol. 40, no. 3, pp. 17–20, May 2009. DOI: 10.1051/epn/2009501.

[26] A. H. Castro Neto *et al.*, "The electronic properties of graphene," *Rev. Mod. Phys.*, vol. 81, no. 1, pp. 109–162, Jan. 2009. DOI: 10.1103/RevModPhys.81.109.

[27] S. Mishra *et al.*, "Collective all-carbon magnetism in triangulene dimers," *Angew. Chem. Int. Ed.*, vol. 59, no. 29, pp. 12 041–12 047, 2020. DOI: https://doi.org/10.1002/anie.202002687.

[28] E. H. Lieb, "Two theorems on the Hubbard model," *Phys. Rev. Lett.*, vol. 62, no. 10, pp. 1201–1204, Mar. 1989. DOI: 10.1103/PhysRevLett.62.1201.

[29] A. A. Ovchinnikov, "Multiplicity of the ground state of large alternant organic molecules with conjugated bonds: (Do Organic Ferromagnetics Exist?)" *Theor. Chim. Acta*, vol. 47, no. 4, pp. 297–304, 1978. DOI: 10.1007/BF00549259.

[30] M. M. Ugeda *et al.*, "Missing Atom as a Source of Carbon Magnetism," *Phys. Rev. Lett.*, vol. 104, no. 9, p. 096 804, Mar. 2010. DOI: 10.1103/PhysRevLett.104.096804.

[31] H. González-Herrero *et al.*, "Atomic-scale control of graphene magnetism by using hydrogen atoms," *Science*, vol. 352, no. 6284, pp. 437–441, Apr. 2016. DOI: 10.1126/science.aad8038.

[32] E. Clar, *The Aromatic Sextet* (A Wiley-Interscience publication). J. Wiley, 1972.

[33] M. Solà, "Forty years of Clar's aromatic π-sextet rule," *Front. Chem.*, vol. 1, 2013. DOI: 10.3389/fchem.2013.00022.

[34] S. Fajtlowicz, P. E. John, and H. Sachs, "On Maximum Matchings and Eigenvalues of Benzenoid Graphs," *Croat. Chem. Acta*, p. 7, 2005.

[35] X. Su *et al.*, "Atomically Precise Synthesis and Characterization of Heptauthrene with Triplet Ground State," *Nano Lett.*, vol. 20, no. 9, pp. 6859–6864, Sep. 2020. DOI: 10.1021/acs.nanolett.0c02939.

[36] S. Mishra *et al.*, "Synthesis and Characterization of π-Extended Triangulene," *J. Am. Chem. Soc.*, vol. 141, no. 27, pp. 10 621–10 625, Jul. 2019. DOI: 10.1021/jacs.9b05319.

[37] J. Su *et al.*, "Atomically precise bottom-up synthesis of π-extended [5]triangulene," *Sci. Adv.*, vol. 5, no. 7, eaav7717, 2019, Publisher: American Association for the Advancement of Science. DOI: 10.1126/sciadv.aav7717.

[38] T. Wang *et al.*, "Aza-Triangulene: On-Surface Synthesis and Electronic and Magnetic Properties," *J. Am. Chem. Soc.*, vol. 144, no. 10, pp. 4522–4529, Mar. 2022. DOI: 10.1021/jacs.1c12618.

[39] J. Lawrence *et al.*, "Topological design and synthesis of high-spin azatriangulenes without jahn–teller distortions," *ACS Nano*, pp. 20 237–20 245, 2023. DOI: 10.1021/acsnano.3c05974.

[40] E. Turco *et al.*, "Observation of the Magnetic Ground State of the Two Smallest Triangular Nanographenes," *JACS Au*, vol. 3, no. 5, pp. 1358–1364, 2023. DOI: 10.1021/jacsau.2c00666.

[41] D. Jacob and J. Fernández-Rossier, "Theory of intermolecular exchange in coupled spin-$\frac{1}{2}$ nanographenes," *Phys. Rev. B*, vol. 106, p. 205 405, 20 Nov. 2022. DOI: 10.1103/PhysRevB.106.205405.

[42] S. Mishra *et al.*, "Large magnetic exchange coupling in rhombus-shaped nanographenes with zigzag periphery," *Nat. Chem.*, vol. 13, no. 6, pp. 581–586, Jun. 2021. DOI: 10.1038/s41557-021-00678-2.

[43] K. Biswas *et al.*, "Steering Large Magnetic Exchange Coupling in Nanographenes near the Closed-Shell to Open-Shell Transition," *J. Am. Chem. Soc.*, vol. 145, no. 5, pp. 2968–2974, Feb. 2023, Publisher: American Chemical Society. DOI: 10.1021/jacs.2c11431.

[44] G. Binnig *et al.*, "Tunneling through a controllable vacuum gap," *Appl. Phys. Lett.*, vol. 40, no. 2, pp. 178–180, Jan. 1982. DOI: 10.1063/1.92999.

[45] G. Binnig *et al.*, "Surface Studies by Scanning Tunneling Microscopy," *Phys. Rev. Lett.*, vol. 49, no. 1, pp. 57–61, Jul. 1982. DOI: 10.1103/PhysRevLett.49.57.

[46] B. Voigtländer, *Scanning Probe Microscopy: Atomic Force Microscopy and Scanning Tunneling Microscopy* (NanoScience and Technology). Berlin, Heidelberg: Springer Berlin Heidelberg, 2015. DOI: 10.1007/978-3-662-45240-0.

[47] K. Bian *et al.*, "Scanning probe microscopy," *Nat. Rev. Methods Primers*, vol. 1, no. 1, p. 36, May 2021. DOI: 10.1038/s43586-021-00033-2.

[48] J. Bardeen, "Tunnelling from a many-particle point of view," *Phys. Rev. Lett.*, vol. 6, pp. 57–59, 2 Jan. 1961. DOI: 10.1103/PhysRevLett.6.57.

[49] J. Tersoff and D. R. Hamann, "Theory of the scanning tunneling microscope," *Phys. Rev. B*, vol. 31, pp. 805–813, 2 Jan. 1985. DOI: 10.1103/PhysRevB.31.805.

[50] G. Kichin *et al.*, "Single Molecule and Single Atom Sensors for Atomic Resolution Imaging of Chemically Complex Surfaces," *J. Am. Chem. Soc.*, vol. 133, no. 42, pp. 16 847–16 851, Oct. 2011. DOI: 10.1021/ja204624g.

[51] P. Hapala *et al.*, "Mechanism of high-resolution stm/afm imaging with functionalized tips," *Phys. Rev. B*, vol. 90, p. 085 421, 8 Aug. 2014. DOI: 10.1103/PhysRevB.90.085421.

[52] L. Gross *et al.*, "The Chemical Structure of a Molecule Resolved by Atomic Force Microscopy," *Science*, vol. 325, no. 5944, pp. 1110–1114, Aug. 28, 2009.

[53] F. J. Giessibl, "Advances in atomic force microscopy," *Rev. Mod. Phys.*, vol. 75, no. 3, 2003.

[54] B. Cirera *et al.*, "Tailoring topological order and π-conjugation to engineer quasi-metallic polymers," *Nat. Nanotechnol.*, vol. 15, no. 6, pp. 437–443, Jun. 2020. DOI: 10.1038/s41565-020-0668-7.

[55] K. Biswas *et al.*, "Interplay between π-conjugation and exchange magnetism in one-dimensional porphyrinoid polymers," *J. Am. Chem. Soc.*, vol. 144, no. 28, pp. 12 725–12 731, 2022, PMID: 35817408. DOI: 10.1021/jacs.2c02700.

[56] F. J. Giessibl, "High-speed force sensor for force microscopy and profilometry utilizing a quartz tuning fork," *Appl. Phys. Lett.*, vol. 73, no. 26, pp. 3956–3958, Dec. 28, 1998.

[57] J. Li *et al.*, "Uncovering the triplet ground state of triangular graphene nanoflakes engineered with atomic precision on a metal surface," *Phys. Rev. Lett.*, vol. 124, p. 177 201, 17 Apr. 2020. DOI: 10.1103/PhysRevLett.124.177201.

[58] J. Li *et al.*, "Single spin localization and manipulation in graphene open-shell nanostructures," *Nat. Commun.*, vol. 10, no. 1, p. 200, Jan. 2019. DOI: 10.1038/s41467-018-08060-6.

[59] L. Kouwenhoven and L. Glazman, "Revival of the Kondo effect," *Phys. World*, vol. 14, no. 1, p. 33, Jan. 2001. DOI: 10.1088/2058-7058/14/1/28.

[60] M. Ternes, A. J. Heinrich, and W.-D. Schneider, "Spectroscopic manifestations of the kondo effect on single adatoms," *J. Phys.: Condens. Matter*, vol. 21, no. 5, p. 053 001, Dec. 2008. DOI: 10.1088/0953-8984/21/5/053001.

[61] J. Kondo, "Resistance Minimum in Dilute Magnetic Alloys," *Progr. Theor. Phys.*, vol. 32, no. 1, pp. 37–49, Jul. 1964. DOI: 10.1143/PTP.32.37.

[62] P. W. Anderson, "Localized magnetic states in metals," *Phys. Rev.*, vol. 124, pp. 41–53, 1 Oct. 1961. DOI: 10.1103/PhysRev.124.41.

[63] H. O. Frota, "Shape of the kondo resonance," *Phys. Rev. B*, vol. 45, pp. 1096–1099, 3 Jan. 1992. DOI: 10.1103/PhysRevB.45.1096.

[64] M. Vilas-Varela *et al.*, "On-Surface Synthesis and Characterization of a High-Spin Aza-[5]-Triangulene," *Angew. Chem. Int. Ed.*, vol. 62, no. 41, e202307884, 2023. DOI: 10.1002/anie.202307884.

[65] B. C. Stipe, M. A. Rezaei, and W. Ho, "Single-Molecule Vibrational Spectroscopy and Microscopy," *Science*, vol. 280, no. 5370, pp. 1732–1735, Jun. 1998. DOI: 10.1126/science.280.5370.1732.

[66] A. J. Heinrich *et al.*, "Single-Atom Spin-Flip Spectroscopy," *Science*, vol. 306, no. 5695, pp. 466–469, Oct. 2004. DOI: 10.1126/science.1101077.

[67] C. F. Hirjibehedin, C. P. Lutz, and A. J. Heinrich, "Spin coupling in engineered atomic structures," *Science*, vol. 312, no. 5776, pp. 1021–1024, 2006. DOI: 10.1126/science.1125398.

[68] L. Grill *et al.*, "Nano-architectures by covalent assembly of molecular building blocks," *Nat. Nanotechnol.*, vol. 2, no. 11, pp. 687–691, Nov. 2007. DOI: 10.1038/nnano.2007.346.

[69] J. Cai *et al.*, "Atomically precise bottom-up fabrication of graphene nanoribbons," *Nature*, vol. 466, no. 7305, pp. 470–473, Jul. 2010. DOI: 10.1038/nature09211.

[70] P. Ruffieux *et al.*, "On-surface synthesis of graphene nanoribbons with zigzag edge topology," *Nature*, vol. 531, no. 7595, pp. 489–492, Mar. 2016. DOI: 10.1038/nature17151.

[71] D. G. de Oteyza *et al.*, "Substrate-Independent Growth of Atomically Precise Chiral Graphene Nanoribbons," *ACS Nano*, vol. 10, no. 9, pp. 9000–9008, Sep. 2016. DOI: 10.1021/acsnano.6b05269.

[72] I. Horcas *et al.*, "Wsxm: A software for scanning probe microscopy and a tool for nanotechnology," *Rev. Sci. Instrum.*, vol. 78, no. 1, p. 013 705, 2007. DOI: 10.1063/1.2432410.

[73] M. Ruby, "Spectrafox: A free open-source data management and analysis tool for scanning probe microscopy and spectroscopy," *SoftwareX*, vol. 5, pp. 31–36, 2016. DOI: https://doi.org/10.1016/j.softx.2016.04.001.

[74] T. R. Albrecht *et al.*, "Frequency modulation detection using high- Q cantilevers for enhanced force microscope sensitivity," *J. Appl. Phys.*, vol. 69, no. 2, pp. 668–673, Jan. 15, 1991.

[75] S. Das and J. Wu, "Polycyclic hydrocarbons with an open-shell ground state," *Phys. Sci. Rev.*, vol. 2, no. 5, May 2017. DOI: 10.1515/psr-2016-0109.

[76] A. Rajca, "Organic diradicals and polyradicals: From spin coupling to magnetism?" *Chem. Rev.*, vol. 94, no. 4, pp. 871–893, 1994. DOI: 10.1021/cr00028a002.

[77] F. Popp, F. Bickelhaupt, and C. Maclean, "The electronic structure of chichibabin's hydrocarbon," *Chem. Phys. Lett.*, vol. 55, no. 2, pp. 327–330, 1978. DOI: https://doi.org/10.1016/0009-2614(78)87030-4.

[78] L. K. Montgomery *et al.*, "The molecular structures of thiele's and chichibabin's hydrocarbons," *J. Am. Chem. Soc.*, vol. 108, no. 19, pp. 6004–6011, Sep. 1986.

[79] Z. Zeng *et al.*, "Stable tetrabenzo-chichibabin's hydrocarbons: Tunable ground state and unusual transition between their closed-shell and open-shell resonance forms," *J. Am. Chem. Soc.*, vol. 134, no. 35, pp. 14 513–14 525, 2012.

[80] T. Y. Baum *et al.*, "Magnetic fingerprints in an all-organic radical molecular break junction," *Nano Lett.*, vol. 22, no. 20, pp. 8086–8092, 2022. DOI: 10.1021/acs.nanolett.2c02326.

[81] L. Zuo *et al.*, "Unraveling the Nature of Spin Coupling in a Metal-Free Diradical: Theoretical Distinction of Ferromagnetic and Antiferromagnetic Interactions," *J. Phys. Chem. Lett.*, pp. 5761–5769, May 2024. DOI: 10.1021/acs.jpclett.4c01063.

[82] Z. Huang *et al.*, "A chemist's overview of surface electron spins," *Chem. Soc. Rev.*, vol. 46, pp. 1955–1976, 7 2017. DOI: 10.1039/C6CS00891G.

[83] T. Junghoefer *et al.*, "Challenges in controlled thermal deposition of organic diradicals," *Chem. Mater.*, vol. 33, no. 6, pp. 2019–2028, 2021. DOI: 10.1021/acs.chemmater.0c03880.

[84] F. Eisenhut *et al.*, "Dodecacene generated on surface: Reopening of the energy gap," *ACS Nano*, vol. 14, no. 1, pp. 1011–1017, 2020. DOI: 10.1021/acsnano.9b08456.

[85] M. Ternes, "Spin excitations and correlations in scanning tunneling spectroscopy," *New J. Phys.*, vol. 17, p. 063 016, Jun. 2015. DOI: 10.1088/1367-2630/17/6/063016.

[86] R. Ortiz and J. Fernández-Rossier, "Probing local moments in nanographenes with electron tunneling spectroscopy," *Progr. Surf. Sci.*, vol. 95, no. 4, p. 100 595, 2020. DOI: https://doi.org/10.1016/j.progsurf.2020.100595.

[87] J. Hieulle *et al.*, "From solution to surface: Persistence of the diradical character of a diindenoanthracene derivative on a metallic substrate," *J. Phys. Chem. Lett.*, vol. 14, no. 50, pp. 11 506–11 512, 2023. DOI: 10.1021/acs.jpclett.3c02401.

[88] S. Song *et al.*, "Highly entangled polyradical nanographene with coexisting strong correlation and topological frustration," *Nat. Chem.*, Feb. 2024. DOI: 10.1038/s41557-024-01453-9.

[89] J. Paaske *et al.*, "Non-equilibrium singlet–triplet kondo effect in carbon nanotubes," *Nat. Phys.*, vol. 2, no. 7, pp. 460–464, Jul. 2006. DOI: 10.1038/nphys340.

[90] S. Sanz Wuhl *et al.*, *Hubbard: V0.4.1*, 2023. DOI: 10.5281/zenodo.4748765.

[91] N. Papior, *Sisl: V0.14.4.dev46+g8754d4f5*, 2023. DOI: 10.5281/zenodo.597181.

[92] H. Rezaei and A. Phirouznia, "Modified spin-orbit couplings in uniaxially strained graphene," *Eur. Phys. J. B*, vol. 91, no. 11, p. 295, Nov. 2018.

[93] H. Yu and T. Heine, "Magnetic coupling control in triangulene dimers," *J. Am. Chem. Soc.*, vol. 145, no. 35, pp. 19 303–19 311, 2023. DOI: 10.1021/jacs.3c05178.

[94] B. W. Heinrich *et al.*, "Control of oxidation and spin state in a single-molecule junction," *ACS Nano*, vol. 12, no. 4, pp. 3172–3177, 2018. DOI: 10.1021/acsnano.8b00312.

[95] K. Vaxevani *et al.*, "Extending the spin excitation lifetime of a magnetic molecule on a proximitized superconductor," *Nano Lett.*, vol. 22, no. 15, pp. 6075–6082, 2022. DOI: 10.1021/acs.nanolett.2c00924.

[96] H. B. Heersche *et al.*, "Electron transport through single Mn_{12} molecular magnets," *Phys. Rev. Lett.*, vol. 96, p. 206 801, 20 May 2006. DOI: 10.1103/PhysRevLett.96.206801.

[97] S. Naghibi *et al.*, "Redox-addressable single-molecule junctions incorporating a persistent organic radical," *Angew. Chem. Int. Ed.*, vol. 61, no. 23, e202116985, 2022. DOI: https://doi.org/10.1002/anie.202116985.

[98] M. Lokamani *et al.*, "Stretch evolution of electronic coupling of the thiophenyl anchoring group with gold in mechanically controllable break junctions," *J. Phys. Chem. Lett.*, vol. 14, no. 24, pp. 5709–5717, 2023. DOI: 10.1021/acs.jpclett.3c00370.

[99] C. Rubio-Verdú *et al.*, "Orbital-selective spin excitation of a magnetic porphyrin," *Commun. phys.*, vol. 1, no. 1, p. 15, 2018. DOI: 10.1038/s42005-018-0015-6.

[100] M. Corso *et al.*, "Charge redistribution and transport in molecular contacts," *Phys. Rev. Lett.*, vol. 115, p. 136 101, 13 Sep. 2015. DOI: 10.1103/PhysRevLett.115.136101.

[101] L. Farinacci *et al.*, "Tuning the coupling of an individual magnetic impurity to a superconductor: Quantum phase transition and transport," *Phys. Rev. Lett.*, vol. 121, p. 196 803, 19 Nov. 2018. DOI: 10.1103/PhysRevLett.121.196803.

[102] S. Trivini *et al.*, "Cooper pair excitation mediated by a molecular quantum spin on a superconducting proximitized gold film," *Phys. Rev. Lett.*, vol. 130, p. 136 004, 13 Mar. 2023. DOI: 10.1103/PhysRevLett.130.136004.

[103] R. Temirov *et al.*, "Kondo effect by controlled cleavage of a single-molecule contact," *Nanotechnology*, vol. 19, no. 6, p. 065 401, Feb. 2008, ISBN: 0957-4484. DOI: 10.1088/0957-4484/19/6/065401.

[104] L. Lafferentz *et al.*, "Conductance of a Single Conjugated Polymer as a Continuous Function of Its Length," *Science*, vol. 323, no. 5918, pp. 1193–1197, Feb. 2009. DOI: 10.1126/science.1168255.

[105] N. Friedrich *et al.*, "Magnetism of Topological Boundary States Induced by Boron Substitution in Graphene Nanoribbons," *Phys. Rev. Lett.*, vol. 125, no. 14, p. 146 801, Sep. 2020. DOI: 10.1103/PhysRevLett.125.146801.

[106] T. Baum, "Electronic transport signatures of two-electron interactions in all-organic single-molecule junctions," Dissertation (TU Delft), Delft University of Technology, 2024. DOI: 10.4233/uuid:dd6db953-9fc5-4be8-99f7-28b2b9e3abd1.

[107] D. Xiang *et al.*, "Mechanically Controllable Break Junctions for Molecular Electronics," *Adv. Mater.*, vol. 25, no. 35, pp. 4845–4867, Sep. 2013. DOI: 10.1002/adma.201301589.

[108] P. Gehring, J. M. Thijssen, and H. S. J. Van Der Zant, "Single-molecule quantum-transport phenomena in break junctions," *Nat. Rev. Phys.*, vol. 1, no. 6, pp. 381–396, May 2019. DOI: 10.1038/s42254-019-0055-1.

[109] R. H. M. Smit *et al.*, "Measurement of the conductance of a hydrogen molecule," *Nature*, vol. 419, no. 6910, pp. 906–909, Oct. 2002. DOI: 10.1038/nature01103.

[110] W. Haiss *et al.*, "Impact of Junction Formation Method and Surface Roughness on Single Molecule Conductance," *The J. Phys. Chem. C*, vol. 113, no. 14, pp. 5823–5833, Apr. 2009. DOI: 10.1021/jp811142d.

[111] F. Van Veen *et al.*, "A generalized neural network approach for separation of molecular breaking traces," *J. Mater. Chem. C*, vol. 11, no. 44, pp. 15 564–15 570, 2023. DOI: 10.1039/D3TC02346J.

[112] Y. Zheng *et al.*, "Designer spin order in diradical nanographenes," *Nat. Commun.*, vol. 11, no. 1, p. 6076, Dec. 2020. DOI: 10.1038/s41467-020-19834-2.

[113] A. Sánchez-Grande *et al.*, "Diradical organic one-dimensional polymers synthesized on a metallic surface," *Angew. Chem. Int. Ed.*, vol. 59, no. 40, pp. 17 594–17 599, 2020. eprint: https://onlinelibrary.wiley.com/doi/pdf/10.1002/anie.202006276.

[114] J. C. Slater and G. F. Koster, "Simplified LCAO method for the periodic potential problem," *Phys. Rev.*, vol. 94, no. 6, pp. 1498–1524, 1954.

[115] J. M. Soler *et al.*, "The SIESTA method for ab initio order-N materials simulation," *J. Phys.: Condens. Matter*, vol. 14, no. 11, pp. 2745–2779, 2002. DOI: 10.1088/0953-8984/14/11/302.

[116] M. J. Frisch *et al.*, *Gaussian~16 Revision C.01*, Gaussian Inc. Wallingford CT, 2016.

[117] J. W. Ochterski, "Thermochemistry in gaussian," *Gaussian Inc*, vol. 1, pp. 1–19, 2000.

[118] J. P. Perdew, K. Burke, and M. Ernzerhof, "Generalized gradient approximation made simple," *Phys. Rev. Lett.*, vol. 77, no. 18, pp. 3865–3868, 1996.

[119] W. J. Hehre, R. F. Stewart, and J. A. Pople, "Self-consistent molecular-orbital methods. i. use of gaussian expansions of slater-type atomic orbitals," *J. Chem. Phys.*, vol. 51, no. 6, pp. 2657–2664, 1969.

[120] J. B. Collins *et al.*, "Self-consistent molecular orbital methods. xvii. geometries and binding energies of second-row molecules. a comparison of three basis sets," *J. Chem. Phys.*, vol. 64, no. 12, pp. 5142–5151, 1976.

[121] S. Cheng *et al.*, "On-surface synthesis of triangulene trimers via dehydration reaction," *Nat. Commun.*, vol. 13, no. 1, p. 1705, Mar. 2022. DOI: 10.1038/s41467-022-29371-9.

[122] Q. Du *et al.*, "Orbital-symmetry effects on magnetic exchange in open-shell nanographenes," *Nat. Commun.*, vol. 14, no. 1, p. 4802, Aug. 2023. DOI: 10.1038/s41467-023-40542-0.

[123] E. Turco *et al.*, *Magnetic excitations in ferromagnetically coupled spin-1 nanographenes*, 2024. arXiv: 2407.00728 [cond-mat.mes-hall].

[124] J. P. Calupitan *et al.*, "Emergence of π-Magnetism in Fused Aza-Triangulenes: Symmetry and Charge Transfer Effects," *Nano Lett.*, vol. 23, no. 21, pp. 9832–9840, 2023. DOI: 10.1021/acs.nanolett.3c02586.

[125] B. de la Torre *et al.*, "Submolecular Resolution by Variation of the Inelastic Electron Tunneling Spectroscopy Amplitude and its Relation to the AFM/STM Signal," *Phys. Rev. Lett.*, vol. 119, no. 16, p. 166 001, Oct. 2017. DOI: 10.1103/PhysRevLett.119.166001.

[126] N. Krane *et al.*, "Exchange Interactions and Intermolecular Hybridization in a Spin-1/2 Nanographene Dimer," *Nano Lett.*, vol. 23, no. 20, pp. 9353–9359, 2023. DOI: 10.1021/acs.nanolett.3c02633.

[127] M. E. Sandoval-Salinas, A. Carreras, and D. Casanova, "Triangular graphene nanofragments: Open-shell character and doping," *Phys. Chem. Chem. Phys.*, vol. 21, no. 18, pp. 9069–9076, 2019. DOI: 10.1039/C9CP00641A.

[128] J. V. Ortiz, "Dyson-orbital concepts for description of electrons in molecules," *J. Chem. Phys.*, vol. 153, no. 7, p. 070 902, Aug. 21, 2020. DOI: 10.1063/5.0016472.

[129] O. Krej čí *et al.*, "Principles and simulations of high-resolution stm imaging with a flexible tip apex," *Phys. Rev. B*, vol. 95, p. 045 407, 4 Jan. 2017. DOI: 10.1103/PhysRevB.95.045407.

[130] L. Gross *et al.*, "Measuring the Charge State of an Adatom with Noncontact Atomic Force Microscopy," *Science*, vol. 324, no. 5933, pp. 1428–1431, Jun. 2009. DOI: 10.1126/science.1172273.

[131] Y. Gao *et al.*, "On-surface synthesis of a doubly anti-aromatic carbon allotrope," *Nature*, vol. 623, no. 7989, pp. 977–981, Nov. 2023. DOI: 10.1038/s41586-023-06566-8.

[132] A. Calvo-Fernández *et al.*, *Theoretical model for multi-orbital Kondo screening in strongly correlated molecules with several unpaired electrons*, arXiv:2405.15958 [cond-mat], May 2024.

[133] S. Mishra *et al.*, "Nonbenzenoid High-Spin Polycyclic Hydrocarbons Generated by Atom Manipulation," *ACS Nano*, vol. 16, no. 2, pp. 3264–3271, 2022. DOI: 10.1021/acsnano.1c11157.

[134] A. I. Krylov, "Triradicals," *J. Phys. Chem. A*, vol. 109, no. 47, pp. 10 638–10 645, Dec. 1, 2005. DOI: 10.1021/jp0528212.

[135] J. T. Haraldsen, T. Barnes, and J. L. Musfeldt, "Neutron Scattering and Magnetic Observables for S = 1/2 Molecular Magnets," *Phys. Rev. B*, vol. 71, no. 6, p. 064 403, Feb. 2005, arXiv:cond-mat/0408253. DOI: 10.1103/PhysRevB.71.064403.

[136] R. L. Martin, "Natural transition orbitals," *J. Chem. Phys.*, vol. 118, no. 11, pp. 4775–4777, Mar. 2003.

[137] S. Mishra *et al.*, "Synthesis and characterization of [7]triangulene," *Nanoscale*, vol. 13, no. 3, pp. 1624–1628, 2021. DOI: 10.1039/D0NR08181G.

[138] S. Mishra *et al.*, "Observation of fractional edge excitations in nanographene spin chains," *Nature*, vol. 598, no. 7880, pp. 287–292, Oct. 2021, arXiv: 2105.09102. DOI: 10.1038/s41586-021-03842-3.

[139] F. D. M. Haldane, "Nonlinear Field Theory of Large-Spin Heisenberg Antiferromagnets: Semiclassically Quantized Solitons of the One-Dimensional Easy-Axis Néel State," *Phys. Rev. Lett.*, vol. 50, no. 15, pp. 1153–1156, Apr. 1983. DOI: 10.1103/PhysRevLett.50.1153.

[140] I. Affleck *et al.*, "Rigorous results on valence-bond ground states in antiferromagnets," *Phys. Rev. Lett.*, vol. 59, no. 7, pp. 799–802, Aug. 1987. DOI: 10.1103/PhysRevLett.59.799.

[141] T. Kennedy, "Exact diagonalisations of open spin-1 chains," *J. Phys. Condens. Matter*, vol. 2, no. 26, pp. 5737–5745, Jul. 1990. DOI: 10.1088/0953-8984/2/26/010.

[142] A. Spinelli *et al.*, "Imaging of spin waves in atomically designed nanomagnets," *Nat. Mater.*, vol. 13, no. 8, pp. 782–785, Aug. 2014. DOI: 10.1038/nmat4018.

[143] A. Sánchez-Grande *et al.*, "Unravelling the Open-Shell Character of Peripentacene on Au(111)," *J. Phys. Chem. Lett.*, vol. 12, no. 1, pp. 330–336, Jan. 2021. DOI: 10.1021/acs.jpclett.0c02518.

[144] C. Zhao *et al.*, "Tunable topological phases in nanographene-based spin-1/2 alternating-exchange Heisenberg chains," *Nat. Nanotechnol.*, Oct. 2024. DOI: 10.1038/s41565-024-01805-z.

[145] R. Ortiz, G. Catarina, and J. Fernández-Rossier, "Theory of triangulene two-dimensional crystals," *2D Materials*, vol. 10, no. 1, p. 015 015, Jan. 2023. DOI: 10.1088/2053-1583/aca4e2.

[146] H. Yu and T. Heine, "Prediction of metal-free Stoner and Mott-Hubbard magnetism in triangulene-based two-dimensional polymers," *Sci. Adv.*, vol. 10, no. 40, eadq7954, Oct. 2024.

[147] H. Yu, Y. Jing, and T. Heine, "Physics and Chemistry of Two-Dimensional Triangulene-Based Lattices," *Acc. Chem. Res.*, acs.accounts.4c00557, Dec. 2024. DOI: 10.1021/acs.accounts.4c00557.

[148] G. Sethi *et al.*, "Flat-band-enabled triplet excitonic insulator in a diatomic kagome lattice," *Phys. Rev. Lett.*, vol. 126, p. 196 403, 19 May 2021.

[149] M. Di Giovannantonio and G. Contini, "Reversibility and intermediate steps as key tools for the growth of extended ordered polymers via on-surface synthesis," *J. Phys. Condens. Matter*, vol. 30, no. 9, p. 093 001, Mar. 2018. DOI: 10.1088/1361-648X/aaa8cb.

[150] C. Steiner *et al.*, "Hierarchical on-surface synthesis and electronic structure of carbonyl-functionalized one- and two-dimensional covalent nanoarchitectures," *Nat. Commun.*, vol. 8, no. 1, p. 14 765, Mar. 2017. DOI: 10.1038/ncomms14765.

[151] G. Galeotti *et al.*, "Synthesis of mesoscale ordered two-dimensional π-conjugated polymers with semiconducting properties," *Nat. Mater.*, vol. 19, no. 8, pp. 874–880, Aug. 2020. DOI: 10.1038/s41563-020-0682-z.

[152] N. Friedrich *et al.*, "Addressing Electron Spins Embedded in Metallic Graphene Nanoribbons," *ACS Nano*, vol. 16, no. 9, pp. 14 819–14 826, Sep. 2022. DOI: 10.1021/acsnano.2c05673.

[153] J. Lawrence *et al.*, "Combining high-resolution scanning tunnelling microscopy and first-principles simulations to identify halogen bonding," *Nat. Commun.*, vol. 11, no. 1, p. 2103, Apr. 2020.

[154] M. Bieri *et al.*, "Surface-supported 2D heterotriangulene polymers," *Chem. Commun.*, vol. 47, no. 37, p. 10 239, 2011. DOI: 10.1039/c1cc12490k.

[155] J. Eichhorn *et al.*, "On-surface Ullmann polymerization *via* intermediate organometallic networks on Ag(111)," *Chem. Commun.*, vol. 50, no. 57, pp. 7680–7682, 2014. DOI: 10.1039/C4CC02757D.

[156] L. Dong, P. N. Liu, and N. Lin, "Surface-Activated Coupling Reactions Confined on a Surface," *Acc. Chem. Res.*, vol. 48, no. 10, pp. 2765–2774, Oct. 2015. DOI: 10.1021/acs.accounts.5b00160.

[157] G. Galeotti *et al.*, "Surface-mediated assembly, polymerization and degradation of thiophene-based monomers," *Chem. Sci.*, vol. 10, no. 19, pp. 5167–5175, 2019. DOI: 10.1039/C8SC05267K.

[158] R. Gutzler *et al.*, "Ullmann-type coupling of brominated tetrathienoanthracene on copper and silver," *Nanoscale*, vol. 6, no. 5, pp. 2660–2668, 2014. DOI: 10.1039/C3NR05710K.

[159] C. J. Judd *et al.*, "Ullmann Coupling Reactions on Ag(111) and Ag(110); Substrate Influence on the Formation of Covalently Coupled Products and Intermediate Metal-Organic Structures," *Sci. Rep.*, vol. 7, no. 1, p. 14 541, Nov. 2017. DOI: 10.1038/s41598-017-13315-1.

[160] J. Lawrence *et al.*, "Circumventing the stability problems of graphene nanoribbon zigzag edges," *Nat. Chem.*, vol. 14, no. 12, pp. 1451–1458, Dec. 2022. DOI: 10.1038/s41557-022-01042-8.

[161] M. Bieri *et al.*, "Two-Dimensional Polymer Formation on Surfaces: Insight into the Roles of Precursor Mobility and Reactivity," *J. Am. Chem. Soc.*, vol. 132, no. 46, pp. 16 669–16 676, Nov. 2010. DOI: 10.1021/ja107947z.

[162] S. Schlögl, W. M. Heckl, and M. Lackinger, "On-surface radical addition of triply iodinated monomers on Au(111)—the influence of monomer size and thermal post-processing," *Surf. Sci.*, vol. 606, no. 13-14, pp. 999–1004, Jul. 2012. DOI: 10.1016/j.susc.2012.02.011.

[163] C. Moreno *et al.*, "Bottom-up synthesis of multifunctional nanoporous graphene," *Science*, vol. 360, no. 6385, pp. 199–203, Apr. 2018.

[164] L. Lafferentz *et al.*, "Controlling on-surface polymerization by hierarchical and substrate-directed growth," *Nat. Chem.*, vol. 4, no. 3, pp. 215–220, Mar. 2012.

List of publications

Included in this Thesis

- **A. Vegliante**, M. Vilas-Varela, R. Ortiz, F. Romero-Lara, M. Kumar, L. Gómez-Rodrigo, F. Schulz, D. Soler, H. Ahmoum, E. Artacho, T. Frederiksen, P. Jelínek, J. I. Pascual, and D. Peña, "On-surface Synthesis of a Ferromagnetic Molecular Spin Trimer," Submitted to *J. Am. Chem. Soc.*, 2024.

- **A. Vegliante**, S. Fernández, R. Ortiz, M. Vilas-Varela, T. Y. Baum, N. Friedrich, F. Romero-Lara, A. Aguirre, K. Vaxevani, D. Wang, C. Garcia Fernandez, H. S. J. Van Der Zant, T. Frederiksen, D. Peña, and J. I. Pascual, "Tuning the Spin Interaction in Nonplanar Organic Diradicals through Mechanical Manipulation," *ACS Nano*, vol. 18, no. 39, pp. 26 514–26 521, 2024. DOI: 10.1021/acsnano.4c01963

- J. Hieulle, S. Castro, N. Friedrich, **A. Vegliante**, F. R. Lara, S. Sanz, D. Rey, M. Corso, T. Frederiksen, J. I. Pascual, and D. Peña, "On-surface synthesis and collective spin excitations of a triangulene-based nanostar," *Angew. Chem. Int. Ed.*, vol. 60, no. 48, pp. 25 224–25 229, 2021. DOI: https://doi.org/10.1002/anie.202108301

Other publications

- J. Hieulle, C. Garcia Fernandez, N. Friedrich, **A. Vegliante**, S. Sanz, D. Sánchez-Portal, M. M. Haley, J. Casado, T. Frederiksen, and J. I. Pascual, "From Solution to Surface: Persistence of the Diradical Character of a Diindenoanthracene Derivative on a Metallic Substrate," *J. Phys. Chem. Lett.*, vol. 14, no. 50, pp. 11 506–11 512, 2023. DOI: 10.1021/acs.jpclett.3c02401

- M. Vilas-Varela, F. Romero-Lara, **A. Vegliante**, J. P. Calupitan, A. Martínez, L. Meyer, U. Uriarte-Amiano, N. Friedrich, D. Wang, F. Schulz, N. E. Koval, M. E. Sandoval-Salinas, D. Casanova, M. Corso, E. Artacho, D. Peña, and J. I. Pascual, "On-Surface Synthesis and Characterization of a High-Spin Aza-[5]-Triangulene," *Angew. Chem. Int. Ed.*, vol. 62, no. 41, e202307884, 2023. DOI: 10.1002/anie.202307884

- N. Friedrich, R. E. Menchón, I. Pozo, J. Hieulle, **A. Vegliante**, J. Li, D. Sánchez-Portal, D. Peña, A. Garcia-Lekue, and J. I. Pascual, "Addressing Electron Spins Embedded in Metallic Graphene Nanoribbons," *ACS Nano*, vol. 16, no. 9, pp. 14 819–14 826, 2022. DOI: 10.1021/acsnano.2c05673